

Two Aspects of the Quantum Chromodynamics' Transition at Finite Temperature



Dissertation

zur Erlangung des Doktorgrades
der Naturwissenschaften (Dr. rer. nat.)
der naturwissenschaftlichen Fakultät für Physik
der Universität Regensburg

Vorgelegt von

Bo Zhang

geboren am 28.09.1983 in YueYang (China)

Promotionsgesuch eingereicht am: 11.05.2011

Die Arbeit wurde angeleitet von: Dr. Falk Bruckmann

Prüfungsausschuss:	Vorsitzender:	Prof. Dr. John Lupton
	Erstgutachter:	Prof. Dr. Tilo Wettig
	Zweitgutachter:	Prof. Dr. Andreas Schäfer
	Weiterer Prüfer:	Prof. Dr. Klaus Richter

Datum des Promotionskolloquiums: 27.07.2011

Contents

1	Introduction	1
1.1	Quantum Chromodynamics and its phase diagram	1
1.2	Order parameters of the QCD phase transition	3
1.3	Lattice QCD	4
1.4	Center symmetry and its breaking	5
1.5	Phase transition in finite temperature QCD	6
2	Topological objects	9
2.1	Basics of Topology	9
2.1.1	Homotopy groups	9
2.1.2	Winding numbers	11
2.2	Solitons: an example in 1 + 1 dimension	12
2.3	Vortex	12
2.4	Dirac monopoles	13
2.5	't Hooft–Polyakov monopoles	15
2.6	Instantons	17
2.7	$SU(2)$ calorons	20
2.7.1	Auxiliary functions in caloron	22
2.7.2	The twist	23
2.8	Relations between topological objects	25
2.8.1	Relation between instantons and monopoles	25
2.8.2	Monopole and vortices	25
2.9	Finding topological objects on the lattice	25
2.9.1	Direct maximal center gauge	25
2.9.2	Indirect maximal center gauge	27
2.9.3	Laplacian center gauge	27
2.10	Topological objects and the QCD phase transition	29
2.10.1	Center vortices and confinement	29
2.10.2	Monopoles and confinement	31
2.10.3	Instantons, calorons and the QCD phase transition	32
2.11	The unknown relation – caloron and vortex	33
3	Vortex content of $SU(2)$ calorons	35
3.1	Discretization of calorons	35
3.1.1	Caloron ensembles	36
3.2	$SU(2)$ Laplacian center gauge	37
3.3	Vortices in individual calorons	38
3.3.1	The lowest eigenvector and the LAG monopoles	40

3.3.2	Dyon charge induced vortex	42
3.3.3	Twist-induced vortex	46
3.3.4	Intersection and topological charge	50
3.3.5	Results from maximal center gauges	51
3.4	Vortices in caloron ensembles	53
3.5	Summary	57
4	Vortices in $SU(3)$ calorons	59
4.1	$SU(N)$ calorons	59
4.2	$SU(3)$ Laplacian center gauge and its ambiguity	61
4.3	Twists and vortices in $SU(3)$ calorons	63
5	Dual condensate and dual quark density	71
5.1	Dual condensate and dressed Polyakov loop	71
5.1.1	Definitions and mechanisms	71
5.1.2	Applications beyond the lattice and in other gauge systems	74
5.2	More fermionic observables	75
5.2.1	General fermionic observables	75
5.2.2	Susceptibilities	76
5.3	Dual quark density	79
5.3.1	The Stefan-Boltzmann limit of dual quark density	79
5.3.2	Convergence problems of dual quark density	81
5.4	Technical details of staggered fermions	82
5.4.1	The staggered fermion action	82
5.4.2	Properties of the staggered fermion Dirac operator	83
5.4.3	Staggered fermion operators	85
5.4.4	General fermionic observables	89
5.5	Numerical results	91
5.5.1	General quark condensate	91
5.5.2	Dual condensate	92
5.5.3	Dual quark density	95
6	Summary	99
	Bibliography	101
7	Appendix	107
7.1	Magnetic charge and winding number	107
7.2	Comparison of numerical integration methods for the Fourier transformation	108
	Acknowledgments	113

Chapter 1

Introduction

1.1 Quantum Chromodynamics and its phase diagram

It is accepted that the strong interaction is described by Quantum Chromodynamics (QCD), the Lagrangian of which is

$$L(x) = -\frac{1}{2g^2} \text{Tr} F^{\mu\nu} F_{\mu\nu} - \bar{\psi}(\not{D} + m)\psi + (\text{possible gauge fixing terms}). \quad (1.1)$$

QCD has many interesting perturbative features, like asymptotic freedom [1], which means that the coupling constant of QCD decreases with the growth of energy scale, so that QCD fields, gluons and quarks are decoupled from each other. Likewise, QCD at high energy scale becomes a free gas of these degrees of freedom.

In this thesis, we will focus on some non-perturbative features of QCD in the phase transition/crossover like confinement, which makes we observe hadrons instead of gluons and quarks in the QCD Lagrangian, and chiral symmetry breaking, which contributes the majority of light hadron masses. Let me introduce them below.

The fermion part of the QCD Lagrangian $\bar{\psi}(\gamma^\mu D_\mu + m)\psi$ has two terms, the chiral transformation

$$\psi \rightarrow e^{i\gamma_5\theta}\psi \quad (1.2)$$

keeps the $\bar{\psi}i\gamma^\mu D_\mu\psi$ term invariant but changes the mass term $\bar{\psi}m\psi$. So the QCD Lagrangian is chirally symmetric in the massless limit (chiral limit).

We know the quark masses do not vanish, the light and strange quark masses are $m_u = 1.7 \sim 3.3\text{MeV}$, $m_d = 4.1 \sim 5.8\text{MeV}$ and $m_s = 101_{-21}^{+29}\text{MeV}$, so the quark mass terms break chiral symmetry explicitly. Given that the masses of the u quark and the d quark are very small and the s quark mass is not large, chiral symmetry is an approximate symmetry of QCD.

But even in the chiral limit $m_q = 0$, where the Lagrangian is chirally symmetric, the quark condensate $\langle\bar{\psi}\psi\rangle$, which is not a chiral symmetry conserving operator has a non-vanishing vacuum expectation at low temperature, this is the spontaneous breaking of chiral symmetry.

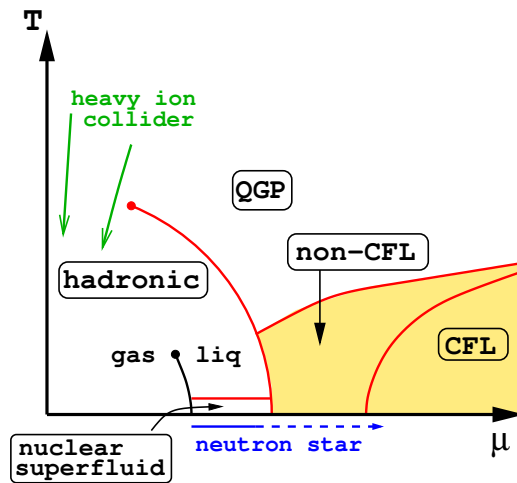


Figure 1.1: Conjectured QCD Phase diagram, from [2].

Confinement means that, at low temperature, one can not find a free quark or other free color charged particles in nature but only color neutral states they form, the hadrons.

Quark confinement is due to that the long range potential of a heavy $\bar{q}q$ pair is (approximately) proportional to the distance between them

$$V_{\bar{q}q}(R) \approx \sigma R. \quad (1.3)$$

If we want to free a quark from this $\bar{q}q$ pair, which means moving one of the quarks to infinity ($R \rightarrow \infty$), we will find we have to face the dilemma that, with the increasing of R , the energy of $\bar{q}q$ rises almost linearly with R , we want to increase R infinitely to free a quark, but after a threshold R_c where $E_{\bar{q}q}(R_c) > 2E_{\bar{q}q}(R_0)$ (R_0 is that of the ground state), the $\bar{q}q$ pair decays into two $\bar{q}q$ pairs. So if the potential of a $\bar{q}q$ pair is proportional to R (although we only need $V(R)|_{R \rightarrow \infty} > 2E_{\bar{q}q}(R_0)$), we can not get a free quark anyway.

Fig. 1.1 shows a commonly conjectured phase diagram of QCD in the μ - T plane, where μ is the chemical potential and T is the temperature. Let us have a brief look at it. Moving rightwards along the μ axis from the origin ($\mu = T = 0$), we travel from QCD vacuum where quarks form hadrons to nuclei, quark matter, and finally enter a (conjectured) color-flavor locking phase of color-superconductivity at very high chemical potential. If we move along the T axis from the origin, as $\mu = 0$ on this axis, there is no favor on quarks or anti-quarks. At low temperature, we have a confined phase of the QCD vacuum, it undergoes a crossover to a deconfined phase at approximately $T = 150 \sim 200\text{MeV}$, where it turns into a plasma of quarks, anti-quarks and gluons there (QGP), which is similar to the early universe. Currently, heavy ion colliders including RHIC and LHC are exploring the phase diagram.

1.2 Order parameters of the QCD phase transition

The QCD phase transition needs observables to manifest it, these observables are order parameters of the QCD phase transition. Polyakov loops and Wilson loops for quark confinement and chiral condensate for chiral symmetry breaking are the most important observables, which will be discussed now.

The Polyakov loops are path ordered exponentials of the gauge field in compact Euclidean time,

$$L(\vec{x}) = P \exp \left(i \int_0^\beta A_0(\vec{x}, t) dt \right), \quad (1.4)$$

where the $\beta = 1/T$ is the time extension of space-time at finite temperature T . The Polyakov loop gives information of the free energy of a static, infinitely heavy quark, its relation to the free energy of such a quark is

$$\langle \text{Tr } L \rangle \propto e^{-\beta F}. \quad (1.5)$$

In the deconfined phase, as the free energy of such a quark is finite, the Polyakov loop is also finite, while in the confined phase the free energy is infinite and the Polyakov loop vanishes,

$$\langle \text{Tr } L \rangle = \begin{cases} 0 & \text{confined phase} \\ \text{finite} & \text{deconfined phase} \end{cases}. \quad (1.6)$$

A detailed proof of the connection between the Polyakov loop and the quark free energy can be found in [3] or [4].

The Wilson loops are rectangular loops extending in space and time direction,

$$W(C) = P \exp \left(\oint_C i A_\mu(x) \cdot dx^\mu \right), \quad (1.7)$$

where C is the loop. It gives information about the binding energy of an infinitely heavy quark pair $\bar{q}q$ in the long time limit ($m_q, T \rightarrow \infty$):

$$\langle \text{Tr } W(R, T) \rangle \propto e^{-V_{\bar{q}q}(R)T}, \quad (1.8)$$

where R and T are the lengths of spatial and temporal sides of the loop respectively. If the potential of the $\bar{q}q$ pair at a large distance R is approximately proportional to the distance,

$$V_{\bar{q}q}(R) \approx \sigma R \quad (1.9)$$

we have $V_{\bar{q}q}(R)T \approx \sigma A$, where $A = RT$ is the area of the rectangle. So an area law in the Wilson loop gives confinement while a perimeter law gives deconfinement

$$\langle \text{Tr } W \rangle \propto \begin{cases} e^{-\sigma A} & \text{confined phase} \\ e^{-cP} & \text{deconfined phase} \end{cases}. \quad (1.10)$$

A detailed proof of the connections between the Wilson loop and the potential $V_{\bar{q}q}(R)$ of a heavy quark pair can be found in [4] or [5].

The chiral condensate is the quark condensate in the chiral limit

$$\chi_{\bar{\psi}\psi} = \lim_{m \rightarrow 0} \lim_{V \rightarrow \infty} \langle \bar{\psi}\psi \rangle. \quad (1.11)$$

We know that in the chiral limit, the QCD Lagrangian is chirally symmetric, but the quark condensate $\langle \bar{\psi}\psi \rangle$ is not, so a non-vanishing chiral condensate means a spontaneous chiral symmetry breaking.

$$\langle \bar{\psi}\psi \rangle = \begin{cases} \text{finite} & \text{chiral symmetry breaking phase} \\ 0 & \text{chiral symmetric phase} \end{cases}. \quad (1.12)$$

1.3 Lattice QCD

Asymptotic freedom says the QCD coupling constant decreases with the growth of temperature, so that the perturbation theory works well at high temperatures. On the other hand, lower temperatures increase the coupling constant, the perturbation theory does not work at low temperature.

There are several methods to deal with low temperature QCD, like QCD sum rules, Dyson-Schwinger equations and lattice QCD simulations, the one we are going to give a brief introduction in this section. In contrast to the other methods, lattice QCD allows calculations from the first principle.

In lattice QCD, fermions reside on the sites only, gluons are replaced by the links between adjacent sites, differential operators by difference operators and the covariant derivative by a difference operator with links.

$$\begin{aligned} \psi(x_\mu) &\Rightarrow \psi(n_\mu) \quad n_\mu \in \{1 \dots N_\mu\} \\ A_\mu &\Rightarrow U_\mu(x) = P \exp(-i \int_{x_\mu}^{x_\mu+a_\mu} A^\mu(y)) \cdot dy_\mu \\ D_\mu \psi(x) &\Rightarrow \frac{1}{2a} (U_\mu(x) \psi(x + \hat{\mu}) - U_\mu^\dagger(x - \hat{\mu}) \psi(x - \hat{\mu})) \end{aligned} \quad (1.13)$$

The QCD action in eqn. (1.1) becomes

$$\begin{aligned} S = & - \sum_{x,\mu,\nu} \frac{1}{g^2 \rho \alpha^4} \text{Tr}(1 - U_{\mu\nu}(x)) \\ & - \sum_{x,\mu} \frac{1}{2a} (\bar{\psi}(x) \gamma_\mu U_\mu(x) \psi(x + \hat{\mu}) - \bar{\psi}(x + \hat{\mu}) \gamma_\mu U_\mu^\dagger(x) \psi(x)) \\ & - \sum_x \bar{\psi}(x) m \psi(x) \end{aligned} \quad (1.14)$$

where the first term replaces the pure gauge field term in the continuous action, the second one replaces the covariant derivative term and the last one is the discretized version of the mass term. There are many lattice actions, eqn. (1.14) is the Wilson action for the links and the naive one for the quarks, we will come back to this in section 5.4.

Monte Carlo simulations need real partition functions, but as we know, the generating function in Minkowski space time is not purely real:

$$Z_M = \int DAD\bar{\psi}D\psi e^{i \int d^4x L(x)}. \quad (1.15)$$

One can continue the time to the imaginary direction $t \rightarrow -i\tau$ where τ is the Euclidean time, so we have $-id^4x_E = d^4x_M$, if we define $L_E = -L_M$, the generating functional becomes

$$Z_E = \int DAD\bar{\psi}D\psi e^{- \int d^4x_E L_E(x)}. \quad (1.16)$$

Comparing it with the partition function of the statistical mechanical systems

$$Z = \text{Tr}[e^{- \int d^3x H/T}], \quad (1.17)$$

it is very clear that the QCD on Minkowski space-time becomes a statistical mechanics system on Euclidean space-time with $H_E = -L_M$ and $T = 1/\beta$ where β is the extension of the lattice in time direction. Lattice QCD simulates this statistical mechanical system.

1.4 Center symmetry and its breaking

The center transformation acts on all the time-like links in one time slice

$$U_0(\vec{x}, t = t_0) \rightarrow zU_0(\vec{x}, t = t_0), \quad (1.18)$$

where z is a center element of the gauge group. $SU(N)$ groups have $N - 1$ center elements,

$$Z_k = e^{\frac{2\pi ik}{N}} \mathbf{1}_N \quad k \in \{0, \dots, N - 1\}. \quad (1.19)$$

Center transformations preserve all the plaquettes, so the (quenched) action is center invariant, and it obvious that the Wilson loops are also center invariant. But the Polyakov loop as a gauge invariant observable is not invariant in center transformations. A Polyakov loop on the lattice is

$$\text{Tr} L(x) = \text{Tr} (U_0(\vec{x}, 1)U_0(\vec{x}, 2)\dots U_0(\vec{x}, N_t - 1)), \quad (1.20)$$

so the center transformation gives an additional z to the Polyakov loops, $P(x) \rightarrow zP(x)$. A similar transformation will be used in the dual observables of Chapter 5.

We see that although center transformation changes the Polyakov loop [6], but it preserves the action and all the Wilson loops, it is a symmetry of the (quenched) action.

In the disordered phase of QCD, the expectation of the Polyakov loop vanishes, so the center symmetry is preserved in the confined phase (these considerations hold in the quenched systems, the fermion determinants will break center symmetry), and the center symmetry is broken in the deconfined phase, as given in eqn. (1.6).

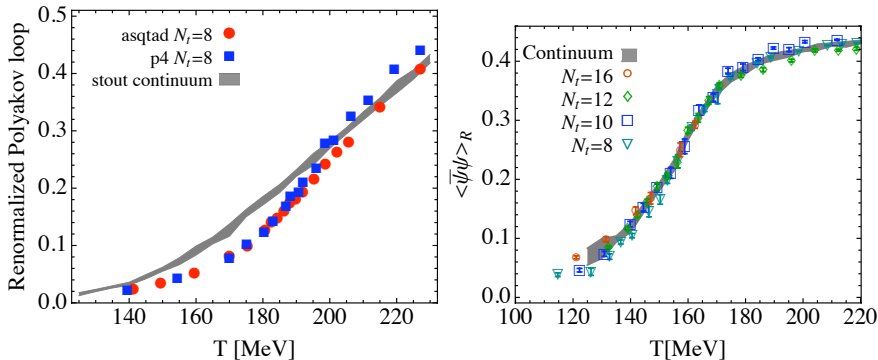


Figure 1.2: The QCD crossover at finite temperature as seen by the renormalized Polyakov loop (left) and light quark condensate (right), from [9].

1.5 Phase transition in finite temperature QCD

As direct calculations are very hard for QCD when the coupling constant is large, Monte Carlo simulations of lattice QCD mentioned in section 1.3 is the method of choice for studies of QCD in the confined phase and near the phase transition.

Recent fully dynamical QCD simulations of the Wuppertal-Budapest collaboration [7, 8, 9] and the hotQCD collaboration [10] on QCD phase transition using staggered fermions show that the transition is a crossover ($\mu = 0$). The latest crossover temperatures¹ of the Wuppertal-Budapest collaboration are (see also Fig. 1.2): 155(3)(3)MeV from renormalized light quark condensate $\langle \bar{\psi}\psi \rangle_R$, 170(4)(3)MeV from renormalized Polyakov loop $\langle L \rangle_R$, 147(2)(3)MeV from chiral quark susceptibility $\chi_{\bar{\psi}\psi}/T^4$, 157(3)(3)MeV from $\Delta_{l,s}$ (see eqn. (3.3) of [8]) and 165(5)(3)MeV from strange quark number susceptibility χ_2^s/T^2 .

We still have many questions on the QCD phase transition, like: What are the basic degrees of freedom in the confined phase and the mechanism by which they give confinement and chiral symmetry breaking? How to relate these degrees of freedom in confined phase with the QCD Lagrangian? How to relate chiral symmetry breaking and confinement from both the observables and the low temperature degrees of freedom in QCD?

Topological objects are candidates for the degrees of freedom in the confined phase. The most important topological objects include instantons, monopoles and vortices. In Chapter 2, we will introduce these topological objects and discuss their relations with confinement and chiral symmetry breaking – instantons have close relations to chiral symmetry breaking, while monopoles and vortices are closer related to confinement.

But what are the relations between different topological objects? The relation between monopoles and center vortices and the relation between instantons and monopoles given in section 2.8 are well established. In this thesis, we will explore the relation between instantons (of finite temperature, called calorons) and center vortices in $SU(2)$ and $SU(3)$ gauge theory in Chapter 3 and Chapter 4, respectively.

¹Simulations with other lattice fermion actions are on the way to cross check these results

The question “How to relate chiral symmetry breaking and confinement?” can be asked in another aspect, the order parameters. The dual condensate introduced in [11, 12] is a novel observable that relates the order parameter of chiral symmetry breaking (chiral condensate) and confinement (Polyakov loop). In this thesis, we will investigate the dual condensate on dynamical staggered fermions and explore a new dual operator: the dual quark density.

This thesis is organized as follows: Chapter 2 introduces the basics of topology (homotopy groups) and different topological objects. Chapter 3 contains the findings about the center vortex contents of $SU(2)$ calorons and caloron ensembles published in [13, 14, 15]. Chapter 4 gives results about center vortices in $SU(3)$ calorons (which are not finally settled because of an ambiguity). Chapter 5 investigates dual condensate and dual quark density theoretically and numerically. In the end, we summarize the results and give a brief outlook.

Chapter 2

Topological objects

Topological objects are classical solutions of Quantum Field Theory (QFT). One might be surprised why classical solutions of QFT are important. We know that QFT is very successful, it interprets quantum excitations of fields as point particles (and the basic degrees of freedom), it gives anomalous magnetic momentum of e and μ , CP violation, asymptotic freedom and many other important phenomena that can not be explained in classical field theory.

Then why do we need classical solutions of QFT? Let us consider QCD, which has a non-Abelian gauge group and the coupling constant is large at low temperature. Strong coupling changes the basic degrees of freedom, making quarks and gluons at low temperatures not point particles. On the other hand, topological objects are of non-perturbative origin and best candidates for non-perturbative effects.

The fundamental concept of topology is to identify mappings from one manifold to another as "homotopic" if they can be deformed one to another continuously. Mappings from k dimensional spheres into a manifold M are the most important cases and form the homotopy groups $\pi_k(M)$, which give information about $k + 1$ dimensional holes in M and are the basis of topological objects.

2.1 Basics of Topology

2.1.1 Homotopy groups

The simplest homotopy group is the first homotopy group π_1 , which is also called the fundamental homotopy group.

Let us begin with the definition of paths. A path is a continuous mapping f from $I = [0, 1]$ to M , where the image of f is a curve in M . A loop is a path whose start point and end point are the same. Then this loop which starts and ends at x_0 is called a loop with base point x_0 .

$$\begin{aligned} f &: [0, 1] \rightarrow M \\ f(0) &= f(1) = x_0. \end{aligned} \tag{2.1}$$

If a loop f can continuously deform into another loop g , which means there exist an interpolating

$$F : [0, 1] \times [0, 1] \rightarrow M \tag{2.2}$$

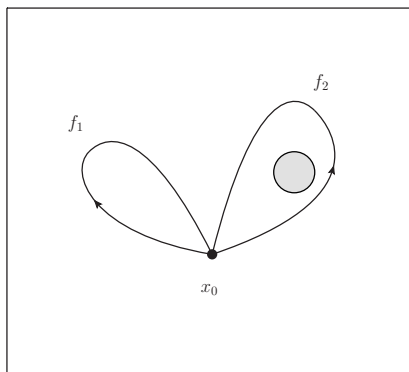


Figure 2.1: Two loops with base point x_0 on I^2 with a hole, where the two loops can be snapped to the point x_0 and surround the hole, respectively, thus belonging to different equivalence classes.

satisfying

$$F(0, \lambda) = f(\lambda), F(1, \lambda) = g(\lambda) \text{ and } F(a, 0) = F(a, 1) = x_0 \quad (2.3)$$

then they are homotopic. Loops are collected into homotopy equivalence classes. We can choose one of the loops, say f , in the homotopy equivalence class to represent it.

We can define the product $h = f \circ g$ by circulating through f and g after each other, this is also a loop with base point x_0 , and it is easy to confirm that the product of loops can be generalized to corresponding homotopy equivalence classes.

With this definition of product, the set of all the homotopy classes on the manifold M with the base point x_0 forms a group. We can confirm that it satisfies all the conditions a group needs. The identity element is the constant loop at x_0 . The inverse loop of f is given by running through f in the opposite direction (so that the product of a loop and its inverse loop is homotopic to the identity). Associativity of three loops holds. These properties can easily be extended to equivalence classes and the first homotopy group of the image manifold M is denoted by $\pi_1(M, x_0)$. It is actually independent of the base point x_0 if M is path connected.

One of the most important first homotopy groups is that of the circle S^1 , it is isomorphic to the group of integers, $\pi_1(S^1) = \mathbf{Z}$, the equivalence classes of $\pi_1(S^1)$ are shown in Fig. 2.2. The plane with one point removed from it, $M = \mathbf{R}^2 \setminus \{0\}$ has the same first homotopy group \mathbf{Z} .

As we mentioned earlier, the k th homotopy group of a manifold M reflects the topological barriers for continuous mappings from S^k to M . Higher homotopy groups are defined in close analogies, by virtue of mappings from I^k to M ,

$$f : I^k \rightarrow M, f(\partial I^k) = x_0. \quad (2.4)$$

The homotopy classes of k dimensional loops on base point x_0 with a suitable definition of the equivalence class product form again a group, $\pi_k(M)$, which again is independent of the base point if the manifold M is path connected.

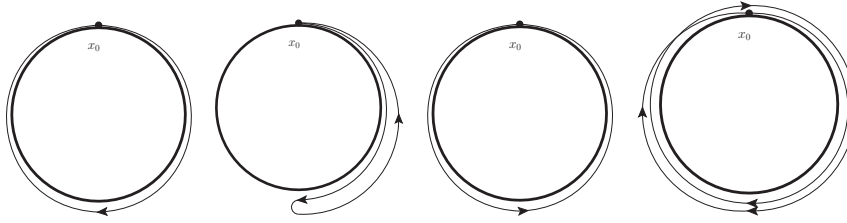


Figure 2.2: Representatives of homotopy classes in $\pi_1(S^1, x_0)$, from left to right, they wind -1 , 0 , 1 and -2 times.

An important difference between the fundamental homotopy group $\pi_1(M)$ and higher homotopy groups $\pi_k(M)$ ($k > 1$) is that fundamental homotopy group can be non-Abelian while higher homotopy groups are always Abelian. The homotopy group related to many topological objects in this chapter are Abelian, like $\pi_2(S^2)$ for 't Hooft–Polyakov monopoles in section 2.5 and $\pi_3(S^3)$ for instantons in section 2.6.

2.1.2 Winding numbers

The winding number is the topological index number for mappings from S^n to S^n as the homotopy groups are isomorphic to the group of integers. We can define it in the language of differential geometry: Let M and N be compact, connected, orientable n dimensional manifolds. We have a differentiable mapping between these two manifolds $f : M \rightarrow N$, and we have a n form ω on N , which is the normalized volume form satisfying

$$\int_N \omega = 1. \quad (2.5)$$

We pull ω back to M , the integral of $f^*\omega$ on M is the Brouwer index of map f .

$$\deg(f) = \int_M f^*\omega \in \mathbf{Z}. \quad (2.6)$$

If two maps f and g are homotopic, their winding numbers are the same

$$\deg(g) = \deg(f), \quad (2.7)$$

We have several examples for winding numbers. The set of unit module complex numbers is isomorphic to S^1 , the winding numbers of the simplest examples are:

$$\begin{aligned} f_1(z) &= z^n & \deg(f_1) &= n \\ f_2(z) &= (z^\dagger)^n & \deg(f_2) &= -n \end{aligned} \quad (2.8)$$

as shown in Fig. 2.2.

The set of $SU(2)$ group elements, $r = x_0\mathbf{1} + ix_i\sigma^i$ (with σ^i the Pauli matrices), is isomorphic to S^3 , so the winding number of two mappings g_1 and g_2 belonging to $\pi_3(S^3)$ are:

$$\begin{aligned} g_1(r) &= r^n & \deg(g_1) &= n \\ g_2(r) &= (r^\dagger)^n & \deg(g_2) &= -n. \end{aligned} \quad (2.9)$$

2.2 Solitons: an example in 1 + 1 dimension

In this section, we will give a simple example of a soliton solution in low dimensions, in which the non-linear interaction disables the superposition principle. This is an interesting feature of topological objects, and an important difference from solutions of linear interaction systems.

The example is a 1 + 1 dimensional system of a scalar field with the Lagrangian

$$L = \frac{1}{2} \partial_\mu \phi \partial^\mu \phi - \frac{1}{b^4} (1 - \cos(b\phi)). \quad (2.10)$$

The Euler-Lagrange equation of this system is the sine-Gordon equation

$$\frac{\partial^2 \phi}{\partial t^2} - \frac{\partial^2 \phi}{\partial x^2} + \frac{1}{b^3} \sin(b\phi) = 0. \quad (2.11)$$

It possesses solitons (or solitary wave) solutions:

$$\phi(x, t) = f(x - vt) = f(\tau) \quad (2.12)$$

where

$$f_{n,\pm}(\tau) = \frac{2\pi n}{b} + \frac{4}{b} \arctan \exp(\pm \frac{\gamma}{b} \tau) \quad n \in \mathbf{Z}, \quad \gamma = \frac{1}{\sqrt{1-v^2}}. \quad (2.13)$$

One can find that the soliton solution $f_{n,\pm}$ connects $\phi(\tau \rightarrow -\infty) = 2\pi n/b$ and $\phi(\tau \rightarrow +\infty) = 2\pi(n \pm 1)/b$, which are minima of the potential $1 - \cos(b\phi)$. It is almost a constant except in the region near $\tau = 0$ where energy density concentrates there. If there are p f_+ like solitons and q f_- like solitons in the system, the difference of ϕ between $\tau = -\infty$ and $\tau = \infty$ is $2\pi(p - q)/b$.

2.3 Vortex

Vortices are 2 dimensional static topological objects carrying quantized electromagnetic flux. A solenoid has magnetic flux through it as shown in Fig. 2.3. A vortex is somehow similar, but with quantized magnetic flux like that trapped in the hole on a superconductor in the Meissner effect.

Consider a $U(1)$ gauge theory of a ‘‘Higgs’’ field ϕ [17]

$$L = -\frac{1}{4} F_{\mu\nu}^2 + |D_\mu \phi|^2 - V(\phi) \quad (2.14)$$

where $V(\phi) = -\sigma^2(\phi^* \phi) + \lambda(\phi^* \phi)^2$. Obviously, a static solution with finite action should reach the minima of $V(\phi)$ at infinity, which is the ‘‘vacuum expectation value’’ of ϕ :

$$|\phi(r)| \xrightarrow{r \rightarrow \infty} \frac{\sigma}{\sqrt{\lambda}} \quad (\text{in polar coordinates}). \quad (2.15)$$

Let us choose a topological nontrivial $\phi(\infty)$, which is a mapping in $\pi_1(S^1)$ with winding number n :

$$\phi(r \rightarrow \infty) = e^{in\theta}, \quad (2.16)$$

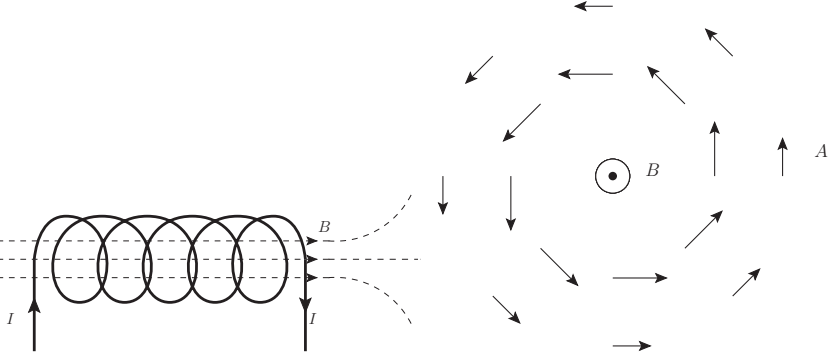


Figure 2.3: The left panel shows a solenoid, the right panel shows a cross section of the solenoid, the magnetic flux in the solenoid and the gauge field are similar to a vortex.

and solve the equations of motion

$$\begin{aligned} D^\mu D_\mu \phi &= \sigma^2 \phi - 2\lambda \phi (\phi^* \phi)^2 \\ ie(\phi \partial_\mu \phi^* - \phi^* \partial_\mu \phi) + 2e^2 A_\mu |\phi|^2 &= \partial^\nu F_{\mu\nu}. \end{aligned} \quad (2.17)$$

The first equation at infinity becomes $D_\mu \phi = 0$, it gives

$$\begin{aligned} A_\theta(r \rightarrow \infty) &= -\frac{n}{er} \\ A_r(r \rightarrow \infty) &= 0, \end{aligned} \quad (2.18)$$

which looks just like the cross section of the solenoid we show in Fig. 2.3.

By Stokes theorem, the magnetic flux through an area S is $\Phi = \int_S B \cdot dS = \oint_{\partial S} A \cdot dl$, so the magnetic flux of the vortex,

$$\Phi = \oint_{\partial S} A \cdot dl = -\frac{2\pi n}{e}, \quad (2.19)$$

is a quantized flux.

2.4 Dirac monopoles

The idea of magnetic monopole was given by Dirac in 1931 [18]. By inserting a magnetic charge term, one can make the Maxwell equations symmetric with respect to their magnetic and electric parts.

The “improved” Maxwell equations are

$$\begin{aligned} \nabla \cdot E &= 4\pi\rho_e, & -\nabla \times E &= \frac{\partial B}{\partial t} + 4\pi j_m \\ \nabla \cdot B &= 4\pi\rho_m, & \nabla \times B &= \frac{\partial E}{\partial t} + 4\pi j_e \end{aligned} \quad (2.20)$$

where the ρ_m and the j_m are the density and the flux of magnetic charge respectively. We can write eqn. (2.20) in the covariant tensor language as

$$\frac{\partial F^{\mu\nu}}{\partial x^\mu} = J_\nu^e, \quad \frac{\partial \tilde{F}^{\mu\nu}}{\partial x^\mu} = J_\nu^m \quad (2.21)$$

where $J = (\rho, j)$ and $\tilde{F}_{\mu\nu} = \frac{1}{2}\epsilon_{\mu\nu\rho\sigma}F^{\rho\sigma}$ is the dual field strength.

If magnetic charge exists, it is a magnetic monopole, and the magnetic field around it should be

$$B = g \frac{\vec{r}}{4\pi|\vec{r}|^3}. \quad (2.22)$$

so that the magnetic flux from a sphere surrounding this magnetic charge is non-zero.

The elementary magnetic charge is determined by the basic electric charge, this is the Dirac quantization condition

$$g = \frac{1}{2e} \quad (2.23)$$

In $U(1)$ gauge theory, the gauge field A_μ can not be written in an expression continuous everywhere on a closed surface S wrapping the magnetic monopole. It is very clear from the fact that the magnetic flux through S is

$$\Phi = \int_S (\nabla \times \vec{A}) \cdot d\vec{S} = 0 \quad (2.24)$$

if \vec{A} is differentiable everywhere. Because the integration of a curl of a differentiable vector function $\vec{f}(x)$ on a surface S with boundary $C = \partial S$ equals the integration of $\vec{f}(x)$ along the boundary C , this is the Stokes Theorem in 2 dimensions:

$$\int_S \nabla \times \vec{f} \cdot d\vec{S} = \oint_C \vec{f} \cdot d\vec{C}. \quad (2.25)$$

As the boundary $C = \partial S$ of a closed surface wrapping the magnetic charge vanishes, we get the (absurd) conclusion that the magnetic flux through S vanishes. We know that the magnetic flux through the surface S equals the magnetic charge inside, so \vec{A} does not have an everywhere differentiable expression on S . If we try to write it this way, we will get a singular point on S . Usually, this singularity can be gauged to a Dirac string with one end on the magnetic charge and the other end at infinity as shown in the right panel of Fig. 2.4.

The mathematically correct way to describe magnetic monopoles are fibre-bundles [19]. Use two charts R_1 and R_2 to cover S , we have differentiable A_μ^1 and A_μ^2 on the two charts respectively, and a transformation V on the overlap of the two charts that connects A_μ^1 and A_μ^2 as shown in the left panel of Fig. 2.4.

We can choose that the first chart R_1 is the north hemisphere including the equator, and R_2 is the south hemisphere, also including the equator. The gauge fields on R_1 and R_2 are [17]

$$\begin{aligned} A_r^1 = A_\theta^1 = 0, \quad A_\phi^1 &= \frac{g}{r} \frac{1 - \cos(\theta)}{\sin(\theta)} \\ A_r^2 = A_\theta^2 = 0, \quad A_\phi^2 &= -\frac{g}{r} \frac{1 + \cos(\theta)}{\sin(\theta)} \end{aligned} \quad (2.26)$$

The gauge transformation connects them on the equator E , being the overlap of R_1 and R_2 :

$$V = e^{2ige\phi}, \quad A_\mu^2 = A_\mu^1 - \frac{i}{e} V \partial_\mu V^\dagger \quad (2.27)$$

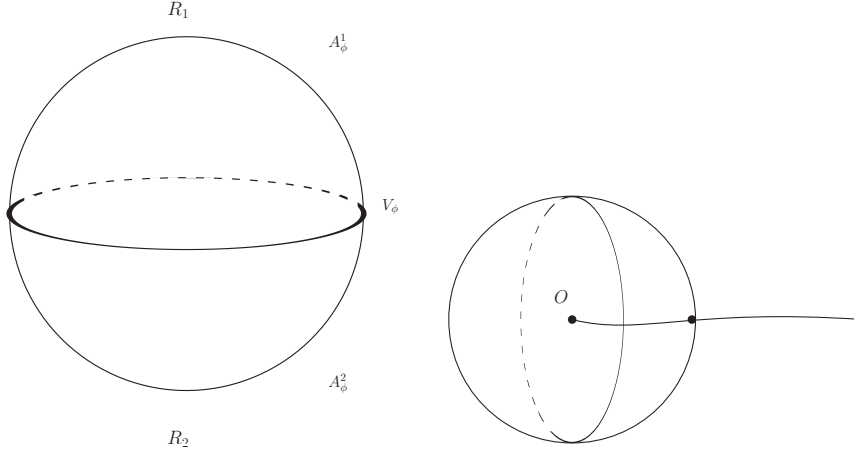


Figure 2.4: The left panel shows the Wu–Yang monopole [19], the right panel is a $U(1)$ magnetic monopole with a Dirac string, where O is the center of the monopole.

Then we find the total magnetic flux through the sphere S^2 is

$$\begin{aligned}\Phi &= \int_{S^2} B \cdot dS = \int_{R_1} B \cdot dS + \int_{R_2} B \cdot dS \\ &= \int_{\partial R_1} A^1 \cdot dl + \int_{\partial R_2} A^2 \cdot dl = \frac{i}{e} \int_E V \partial_\mu V^\dagger dl\end{aligned}\quad (2.28)$$

note that $\partial R_1 = E$ and $\partial R_2 = -E$ are in opposite directions. We can find that $\pi_1(U(1)) \cong \pi_2(S^2) = \mathbf{Z}$ determines the quantization of the magnetic charge.

2.5 't Hooft–Polyakov monopoles

The Dirac monopoles gives a higher symmetry of the magnetism and the electricity, but it has so far not been found experimentally. In 1974, 't Hooft and Polyakov [20, 21] discovered another kind of magnetic monopole which is a classical solution of the equation of motion in non-Abelian gauge theories.

The model is a $SU(2)$ gauge theory with a Higgs field ϕ in the adjoint representation and a Mexican hat potential for it.

$$L = -\frac{1}{4} F_{\mu\nu}^a F_{\mu\nu}^a + \frac{1}{2} (D_\mu \phi)^a (D^\mu \phi)_a - \frac{\lambda}{8} (\phi \cdot \phi - v^2)^2 \quad (2.29)$$

where $F_{\mu\nu}^a$ and $(D_\mu \phi)^a$ are the field strength and the adjoint covariant derivative of ϕ in $SU(2)$:

$$\begin{aligned}F_{\mu\nu}^a &= [D_\mu, D_\nu]^a = \partial_\mu A_\nu^a - \partial_\nu A_\mu^a + e\epsilon^{abc} A_\mu^b A_\nu^c \\ (D_\mu \phi)^a &= \partial_\mu \phi^a + e\epsilon^{abc} A_\mu^b \phi^c \sim [D_\mu, \phi]^a\end{aligned}\quad (2.30)$$

Let us consider the static solutions of this system, with vanishing A_0 , spontaneous symmetry breaking of ϕ and the equation of motion (EOM).

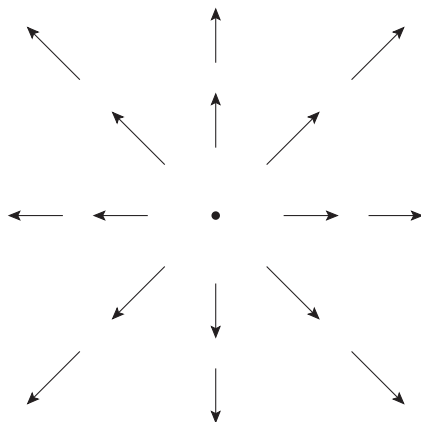


Figure 2.5: The 2d projected Higgs field ϕ of a 't Hooft–Polyakov monopole in the hedgehog gauge.

A finite action solution needs the asymptotic ϕ in a minimum of the potential, which will give the “vacuum expectation value” $|\phi| = v$ at infinity. It spans a S^2 in color space. The gauge symmetry remaining after the symmetry breaking is a $U(1)$ subgroup of $SU(2)$ locally, which can depend on the location \vec{x} . But if the direction of ϕ in color space at infinity $\vec{n}_\phi(\vec{n}_x)$ ($\vec{n}_x = \vec{x}/|x|$, $\vec{n}_\phi = \vec{\phi}/|\phi|$) is a trivial mapping from S^2 to S^2 , the remaining $U(1)$ symmetry can be gauged to a fixed direction, which is completely the same to a $U(1)$ gauge theory. So we choose a nontrivial $\phi(x)$ that $\vec{n}_\phi(\vec{n}_x) = \vec{n}_x$, meaning a hedgehog $\phi^a = vx^a/|x|$ as shown in Fig. 2.5.

The EOM of ϕ is then

$$(D_\mu D^\mu \phi)^a = -\frac{1}{4}(\phi \cdot \phi - v^2)\phi^a, \quad (2.31)$$

the left hand side vanishes at infinity, so the equation can be reduced $D^\mu \phi = 0$, and we can get the solution at infinity

$$\begin{aligned} A_i^a &= -\epsilon_{iab} \frac{x^b}{e|x|^2} \quad (|x| \rightarrow \infty) \\ \phi^a &= v \frac{x^a}{|x|} \quad (|x| \rightarrow \infty) \end{aligned} \quad (2.32)$$

We can also consider the solution of the 't Hooft–Polyakov monopole by minimizing the energy [22, 23]

$$\begin{aligned} E &= \int d^3x ((D_\mu \phi)^2 + B^2 + V(\phi)) = \int d^3x ((D\phi \mp B)^2 + V(\phi) \pm 2B \cdot D\phi) \\ &\geq 2 \left| \int d^3x B \cdot D\phi \right| = 2 \left| \int d^3x \nabla B \cdot \phi \right| = v \left| \int_{S_\infty^2} dS^i (B \cdot n_\phi)_i \right| \end{aligned} \quad (2.33)$$

in whose deduction, $D_i B_i = \epsilon_{ijk} D^i D^j D^k = 0$ and $B_i^a (A^i \phi)_a = \epsilon_{abc} B_i^a A^{ib} \phi^c = (A^i B_i)^a \phi_a$ are used. The last expression is the magnetic flux of the magnetic

field after spontaneous symmetry breaking (projected to the remaining gauge symmetry direction) through S_∞^2 , giving

$$E \geq v|q_{mag}| \quad (2.34)$$

The minimum of the energy E is proportional to v and the magnetic charge of the monopole $4\pi/e$.

The condition for E to reach the minimum is

$$D\phi = \pm B, \quad (2.35)$$

the analytical solution of this equation is given in [22, 23] in the limit of vanishing potential.

$$A_i^a = \epsilon_{aij} \frac{x_j [1 - K(|r|)]}{e|r|^2}, \quad \phi^a = \frac{x_a H(|x|)}{e|x|^2} \quad (2.36)$$

where

$$K(|x|) = \frac{ev|x|}{\sinh(ev|x|)}, \quad H(|x|) = ev|x| \coth(ev|x|) - 1. \quad (2.37)$$

An interesting feature of this static 't Hooft–Polyakov monopole solution is that if we replace the ϕ in $D\phi = \pm B$ by A_0 , it becomes the duality condition of gauge fields in section 2.6

$$F_{\mu\nu} = \pm \tilde{F}_{\mu\nu}. \quad (2.38)$$

This kind of monopoles with A_0 instead of ϕ are called 'dyons' because they have both magnetic and electric charges. They are constituents of calorons which will be introduced in section 2.7.

It can be shown that the magnetic charge is proportional to the winding number of the mapping $\vec{n}_\phi(\vec{n}_x)$ from the S^2 at $|x| \rightarrow \infty$ in coordinate space to the S^2 in color space, see Appendix 7.1. So the topological feature of the 't Hooft–Polyakov monopoles is this S^2 winding number.

2.6 Instantons

Instantons are prominent topological objects in gauge theories, they naturally exist in Euclidean space time as minima of the action.

The boundary of Euclidean space time R^4 is S^3 , so it is possible to find topological objects of S^3 windings in Euclidean space time. The Lagrangian of the gauge field in Euclidean space time is

$$L = \frac{1}{2} \text{Tr}(F_{\mu\nu} F_{\mu\nu}) = \frac{1}{2} (E^2 + B^2). \quad (2.39)$$

We can find that the lower bound of the action is

$$S \geq \left| \int d^4x \frac{1}{2} \text{Tr}(F_{\mu\nu} \tilde{F}_{\mu\nu}) \right| = \frac{8\pi^2}{g^2} |Q| \quad (2.40)$$

where Q is the topological charge

$$Q = \frac{g^2}{16\pi^2} \int d^4x \text{Tr} F_{\mu\nu} \tilde{F}_{\mu\nu}. \quad (2.41)$$

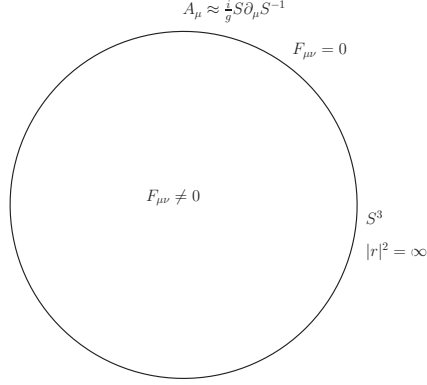


Figure 2.6: The feature of instantons on the S^3 boundary, from [17].

The topological charge is determined by the boundary behavior, this can be seen by writing the topological charge density $\text{Tr} F_{\mu\nu} \tilde{F}^{\mu\nu}$ as the total divergence of the Chern-Simons current:

$$K_\mu = \epsilon_{\mu\nu\sigma\lambda} \text{Tr} \left(\frac{1}{2} A_\nu \partial_\sigma A_\lambda - \frac{ig}{3} A_\nu A_\sigma A_\lambda \right), \quad \partial_\mu K^\mu = \frac{1}{4} \text{Tr} \tilde{F}_{\mu\nu} F^{\mu\nu}. \quad (2.42)$$

Then we rewrite the definition of topological charge in eqn. (2.41) in terms of K_μ

$$Q = \frac{g^2}{16\pi^2} \int d^4x \, 4\partial_\mu K^\mu = \frac{g^2}{4\pi^2} \int_{S_\infty^3} K^\mu \cdot d^3S_\mu \quad (2.43)$$

On the other hand, if we want the action of the solution to be finite, we need

$$r^2 F_{\mu\nu} |_{r \rightarrow \infty} \rightarrow 0 \quad (2.44)$$

so the gauge field approaches a pure gauge field at infinity

$$A_\mu = \frac{i}{g} T \partial_\mu T^\dagger = -\frac{i}{g} (\partial_\mu T) T^\dagger \quad (2.45)$$

as shown in Fig. 2.6.

Then what is the topological charge of a gauge field like this? The K^μ in eqn. (2.42) of the pure gauge field in eqn. (2.45) is

$$K_\mu = \frac{1}{6e^2} \epsilon_{\mu\nu\sigma\lambda} \text{Tr} (T^{-1} \partial_\nu T) (T^{-1} \partial_\sigma T) (T^{-1} \partial_\lambda T). \quad (2.46)$$

Putting it into the topological charge definition of eqn. (2.43), we get

$$\begin{aligned} Q &= \frac{1}{24\pi^2} \int_{S_\infty^3} d^3S_\mu \epsilon_{\mu\nu\sigma\lambda} \text{Tr} (T^{-1} \partial_\nu T) (T^{-1} \partial_\sigma T) (T^{-1} \partial_\lambda T) \\ &= \frac{1}{24\pi^2} \int_{S_\infty^3} d^3S_\infty \det \frac{\partial T(S_\infty^3)}{\partial S_\infty^3} \\ &= \frac{1}{24\pi^2} \int_G dT(S_\infty^3), \end{aligned} \quad (2.47)$$

is proportional to the winding number of the gauge transformation $T(S_\infty^3)$, which is a mapping from the S_∞^3 in coordinate space to the gauge group space given by $\pi_3(G)$.

Let us calculate an $SU(2)$ example of an instanton. We choose $SU(2)$ because its elements can be parameterized easily as

$$g = g^\mu \sigma_\mu \quad (|g| = 1) \quad (2.48)$$

where $\sigma_\mu = (\mathbf{1}_2, i\vec{\sigma})$ and $\vec{\sigma} = (\sigma_1, \sigma_2, \sigma_3)$, so it is clear that $SU(2) \simeq S^3$. The gauge field at infinity approaches a pure gauge field given by eqn. (2.45) where the gauge transformation T is the identical mapping of a hedgehog

$$T = \frac{x_0 \mathbf{1}_2 + i\vec{x} \cdot \vec{\sigma}}{x}. \quad (2.49)$$

Then the asymptotic gauge field on S_∞^3 is

$$A_\mu = \frac{2}{g} \bar{\eta}_{\mu\nu}^a \sigma_a \frac{x_\nu}{x^2} \quad (2.50)$$

where $\bar{\eta}_{\alpha\beta}$ is the self-dual 't Hooft tensor

$$\bar{\eta}_{\alpha\beta} = \bar{\eta}_{\alpha\beta}^\gamma \sigma_\gamma = \bar{\sigma}_{[\alpha} \sigma_{\beta]}, \quad (2.51)$$

and the K_μ is

$$K_\mu = \frac{2x_\mu}{g^2 x^4} \quad (2.52)$$

which has an obvious 'hedgehog' behavior on S_∞^3 . The topological charge of this system is

$$Q = \frac{g^2}{4\pi^2} \int_{S_\infty^3} K \cdot d^3 S = \frac{1}{2\pi^2} \int_{S_\infty^3} \frac{x^\mu}{g^2 x^4} d^3 S_\mu = 1. \quad (2.53)$$

One can extend the gauge field expression in eqn. (2.50) into the bulk of the instanton [24]

$$A_\mu = \frac{2}{g} \bar{\eta}_{\mu\nu}^a \sigma_a \frac{x_\nu}{x^2 + \rho^2}, \quad (2.54)$$

where ρ is the size of the instanton. The topological charge density (action density) of it is

$$\text{Tr} F_{\mu\nu}^2 = \frac{1}{g^2} \frac{\rho^4}{(x^2 + \rho^2)^4}, \quad (2.55)$$

which is obviously a single lump in R^4 , meaning it is an "instantaneous" object. Another parameter of a general charge one instanton solution is the location of instanton center y_μ . For higher charge instantons composed of several lumps, there are $|Q|$ locations and the color orientations are additional parameters of the moduli space.

2.7 $SU(2)$ calorons

In this section we are going to introduce calorons, which are instantons at finite temperature. In other words, their base space is $R^3 \times S^1$ where the circle S^1 has circumference $\beta = 1/k_B T$ as usual. In this section we only discuss the $SU(2)$ calorons which are much simpler than the general $SU(N)$ calorons which will be introduced in section 4.1.

As it turns out from the explicit solutions in [25, 26, 27], calorons consist of localized lumps of topological charge density, which – due to self duality – are lumps of action density, too. For the gauge group $SU(N)$ one can have up to N lumps per unit topological charge. When well separated, these lumps are static, although the gauge field, generically, can and will be time dependent, see section 2.7.2 and section 4.3. Moreover, they possess (quantised) magnetic charge equal to their electric charge and hence are called *dyons* as discussed in section 2.5. Consequently, the moduli of calorons are the spatial locations of the dyons, which can take any value, plus phases [28].

Another important parameter of the solutions by Kraan/van Baal and Lee/Lu [26, 27] is the holonomy, the limit of the (untraced) Polyakov loop in eqn. (1.4) at spatial infinity,

$$\mathcal{P}_\infty = \lim_{|\vec{x}| \rightarrow \infty} L(\vec{x}). \quad (2.56)$$

Due to the magnetic neutrality of the dyons within a caloron, this limit is independent of the direction the limit is taken. (In our convention the gauge fields are hermitian, we basically follow the notation of [26] but multiply their anti-Hermitian gauge fields by i and reinstate β .)

In $SU(2)$ we diagonalise \mathcal{P}_∞ ,

$$\mathcal{P}_\infty = \exp(2\pi i \omega \sigma_3) \quad (2.57)$$

Note that $\omega = 0$ or $1/2$ amount to trivial holonomies $\mathcal{P}_\infty = \pm 1_2$, whereas the case $\omega = 1/4$, i.e. $\text{Tr } \mathcal{P}_\infty = 0$ is referred to as maximal nontrivial holonomy. As we mentioned in section 1.2, $\langle \text{Tr } L \rangle = 0$ confines infinitely heavy quarks. $\omega = 1/4$ calorons therefore should have close relations to the confined phase while $\omega \neq 1/4$ calorons to the deconfined phase.

The constituent dyons have fractional topological charges (“masses”) governed by the holonomy, namely 2ω and $2\bar{\omega} \equiv 1 - 2\omega$, cf. Fig. 2.7 left panel. The topological charges of the dyons are identical in the case of maximal nontrivial holonomy $\omega = 1/4$.

To be more concrete, the gauge field of a unit charge caloron in the periodic gauge ¹ is given by

$$\begin{aligned} A_\mu^3 &= -\frac{1}{2} \bar{\eta}_{\mu\nu}^3 \partial_\nu \log \phi - \frac{2\pi\omega}{\beta} \delta_{\mu,0} \\ A_\mu^1 - iA_\mu^2 &= -\frac{1}{2} \phi (\bar{\eta}_{\mu\nu}^1 - i\bar{\eta}_{\mu\nu}^2) (\partial_\nu + \frac{4\pi i \omega}{\beta} \delta_{\nu,0}) \tilde{\chi}, \end{aligned} \quad (2.58)$$

where $\bar{\eta}$ is the 't Hooft tensor and ϕ and χ are (x_0 -periodic) combinations of trigonometric and hyperbolic functions of x_0 and \vec{x} , respectively, see section 2.7.1

¹This gauge is in contrast to the non-periodic “algebraic gauge” where A_0 asymptotically vanishes and the holonomy is carried by the transition function.

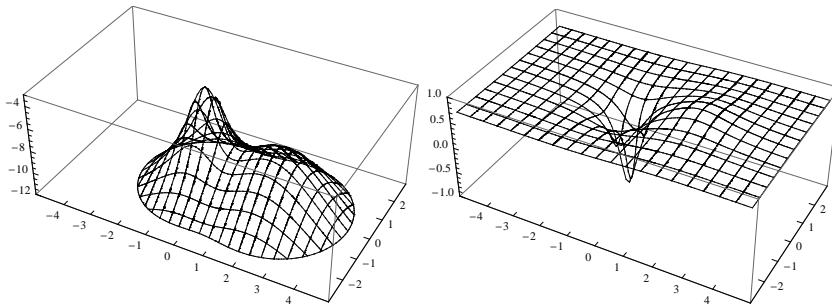


Figure 2.7: Action density (left, shown in logarithmic scale and cut below e^{-12}) and Polyakov loop (right) in the (x_1, x_3) -plane (measured in units of β) at $x_0 = x_2 = 0$ for a caloron with intermediate holonomy $\omega = 0.12$ and size $\rho = 0.9\beta$ as discretized on a $8 \times 48^2 \times 80$ lattice. The dyon locations are $\vec{y}_1 = (0, 0, -0.61)$ and $\vec{y}_2 = (0, 0, 1.93)$.

and [26]. They are given in terms of the distances

$$r = |\vec{x} - \vec{y}_1|, \quad s = |\vec{x} - \vec{y}_2| \quad (2.59)$$

from the following constituent dyon locations

$$\vec{y}_1 = (0, 0, -2\pi\omega\rho^2/\beta), \quad \vec{y}_2 = (0, 0, 2\pi\omega\rho^2/\beta), \quad (2.60)$$

which we have put on the x_3 -axis with the center of mass at the origin (which can always be achieved by space rotations and translations) and at a distance of $d \equiv \pi\rho^2/\beta$ to each other.

In case of large ρ , the action consists of approximately static lumps (of radius $\beta/4\pi\omega$ and $\beta/4\pi\bar{\omega}$ in spatial directions) near \vec{y}_1 and \vec{y}_2 . In the small ρ limit the action profile approaches a single 4d instanton-like lump at the origin. In Ref. [26] one can find more plots of the action density of $SU(2)$ calorons with different sizes and holonomies.

In the far-field limit, away from both dyons the function $\tilde{\chi}$ behaves like

$$\begin{aligned} \tilde{\chi} &= \frac{4d}{(r+s+d)^2} \left\{ r e^{-4\pi\bar{\omega}r/\beta} e^{-2\pi i x_0} + s e^{-4\pi\omega s/\beta} \right\} \\ &\times [1 + \mathcal{O}(e^{-\min(4\pi\bar{\omega}r/\beta, 4\pi\omega s/\beta)})], \end{aligned} \quad (2.61)$$

and hence the off-diagonal part of A_μ decays exponentially, while the Abelian part from

$$\phi = \frac{r+s+d}{r+s-d} + \mathcal{O}(e^{-\min(4\pi\bar{\omega}r/\beta, 4\pi\omega s/\beta)}) \quad (2.62)$$

becomes a dipole field [26].

The Polyakov loop in the bulk plays a role similar to an exponentiated Higgs field in the gauge group: it is $+1_2$ and -1_2 in the vicinity of \vec{y}_1 and \vec{y}_2 ², respectively, cf. Fig. 2.7 right panel. The existence of such points is of topological origin [30, 31, 32]. Thus the Polyakov loop is a more suitable pointer to the

²On the line connecting the dyons the Polyakov loop can actually be computed exactly [29].

constituent dyon locations, which agrees with the maxima of topological density for the limiting case of well-separated dyons, but is valid even in case the two topological lumps merged into one for small ρ .

2.7.1 Auxiliary functions in caloron

Here we give the functions necessary for the gauge fields of calorons [26] including β and their form in the limits described earlier in this section. The first set of auxiliary dimensionless functions is

$$\begin{aligned} \psi &= -\cos(2\pi x_0/\beta) + \cosh(4\pi\bar{\omega}r/\beta) \cosh(4\pi\omega s/\beta) \\ &\quad + \frac{r^2 + s^2 + d^2}{2rs} \sinh(4\pi\bar{\omega}r/\beta) \sinh(4\pi\omega s/\beta) \\ &\quad + d \left(\frac{\sinh(4\pi\bar{\omega}r/\beta)}{r} \cosh(4\pi\omega s/\beta) + \cosh(4\pi\bar{\omega}r/\beta) \frac{\sinh(4\pi\omega s/\beta)}{s} \right) \end{aligned} \quad (2.63)$$

$$\begin{aligned} \hat{\psi} &= -\cos(2\pi x_0/\beta) + \cosh(4\pi\bar{\omega}r/\beta) \cosh(4\pi\omega s/\beta) \\ &\quad + \frac{r^2 + s^2 - d^2}{2rs} \sinh(4\pi\bar{\omega}r/\beta) \sinh(4\pi\omega s/\beta). \end{aligned} \quad (2.64)$$

We remind the reader that $r = |\vec{x} - \vec{y}_1|$ and $s = |\vec{x} - \vec{y}_2|$ are the distances to the dyon locations and $d = |\vec{y}_1 - \vec{y}_2| = \pi\rho^2/\beta$ is the distance between the dyon locations, the ‘‘size of the caloron’’. The next set of auxiliary functions entering eqn. (2.58) are

$$\phi = \frac{\psi}{\hat{\psi}}, \quad \tilde{\chi} = \frac{1}{\psi} d \left(\frac{\sinh(4\pi\bar{\omega}r/\beta)}{r} + e^{-2\pi i x_0/\beta} \frac{\sinh(4\pi\omega s/\beta)}{s} \right) \quad (2.65)$$

For the twist in next subsection we will analyze the limit of large size $d \gg \beta$ here. For points $\vec{x} = \vec{y}_1 + \vec{\delta}$ near the location of the first dyon, $r = |\vec{\delta}|$ is small and $s = d - \delta_3 + O(|\delta|^2/d)$ is large. Hence the argument $4\pi\omega s/\beta$ is much larger than 1 (unless trivial holonomy $\omega = 0$) and the hyperbolic functions can be replaced by exponential functions with exponentially small corrections. On the other hand, no manipulations are made in all functions with argument $4\pi\bar{\omega}r/\beta$, such that we get the exact expressions in terms of the distance r ,

$$\psi = e^{4\pi\omega s/\beta} \frac{d}{r} \sinh(4\pi\bar{\omega}r/\beta) \quad (2.66)$$

$$\hat{\psi} = \frac{1}{2} e^{4\pi\omega s/\beta} \left(\cosh(4\pi\bar{\omega}r/\beta) - \frac{\delta_3}{r} \sinh(4\pi\bar{\omega}r/\beta) \right) \quad (2.67)$$

The exponentially large prefactors cancel in the functions ϕ and $\tilde{\chi}$:

$$\phi(\vec{x} = \vec{y}_1 + \vec{\delta}) \simeq \frac{2d}{|\delta| \coth(4\pi\bar{\omega}|\delta|/\beta) - \delta_3}, \quad (2.68)$$

$$\tilde{\chi}(\vec{x} = \vec{y}_1 + \vec{\delta}) \simeq e^{-2\pi i x_0/\beta} \frac{1}{2d} \frac{|\delta|}{\sinh(4\pi\bar{\omega}|\delta|/\beta)}. \quad (2.69)$$

where we have replaced r by $|\vec{\delta}|$.

For points $\vec{x} = \vec{y}_2 + \vec{\delta}$ near the location of the second dyon, $s = |\vec{\delta}|$ is small and $r = d + \delta_3 + O(\delta^2/d)$ is large leading to

$$\psi = e^{4\pi\bar{\omega}r/\beta} d \frac{\sinh(4\pi\omega s/\beta)}{s} \quad (2.70)$$

$$\hat{\psi} = \frac{1}{2} e^{4\pi\bar{\omega}r/\beta} \left(\cosh(4\pi\omega s/\beta) + \frac{\delta_3}{s} \sinh(4\pi\omega s/\beta) \right) \quad (2.71)$$

and

$$\phi(\vec{x} = \vec{y}_2 + \vec{\delta}) \simeq \frac{2d}{|\delta| \coth(4\pi\omega|\delta|/\beta) + \delta_3}, \quad (2.72)$$

$$\tilde{\chi}(\vec{x} = \vec{y}_2 + \vec{\delta}) \simeq \frac{1}{2d} \frac{|\delta|}{\sinh(4\pi\omega|\delta|/\beta)}. \quad (2.73)$$

2.7.2 The twist

A less-known feature of the caloron we want to describe next is the Taubes twist. It basically means that the gauge field³ of one of the dyons is rotated by a time dependent gauge transformation (rotated in the direction of the holonomy, here the third direction in color space) w.r.t. the gauge field of the other dyon when they are combined into a caloron. This is the way the dyons generate the unit topological charge [26]. And generically, the topological charge can be constructed from relative twisting monopoles.

The simplest way to reveal the twist is to consider the limit of well separated dyons, i.e. when their distance d is much larger than their radii $\beta/4\pi\omega$ and $\beta/4\pi\bar{\omega}$. Let us consider points near the first dyon, $\vec{x} = \vec{y}_1 + \vec{\delta}$, where the distance $\delta \equiv |\vec{\delta}|$ is small compared to the separation d , but not necessarily compared to the dyon size. In the last section we have derived the form of the functions ϕ and $\tilde{\chi}$ in this limit, see eqn. (2.68) and (2.69). The large factors of $2d$ cancel in the $\partial_\mu \log \phi$ and $\phi \partial_\mu \tilde{\chi}$ terms in the caloron gauge field formula eqn. (2.58). The $\tilde{\chi}$ near this dyon has a phase factor $e^{-2\pi i x_0/\beta}$ which does not appear in the $\tilde{\chi}$ near the other dyon, this phase factor will enter non-diagonal entries of A_μ , and this factor reflects the twist of this dyon as we will see later.

In the vicinity of the other dyon, $\vec{x} = \vec{y}_2 + \vec{\delta}$, we get very similar expressions with $\bar{\omega}$ replaced by ω and δ_3 by $-\delta_3$, but the time-dependent phase factor is absent as given in eqn. (2.72) and (2.73). This staticity of course also holds for A_μ near this dyon and all quantities computed from it.

Inserting the auxiliary functions into the gauge field of eqn. (2.58) one can find that the corresponding gauge field components are connected via a PT transformation, and the exchange of ω and $\bar{\omega}$

$$(A_\mu^1 - iA_\mu^2)(x_0, \vec{y}_2 + \vec{\delta}; \omega) = -(A_\mu^1 - iA_\mu^2)(-x_0, \vec{y}_1 - \vec{\delta}; \bar{\omega}) e^{-2\pi i x_0/\beta} \quad (2.74)$$

$$A_\mu^3(x_0, \vec{y}_2 + \vec{\delta}; \omega) = -A_\mu^3(-x_0, \vec{y}_1 - \vec{\delta}; \bar{\omega}) - \frac{\pi}{\beta} \delta_{\mu,0}, \quad (2.75)$$

plus a gauge transformation, namely

$$A_\mu(x_0, \vec{y}_2 + \vec{\delta}; \omega) = -{}^T A_\mu(-x_0, \vec{y}_1 - \vec{\delta}; \bar{\omega}) \quad (2.76)$$

³The twist can be formulated in a gauge-invariant way by field strength correlators between points connected by Schwinger lines [33].

with the time-dependent twist gauge transformation

$$\mathbb{T}(x_0) = \exp\left(-\pi i \frac{x_0}{\beta} \sigma_3\right). \quad (2.77)$$

This gauge transformation is non-periodic, $\mathbb{T}(\beta) = -1_2$ (but acts in the adjoint representation). It enters the non-diagonal entries of the gauge field near the first dyon in eqn. (2.74) and gives the $e^{-2\pi i x_0/\beta}$ factor to it.

The Polyakov loop values inside the dyon centers are obtained from $\tilde{\chi}(\vec{x} = \vec{y}_{1,2} + \delta) = \mathcal{O}(\delta^2)$ and

$$\phi(\vec{x} = \vec{y}_1 + \delta) = \frac{2d}{\beta/4\pi\bar{\omega} - \delta_3 + \mathcal{O}(\delta^2)}, \quad (2.78)$$

$$\phi(\vec{x} = \vec{y}_2 + \delta) = \frac{2d}{\beta/4\pi\omega + \delta_3 + \mathcal{O}(\delta^2)}, \quad (2.79)$$

which results in

$$A_0(\vec{y}_1) = -\frac{\pi}{\beta} \sigma_3 \quad \mathcal{P}(\vec{y}_1) = -1_2, \quad (2.80)$$

$$A_0(\vec{y}_2) = 0 \quad \mathcal{P}(\vec{y}_2) = +1_2. \quad (2.81)$$

Actually, the gauge field around \vec{y}_2 is that of a static magnetic monopole with the Higgs field ϕ identified with A_0 through dimensional reduction. Indeed, it vanishes at the core according to (2.81) and approaches the “vacuum expectation value” $|\phi| = 2\pi\omega/\beta$ away from the core. Accordingly, $D_i\phi$ is identified with $D_iA_0 = F_{i0} = E_i$, and the Bogomolnyi equation with the self duality equation.

The gauge field around \vec{y}_1 is that of a twisted monopole, i.e. a monopole gauge rotated with \mathbb{T} . The corresponding Higgs field is obtained from that of a static monopole by the same \mathbb{T} , transforming in the adjoint representation. Therefore, the Higgs field ϕ of the twisted monopole agrees with the gauge field A_0 apart from the inhomogeneous term in eqn. (2.75). ϕ vanishes at the core, too, and approaches the vacuum expectation value $2\pi\bar{\omega}/\beta$.

The electric and magnetic charges, as measured in the ϕ direction through the 't Hooft field strength tensor, are equal and the same for both dyons. This is consistent with the fact that selfdual configurations fulfilling the BPS bound must have positive magnetic charge.

These fields are in some unusual gauge: around the dyon cores the Higgs field has the hedgehog form $\phi^a \sim (\vec{x} - \vec{y}_{1,2})_a$ which is called the radial gauge. Far away from the dyons the Higgs field ϕ becomes diagonal up to exponentially small corrections. Indeed, if one neglects the exponentially small $\tilde{\chi}$'s of (2.69) and (2.73) and replaces the hyperbolic cotangent by 1 in the denominator of (2.68) and (2.72), this would be the so-called unitary gauge with diagonal Higgs field (in section 2.5) and a Dirac string singularity (along the line connecting the dyons). Far away from the caloron's dyons, however, the “hedgehog” ϕ is not “combed” completely and there is no need for a singularity⁴. In other words the covering of the color space happens in an exponentially small but finite solid angle.

More precisely, the Higgs field ϕ approaches $-2\pi\omega\sigma_3/\beta$ and $+2\pi\bar{\omega}\sigma_3/\beta$ away from the static and twisting dyon, respectively, for almost all directions. These

⁴In contrast, the gauge field A_4 written down in section IIA of [34] is diagonal and A_φ has a singularity at the x_3 -axis.

values differ by $\pi\sigma_3/\beta$, and hence the corresponding A_0 's can be glued together (apart from a gauge singularity at the origin). Moreover, in A_0 the leading far field corrections to the asymptotic value, namely monopole terms, are of opposite sign w.r.t. the fixed color direction σ_3 and therefore do not induce a net winding number in the asymptotic Polyakov loop. Hence the holonomy is independent of the direction.

We remind the reader that this subsection has been dealing with the limit of well-separated dyons, i.e. all formulas are correct up to exponential corrections in β/d and algebraic ones in δ/d .

2.8 Relations between topological objects

2.8.1 Relation between instantons and monopoles

Instantons have been found to induce Abelian projected monopoles, both by topological arguments using the Hopf invariant [35, 36, 37] as well as through empirical studies on the lattice [38, 39, 40].

As we have discussed in section 2.7, the relation between calorons and monopoles/dyons is much clearer, the latter are constituents of the former, visible through e.g. the action density.

2.8.2 Monopole and vortices

In section 2.3, 2.4 and 2.5, we have seen that vortices are magnetic fluxes while monopoles are sources of magnetic fluxes (the vortices in space-time directions correspond to magnetic fluxes, purely spatial vortices do not, examples will be given and discussed in section 3.3). Then it is quite natural to think that the vortices are magnetic fluxes connect monopoles, or in other words, monopoles reside on vortex surfaces.

In the upcoming section 2.9, monopoles identified by Laplace Abelian gauge always reside on vortex sheets identified by Laplacian center gauge [41]. In indirect maximal center gauge, although it does not provide such a close relation, but the $SU(2)$ results of [42] find that almost all (97%) the monopoles lie on vortex sheets.

2.9 Finding topological objects on the lattice

We have learned instantons, monopoles and vortices in previous sections. In this section, we will introduce the methods to find monopoles and vortices on the lattice by Abelian and center projections respectively. Instantons can be found on the lattice after cooling/smearing etc. [43].

2.9.1 Direct maximal center gauge

We know in section 2.3 that vortices are quantised magnetic fluxes. In a gauge group G , the quantized magnetic fluxes Φ_B of

$$e^{ig\Phi_B} = Z_G, \quad (2.82)$$

where Z_G are center elements of G , are called center vortices.

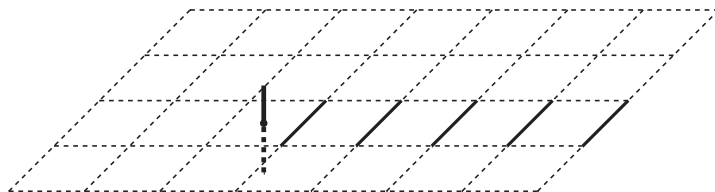


Figure 2.8: An $SU(2)$ example of a center configuration and its vortices. The dashed lines on the plane are trivial $+1$ links, while the solid lines on the plane are -1 links, and the fat line is the vortex penetrating this plane. In short, vortices penetrate the non-trivial plaquettes (in $SU(2)$ just -1 plaquettes).

To find the center vortices on lattice, one needs to project the gauge configurations onto center degrees of freedom by removing the non-confining fluctuations which are supposed to have no influences on the far-infrared physics [6]. Direct maximal center gauge (DMCG) [44] is an intuitive method to reveal the center vortices. It gauge transforms the configuration of adjoint links as close to a trivial configuration (all the links are $\mathbf{1}$) as possible, because center elements of a group G are the identity in the adjoint representation.

We maximize

$$R = \sum_{x,\mu} \text{Tr}[U_{A\mu}(x)], \quad (2.83)$$

where $U_{A\mu}$ are links in the adjoint representation. In $SU(N)$, the expression of R can be simplified to

$$R = \sum_{x,\mu} \text{Tr}[U_\mu(x)]\text{Tr}[U_\mu^\dagger(x)] + \text{const.} \quad (2.84)$$

by virtue of $\sum_k (T_k)_{ab}(T_k)_{cd} = \frac{1}{2}\delta_{ad}\delta_{bc} - \frac{1}{2N}\delta_{ab}\delta_{cd}$ and $(U_A)_{ab} = \text{Tr}[T_a U T_b U^\dagger]$.

After the gauge transformation by maximizing R , the configuration (in fundamental representation) is in the possible closest form to a center configuration. We decompose the links into the center part Z_μ and the remaining fluctuation part V_μ as

$$U_\mu(x) \rightarrow Z_\mu(x)V_\mu(x). \quad (2.85)$$

In $SU(2)$, this decomposition is done by $Z_\mu(x) = \text{sign}(\text{Tr}[U_\mu(x)])$. Note that the vortices are not the non-trivial center element links, but the plaquettes on the dual lattice that penetrate the non-trivial plaquettes as shown in Fig. 2.8.

An advantage of DMCG is that if one ‘inserts’ some center vortices to the configuration by hand, which means to change some links $U \rightarrow Z_k U$, these ‘inserted’ vortices will be detected because the configuration in the adjoint representation is the same to that before the insertion.

DMCG has a weakness, the Gribov copy problem [45]. It happens in the procedure of maximizing R in eqn. (2.84), that R as a function of the gauge transformation has many local maxima. In numerical simulations, it is practically impossible to find the global maximum and one ends up in a local one. This influences the location and further properties of center vortices.

2.9.2 Indirect maximal center gauge

Indirect maximal center gauge (IMCG) [46] is very useful in exploring the connection between Abelian monopoles and vortices [6]. It has two steps, the first step is the maximal Abelian gauge (MAG) [47], which minimizes the non-diagonal elements of the links. In $SU(2)$, it maximizes

$$R = \sum_{x,\mu} \text{Tr}[U_\mu(x)\sigma_3 U_\mu^\dagger(x)\sigma_3], \quad (2.86)$$

this is equivalent to minimizing the non-diagonal elements because

$$\frac{1}{2} \text{Tr}[\sigma^\mu \sigma_3 \bar{\sigma}^\nu \sigma_3] = \begin{cases} 1 & (\mu = \nu = 0, 3) \\ 0 & (\mu \neq \nu) \\ -1 & (\mu = \nu = 1, 2) \end{cases}. \quad (2.87)$$

After having maximized R , one decomposes the links $U'_\mu(x) = C_\mu(x)D_\mu(x)$ into an Abelian part $D_\mu(x)$ and the background part $C_\mu(x)$ where

$$D_\mu = \frac{1}{\sqrt{|U'_{\mu 11}| |U'_{\mu 22}|}} \begin{pmatrix} U'_{\mu 11} & 0 \\ 0 & U'_{\mu 22} \end{pmatrix}. \quad (2.88)$$

Exploiting the remaining $U(1)$ gauge freedom, which amounts to a shift $\theta_\mu(x) \rightarrow {}^\alpha\theta_\mu(x) = -\alpha(x) + \theta_\mu(x) + \alpha(x + \hat{\mu})$, where $\theta_\mu(x) = \arg(U^\mu(x)_{11})$, the second step maximizes the IMCG functional

$$F_{\text{IMCG}}[U] = \sum_{\mu,x} (\cos({}^\alpha\theta_\mu(x)))^2, \quad (2.89)$$

that serves the same purpose as the R in eqn. (2.83).

Finally, the projected $Z(2)$ gauge links are defined as

$$Z_\mu(x) = \text{sign}(\cos({}^\alpha\theta_\mu(x))). \quad (2.90)$$

2.9.3 Laplacian center gauge

Laplacian center gauge (LCG) [41], which avoids the Gribov copies problem, utilizes the two eigenmodes $\phi^{(1)}$ and $\phi^{(2)}$ of the gauge covariant lattice Laplacian operator in the adjoint representation:

$$-\Delta[U_A]\phi^{(1,2)} = \lambda_{1,2}\phi^{(1,2)} \quad (2.91)$$

$$\Delta_{xy}^{ab}[U_A] = \frac{1}{a^2} \sum_{\mu} \left(U_{A\mu}(x)^{ab} \delta_{x+\hat{\mu},y} + U_{A\mu}(x-\hat{\mu})^{ba} \delta_{x-\hat{\mu},y} - 2\delta^{ab} \delta_{xy} \right) \quad a, b = 1, 2, n_A, \quad (2.92)$$

where n_A is the dimension of adjoint representation. Consider that vortices should reflect the infrared feature of the gauge field, the lowest two eigenmodes are preferred.

The first step of LCG, which is also called Laplacian Abelian gauge (LAG) [48], transforms the lowest eigenmode $\Phi^{(1)} = \phi_a^{(1)} T^a$ diagonal,

$$\Phi^{(1)'}(x) = \Omega(x)\Phi^{(1)}(x)\Omega^\dagger(x) \quad \Phi_{i,j}^{(1)'}(x) = 0 \quad (i \neq j). \quad (2.93)$$

The gauge transformation $\Omega(x)$ is not unique, it is easy to find that gauge transformations keeping $\Phi^{(1)'}$ diagonal, namely in the Cartan subgroup of $SU(N)$ matrices, are

$$V(x) = \exp\left(\text{diag}(i\alpha_1(x), \dots, i\alpha_N(x))\right), \quad \sum_{i=1}^N \alpha_i(x) = 0. \quad (2.94)$$

An additional freedom we need to fix in the first step is the exchange of the non-diagonal entries of $\Phi^{(1)'}$ – the eigenvalues of $\Phi^{(1)}$. The gauge transformations exchanging the eigenvalues are not in the $U(1)^{N-1}$ Cartan subgroup, so we should fix the order of the eigenvalues ascending or descending.

We can also identify the remaining symmetry after the first step of LCG by the number of free parameters. An $SU(N)$ matrix has $N^2 - 1$ real parameters, from eqn. (2.93) we can find the number of real conditions is $N(N-1)/2 \times 2 = N(N-1)$. So the remaining number of free parameters is $N-1$ and Cartan subgroup is the remaining symmetry.

As the first step has restricted the remaining symmetry to the Cartan subgroup, the second step fixes the remaining $U(1)^{N-1}$ symmetry to Z_N . Now we see why to choose the adjoint representation, because the adjoint fields are blind to the centers of $SU(N)$

$$Z_k \Phi^{(1,2)} Z_k^\dagger = \Phi^{(i)} \quad (2.95)$$

The first excited eigenmode after the first step is

$$\Phi^{(2)'}(x) = \Omega(x) \Phi^{(2)}(x) \Omega^\dagger(x). \quad (2.96)$$

The second step applies the gauge transformation $V(x) \in U(1)^{N-1}$ to $\Phi^{(2)'}(x)$,

$$\Phi^{(2)''}(x) = V(x) \Phi^{(2)'}(x) V^\dagger(x). \quad (2.97)$$

The remaining $U(1)^{N-1}$ symmetry is fixed by *rotating $N-1$ non-diagonal entries of $\Phi^{(2)''}$ real and positive.*

Defects can occur in the procedure of LCG. In the first step, if $\Phi^{(1)}$ has two equal eigenvalues, or in the second step, if any of the $N-1$ non-diagonal entries of $\Phi^{(2)'}$ vanishes.

The defects of these two LCG steps can be related to monopoles and vortices. The defects of the first step is very obvious in an $SU(2)$ monopole configuration, whose lowest eigenmode is a zero mode, the scalar field ϕ itself (see section 3.3.1) which vanishes at the center of the monopole. So we expect the defects in the first LCG step to be the world lines of monopoles. Indeed, the hedgehog like lowest mode has an S^2 winding number, the first LCG step rotates this lowest mode to a fixed direction meaning the gauge transformation Ω around the monopole reflects an S^2 winding, which will appear in the A_μ from this gauge transformation. In $SU(N)$, the defect promotes the remaining symmetry from $U(1)^{N-1}$ to $SU(2) \times U(1)^{N-3}$.

Let us consider the defects of the second LCG step in $SU(2)$. If one finds $\Phi_{1,2}^{(2)'}(x_V) = 0$ on the plane that passes through x_V and extends in the $e_1 = \nabla \phi_1^{(2)'}(x_V)$ and $e_2 = \nabla \phi_2^{(2)'}(x_V)$ directions (∇ is the gradient operator), the Taylor expansion of $\Phi_{1,2}^{(2)'}$ around x_V is

$$\Phi_{1,2}^{(2)'}(x) = (x - x_V) \cdot e_1 + i(x - x_V) \cdot e_2 + O((x - x_V)^2) \approx f(r, \theta) e^{i\theta}, \quad (2.98)$$

which has a hedgehog form around x_V on this plane. In $SU(2)$, the gauge transformation V around x_V on this plane is

$$V(\theta) = \text{diag}(e^{-\frac{i\theta}{2}}, e^{\frac{i\theta}{2}}). \quad (2.99)$$

While applying the gauge transformation V , the gauge field A_μ around x_V on this plane becomes

$$A_\mu \rightarrow VA_\mu V^\dagger + \frac{i}{g} V \partial_\mu V^\dagger \quad (2.100)$$

where the second term reflects the topological features of V and gives a vortex flux penetrating the $e_1 - e_2$ plane at x_V .

2.10 Topological objects and the QCD phase transition

2.10.1 Center vortices and confinement

The relation of center vortices and confinement was first proposed by 't Hooft in [49], there is a nice review of center vortex confinement in [6].

To find the role of center vortices in confinement, let us consider center vortex configurations superimposed on non-confining configurations, the Wilson loop of a loop C is

$$W(C) = Z(C)w(C), \quad (2.101)$$

where $w(C)$ is the contribution from the non-confining configuration, and $Z(C)$ is the contribution from the center vortices penetrating C .

If different contributions satisfy the two conditions below, the center vortex contributions give the confinement:

1. The non-confining background contribution $w(C)$ and the center vortices contribution $Z(C)$ are weakly correlated if C is a large loop.
2. The correlation between the center vortex contributions to two non-overlapping large loops C_1 and C_2 is weak, or say, the correlation between $Z(C_1)$ and $Z(C_2)$ is weak (not $\langle Z(C_i) \rangle$).

The first condition says the two parts of contributions can be decoupled

$$\langle W(C) \rangle = \langle Z(C) \rangle \langle \text{Tr}[w(C)] \rangle \quad (2.102)$$

where the contributions from non-confining background satisfies a perimeter law.

Then let us consider the second condition. First, we divide the area enclosed by C into N subareas, each subarea enclosed by a sub loop C_i , the subareas are of the same rectangular shape so that their areas equal A/N . The second condition decouples the vortex contributions from different sub loops. Consider translational symmetry, the expectation of vortex contributions to the sub loops should be the same.

$$\langle Z(C) \rangle = \langle \prod_i Z(C_i) \rangle \approx \prod_i \langle Z(C_i) \rangle = \langle Z(C_j) \rangle^N \quad (2.103)$$

Vortices are $D - 2$ dimensional continuous objects, the correlation of penetrations through two large surfaces must be stronger than that through two small

surfaces, so the second condition provides us that the penetration correlations of smaller surfaces are weak.

Then we can continue this procedure and get

$$\langle Z(C) \rangle = (\langle Z_p \rangle)^{\frac{A(C)}{a^2}} = \exp[-\sigma A(c)] \quad (2.104)$$

where $\sigma = -\ln Z_p/a^2$ is the string tension and Z_p is the expectation of center vortex contributions to one plaquette.

In $SU(2)$, the center of the gauge group is $-\mathbf{1}_2$, and the Z_p of a single plaquette is -1 if it is penetrated by vortices and it is 1 if not. So the expectation of Z_p is

$$\langle Z_p \rangle = (1-d)(+1) + d(-1) \quad (2.105)$$

where d is the probability of a plaquette being penetrated by vortices. The string tension in $SU(2)$ is then

$$\sigma = -\frac{\ln(1-2d)}{a^2}. \quad (2.106)$$

We can write the second condition in another way: the vortices penetrations of an area are basically independent. Let us consider the ideal case in which the penetrations are perfectly independent of each other so that the number of penetrations follows a Poisson distribution in the continuum limit

$$P(n) = \frac{\left(\frac{Ad}{a^2}\right)^n}{n!} e^{-\frac{Ad}{a^2}} \quad (2.107)$$

In $SU(2)$ the expectation of vortex contributions is

$$\langle Z(C) \rangle = \sum_{n=0}^{\infty} (-1)^n P(n) = e^{-\frac{2Ad}{a^2}}, \quad (2.108)$$

it gives the string tension

$$\sigma = \frac{2d}{a^2}. \quad (2.109)$$

This result is the continuum limit of eqn. (2.106) as $d \rightarrow 0$ in the continuum limit.

But obviously, the penetrations can not be completely independent because vortices form a closed continuous $D-2$ dimensional surface in the D dimensional space time. The penetrations of an area by a continuous closed surface can not be completely independent. Then what is the feature for the confining vortices? The answer is percolating vortices.

A percolating vortex surface means it is not a local one but crosses the lattice boundary, or in other words, the cluster extension of the vortex surface is the lattice size.

Consider a Wilson loop extending in space and time direction and let us compare a vortex configuration with non-percolating vortex surfaces only with another which includes percolating vortex surfaces as shown in Fig. 2.9.

If the Wilson loop C is large enough, the vortex penetrations of the area spanned by C are correlated except those near the boundary of the area if the vortex surface does not percolate, and Wilson loop is proportional to $e^{-dP(C)}$ in this case, where $P(C)$ is the perimeter of the loop (deconfined phase). The

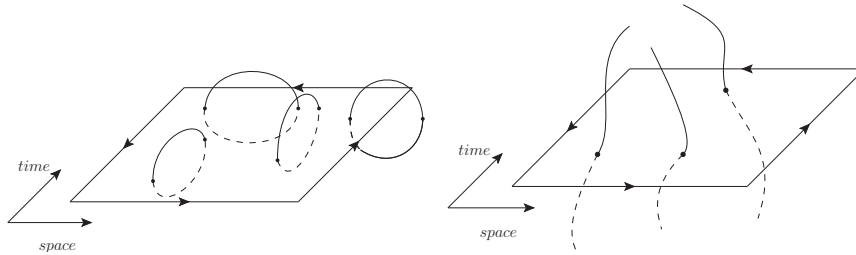


Figure 2.9: The left panel shows non-percolating vortices penetrating the area enclosed by a loop. The penetrations are correlated except those near the edges, thus the vortex only Wilson loop obeys a perimeter law. In contrast, the right panel shows percolating vortices which give the Wilson loop an area law.

percolating vortex surfaces extend to the boundary after penetrating the area and come back to the area only from the other side of the area because of periodic lattice space. So that the penetrations are independent of each other and the Wilson loop gives an area law (confined phase).

Now we see percolation of purely spatial vortex surfaces is the feature of the confined phase. Ref. [50] has compared the vortex cluster extension in the confined phase and the deconfined phase, finding that most vortices belong to a large cluster in the confined phase, while in the deconfined phase most vortices belong to very small clusters.

Several approaches are adopted to verify if vortices are the physical degrees of freedom responsible for confinement, like center dominance and scaling behavior. Center dominance means the vortices alone should recover most of the string tension. The logic of scaling behavior is that, if the vortex contents of configurations reflect physical degrees of freedom, they should have a continuum limit, and quantities like the area of the vortices should approach a constant in the continuum limit.

$SU(2)$ results [46] [44] [51] [52] [53] show that both DMCG and LCG approximately recover the full string tension, but only the DMCG gives the right scaling behavior. In $SU(3)$ [54], DMCG gives the right scaling behavior but does not recover the full string tension, while LCG can recover the full string tension but has a wrong scaling behavior.

2.10.2 Monopoles and confinement

The confinement picture by monopoles is called Dual Superconductor. In superconductors, electrons form weakly bounded states called Cooper pairs, which condensate and squeeze magnetic field into flux tubes. In a dual superconductor, the role of electric parts and magnetic parts are exchanged. Magnetic monopoles condensate and squeeze chromoelectric fluxes. Different from the magnetic fluxes in the superconductor case which form closed loops, chromoelectric fluxes connect chromoelectric charges. Then we find the energy contributions of a flux tube to a $\bar{q}q$ pair is proportional to the length of the flux tube (if the radius of the flux tube is independent of the flux tube length), and the flux tube gives a confining potential. Kronfeld et al. found the color magnetic monopole currents

percolate only in the confined phase [55], it confirms that the dual superconductor picture works also in $SU(2)$.

In section 2.7.2, we have seen the magnetic monopoles in calorons are 't Hooft–Polyakov monopoles with the adjoint scalar field ϕ replaced by A_0 , so the magnetic monopoles exist in theories without the adjoint scalar field ϕ as dyons. So the role of the Higgs field is played by the holonomy at finite temperature.

The monopole condensation picture has some problems, like the representation dependence of the string tension in it seems incorrect [6].

2.10.3 Instantons, calorons and the QCD phase transition

The fermion Lagrangian is

$$L_F = \bar{\psi}(i\gamma^\mu D_\mu + im)\psi \quad (2.110)$$

In the chiral limit $m \rightarrow 0$ where the left hand fermions and right hand fermions decouple with each other, the fermions have definite chirality. With an instanton background, there is a left hand fermion zero mode which satisfies

$$\bar{\sigma}_\mu D_\mu \psi_L = 0 \quad (2.111)$$

and on the anti-instanton background resides a right hand fermion zero mode that satisfies

$$\sigma_\mu D_\mu \psi_R = 0. \quad (2.112)$$

The more general conclusion is the Atiyah-Singer index theorem [56]:

$$Q = n_L - n_R \quad (2.113)$$

where Q is the topological charge, n_L and n_R are the number of left hand and right hand fermion zero modes respectively.

The chiral condensate $\langle \bar{\psi}\psi \rangle_{m \rightarrow 0}$ is the order parameter of chiral symmetry breaking for the QCD phase transition. According to the Banks-Casher relation [57] in eqn.(5.17), the chiral condensate is proportional to the spectral density at origin.

In an instanton liquid [58], if all the instantons and anti-instantons are well separated, each of them contributes a quasi-zero mode (not exact zero mode because of the interaction with other instantons). According to the instanton liquid model, suppose the shifted quasi-zero modes in the multi-instanton background are superpositions of the old exact zero modes of single instanton backgrounds, the shift of such a mode is proportional to

$$T = \int d^4x \psi_j^\dagger(x - y') i\gamma^\mu \partial_\mu \psi_k(x - y) \quad (2.114)$$

where y and y' are the locations of instantons. In the instanton liquid model, the result for the average shift is

$$\langle T^2 \rangle \sim \frac{n}{V} \rho^2 \quad (2.115)$$

and then the spectral density is

$$\frac{\rho(\lambda = 0)}{V} \sim \sqrt{\frac{n}{V}} \frac{1}{\rho} \sim \frac{1}{R^2 \bar{\rho}} \quad (2.116)$$

where $\bar{\rho}$ is the average size of the instantons and \bar{R} is the average distance between the instantons. Hence instantons of realistic sizes and density are able to generate the chiral condensate. However, attempts to generate confinement from instanton models failed (unless unnatural relations between the instantons are assumed).

Calorons [25, 26, 27], as we have introduced in section 2.7, are the finite temperature versions of instantons. Calorons have zero modes like instantons, so that in a liquid of calorons and anti-calorons at finite temperature, they will contribute to the $\rho(0)$ and cause chiral symmetry breaking. The holonomy makes calorons different from instantons. Under the conjecture that the asymptotic Polyakov loop (holonomy) is related to the average Polyakov loop, the order parameter of confinement, calorons are sensitive to the phase of QCD under consideration.

2.11 The unknown relation – caloron and vortex

First, we want to summarize the topological objects that appeared in this chapter. Basically there are three kinds of topological excitations that have been intensively examined over the years to answer the question of what drives confinement and other non-perturbative effects in QCD: instantons, magnetic monopoles and center vortices.

As we introduced in section 2.6, instantons as solutions of the equations of motion are special, in contrast to monopoles or center vortices, which occur only through gauge fixing or projections, they are the relevant objects in a semi-classical approach. While the generation of a chiral condensate is very natural via the (quasi) zero modes, confinement remained unexplained in this model.

At finite temperature, where the classical solutions are called calorons, the asymptotic Polyakov loop as a parameter of calorons makes them sensitive to the phases of QCD. The calorons with nontrivial holonomy consist of N dyons/magnetic monopoles for the gauge group $SU(N)$ (see section 4.1). In this way, contact is seemingly made to the Dual Superconductor scenario. We stress that the dyon constituents of calorons appear in an unambiguous way as classical objects.

The last observation suggests an overall description of confinement [59] and deconfinement in terms of calorons' dyon constituents as independent degrees of freedom. The proposed generalized (approximative) moduli space metric, however, presents some difficulties [60] which are not yet overcome.

Since calorons unify instanton and monopoles, and monopoles generically reside on vortex sheets, it is natural to ask for the relation between calorons and center vortices. What is the vortex content of calorons and what is role of these vortices in the confinement/deconfinement phase? We will start with $SU(2)$ calorons in the next chapter.

Chapter 3

Vortex content of $SU(2)$ calorons

In this and the subsequent chapter we will merge the caloron and vortex picture focusing on two aspects: *(i)* to demonstrate how the vortex content of individual calorons depends on the parameters of the caloron solution – in particular the holonomy – and *(ii)* to obtain the vortices in corresponding caloron ensembles and analyze their percolation properties. In this chapter we will restrict ourselves to the simplest case, a quenched system with gauge group $SU(2)$.

We will mainly use LCG, which has found a correlation of vortices to instantons cores in [61, 62]. We recall that LCG has been abandoned for finding vortices in $SU(2)$ Monte Carlo configurations because the vortex density did not possess a good continuum limit [52]. This observation does not invalidate the application of LCG to smooth (semi-classical) field configurations. We also compare with results obtained by DMCG and IMCG. In order to enable the application of these gauge-fixing techniques we discretize calorons on a lattice, which is known to reproduce continuum results very well.

This chapter is organized as follows. In the next two sections 3.1 and 3.2 we describe technicalities of how to discretize calorons on the lattice and the $SU(2)$ version of LCG. In section 3.3 we discuss the vortex content of single calorons, in particular how the vortex properties change with the holonomy parameter. In section 3.4, we continue with the vortex content of caloron gases and analyze the consequences for the physical mechanism. At the end of this chapter, we conclude with a short summary. The content of this chapter has basically appeared in our publication [14] and the proceedings [13, 15].

3.1 Discretization of calorons

In order to perform the necessary gauge transformations or diagonalizations of the Laplacian operator in numerical form we translate the caloron solutions – and later caloron gas configurations – into lattice configurations.

For a space-time grid (with a temporal extent $N_t = 8$ and spatial sizes of $N_i = 48, \dots, 80$, see specifications later) we compute the links $U_\mu(x)$ as path-ordered exponentials of the gauge field $A_\mu(x)$ (for single-caloron solutions given

by eqn. (2.58)). Practically, the integral

$$U_\mu(x) = \mathcal{P} \exp \left(-i \int_x^{x+a\hat{\mu}} A_\mu(y) dy_\mu \right) \quad (3.1)$$

which has appeared in eqn. (1.13) is decomposed into at least $N = 20$ subintervals, for which this exponential is obtained by exponentiation of $iA_\mu(\tilde{y})a/N$ with $A_\mu(\tilde{y})$ evaluated in the midpoint of the subinterval. These exponential expressions are then multiplied in the required order (from x left to $x + a\hat{\mu}$ right). A necessary condition for the validity of this approximation is that $a/N \ll \rho$ with ρ characterizing the caloron size or a typical caloron size in the multicaloron configurations.

Still this might be not sufficient to ensure that the potential $A_\mu(y)$ is reasonably constant within the subinterval of all links and gives a converged result. In particular, the caloron gauge field (2.58) is singular at the origin and has big gradients near the line connecting the dyons, as visualized in Fig. 2 of [63]. Hence we dynamically adjust the number of subintervals N for every link, ensuring that further increasing N would leave unchanged all entries of the resulting link matrix $U_\mu(x)$.

The discretized caloron constructed this way is not strictly periodic in the space. The resulting mismatch on a periodic lattice, however, is not big for the lattices at hand with $N_i \gg N_t$ because the caloron gauge field far from the dyons decays fast. The action is already very close to the continuum value $8\pi^2$, the maximal deviation occurs for large calorons ($\rho \gtrsim 0.9\beta$) and is about 15 %.

Later on, we will make heavy use of the lowest Laplacian eigenmodes in the LCG. When computing these modes in the caloron backgrounds we enforce spatial periodicity by hand. In Maximal Center gauges we also consider the caloron gauge field as spatially periodic.

3.1.1 Caloron ensembles

The caloron gas configurations considered later in this chapter have been created along the lines of Ref. [64]. The four-dimensional center of mass locations of the calorons are sampled randomly as well as the spatial orientation of the “dipole axis” connecting the two dyons and the angle of a global $U(1)$ rotation around the axis σ_3 in color space. The caloron size is sampled from a suitable size distribution $D(\rho, T)$.

The superposition is performed in the so-called algebraic gauge with the same holonomy parameter ω taken for all calorons and anti-calorons¹. Finally, the additive superposition is gauge-rotated into the periodic gauge. Then the field $A_\mu(x)$ is periodic in Euclidean time and possesses the required asymptotic holonomy. We have applied cooling to the superpositions in order to ensure spatial periodicity of the gauge field.

In section 3.4 we will compare sequences of random caloron gas configurations which differ in nothing else than the global holonomy parameter ω .

¹Superposing (anti)calorons with *different holonomies* would create jumps of A_0 in the transition regions.

3.2 $SU(2)$ Laplacian center gauge

To detect center vortices, we will mainly use the LCG procedure [41], and will compare our LCG results to vortices from the maximal center gauges DMCG and IMCG in section 3.3.5.

As we mentioned in section 2.9.3, LCG needs the two lowest eigenmodes of the gauge covariant Laplacian operator in eqn. (2.92) in the adjoint representation which we calculate by virtue of the ARPACK package [65].

For the $SU(2)$ vortex detection, the lowest mode $\phi^{(1)}$ (in the column vector form) is rotated to the third color direction (diagonalised, in the language of $SU(N)$ LCG),

$$V\phi^{(1)} = |\phi^{(1)}\rangle\sigma_3. \quad (3.2)$$

The remaining Abelian freedom of rotations around the third axis, $V \rightarrow vV$ with $v = \exp(i\alpha\sigma_3)$ is fixed (up to center elements) by demanding for $\phi^{(2)}$ a vanishing second component and positive first component, respectively,

$$({}^vV\phi^{(2)})^{a=2} = 0, \quad ({}^vV\phi^{(2)})^{a=1} > 0. \quad (3.3)$$

Defects of the gauge fixing procedure in $SU(2)$ appear when $\phi^{(1)}$ and $\phi^{(2)}$ are collinear, because then the Abelian freedom parametrized by v remains unfixed. In [41], it was shown that the points x , where $\phi^{(1)}(x)$ and $\phi^{(2)}(x)$ are collinear, define the generically two-dimensional vortex surface, as the Wilson loops in perpendicular planes take center elements. This includes points x , where $\phi^{(1)}$ vanishes, $\phi^{(1)}(x) = 0$, which define monopole worldlines in the Laplacian Abelian Gauge (LAG) [66] in $SU(2)$.

We detect the center vortices in LCG with the help of a topological argument: after having diagonalised $\phi^{(1)}$ by virtue of V , eqn. (3.2), the question whether $\phi^{(1)}$ and $\phi^{(2)}$ are collinear amounts to $V\phi^{(2)}$ being diagonal too, i.e. having zero first and second components. We therefore inspect each plaquette, take all four corners and consider the projections of $V\phi^{(2)}$ taken in these points onto the (σ_1, σ_2) -plane, see Fig. 3.1.

By assuming continuity² of the field $V\phi^{(2)}$ (more precisely, its (σ_1, σ_2) projection) between the lattice sites of this plaquette, we can easily assign a winding number to it. By normalization of the two-dimensional arrows this is actually a discretization of a mapping from a circle in coordinate space to a circle in color space. In the continuum this could give rise to any integer winding number, while with four discretization points the winding number can only take values $\{-1, 0, 1\}$. This winding number can easily be computed by adding the angles between the two-dimensional vectors on neighbor sites.

A nontrivial winding number around the plaquette implies that the (σ_1, σ_2) -components of $V\phi^{(2)}$ have a zero point inside the plaquette, which in turn means that the two eigenvectors are there collinear in color space. In this case we can declare the midpoint of that plaquette belonging to the vortex surface. The vortex surface is a two-dimensional closed surface formed by the plaquettes of the dual lattice. The plaquettes of the dual lattice are orthogonal to and shifted by $a/2$ in all directions relative to the plaquettes of the original lattice.

²The continuity assumption underlies all attempts to measure topological objects on lattices. For semi classical objects it is certainly justified.

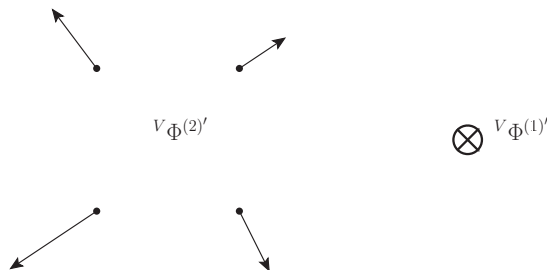


Figure 3.1: The topological argument to detect $SU(2)$ vortices on a given plaquette: The transverse components of the first excited mode $\phi^{(2)}$ to the direction of the lowest mode $\phi^{(1)}$ (after both have been gauge transformed by V) are plotted for the four sites of a plaquette. The configuration shown here has a non vanishing winding number, which implies that the two eigenvectors are collinear in color space somewhere inside the plaquette.

At face value the above procedure is plagued by points where the lowest eigenvector $\phi^{(1)}$ is close to the negative σ_3 -direction. Such situations are inevitable when $\phi^{(1)}$ has a hedgehog behavior around one of its zeroes, i.e. for monopoles in the LAG. Then the diagonalising gauge transformation V changes drastically in space. The corresponding transformed first excited mode $V\phi^{(2)}$ may give artificial winding numbers and thus unphysical vortices if we insist on the continuity assumption in this case.

Actually, to detect vortices, the lowest eigenvector can be fixed to *any* color direction [41], i.e. to different directions on different plaquettes. Using this we rotate $\phi^{(2)}$ plaquette by plaquette to the direction of the average $\bar{\phi}^{(1)}$ over the four corners of the plaquette. This gauge rotation is in most cases a small rotation. Afterwards we inspect $\phi^{(2)}$'s color components perpendicular to the average direction (this can be done by inspecting $V\phi^{(2)}$ in the (σ_1, σ_2) -plane after diagonalising the four-site averaged lowest eigenvector, the resulting gauge transformation now changes only mildly throughout the four sites of the plaquette).

Note that the winding number changes sign under $\phi^{(1)} \rightarrow -\phi^{(1)}$, but not under $\phi^{(2)} \rightarrow -\phi^{(2)}$ (both changes of sign do not change the fact that these fields are the lowest eigenmodes of the Laplacian operator). Hence the global signs of $\phi^{(1)}$, $\phi^{(2)}$ and also the signs of the winding numbers are ambiguous.

3.3 Vortices in individual calorons

The following results are obtained for single calorons discretized on space-time lattices with $N_t = 8$ (meaning that our lattice spacing is $a = \beta/8$) and $N_1 = N_2 = 48$, $N_3 = 80$ or $N_1 = N_2 = N_3 = 64$ points.

For the LCG vortices of calorons we have to take an ambiguity into account, namely the dependence of the adjoint Laplacian spectrum on the lattice discretization, in particular the ratio $N_3/N_{1,2}$. From experience we can summarize that the lowest adjoint eigenmode $\phi^{(1)}$ is rather independent of that ‘‘aspect ratio’’. The first excited mode $\phi^{(2)}$ depends on it in the following way, cf. Fig. 3.2: for large $N_3/N_{1,2}$ the first excited mode $\phi^{(2)}$ is a singlet, whereas

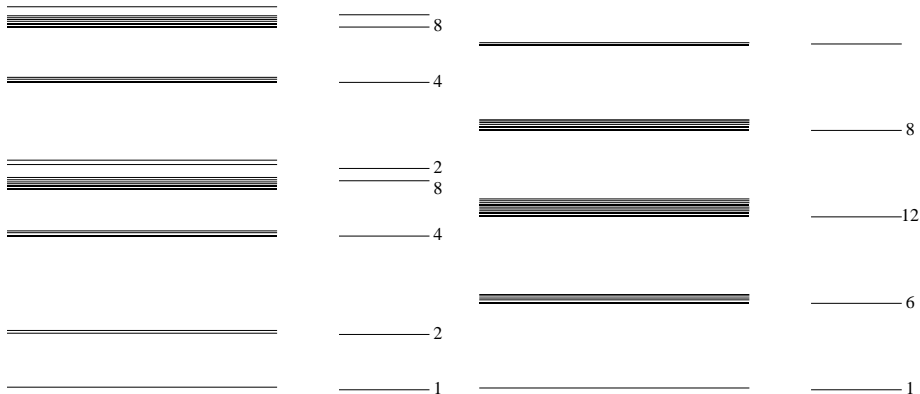


Figure 3.2: The lowest 30 eigenvalues of the adjoint Laplacian operator for a caloron with $\omega = 0.12$ and $\rho = 0.7\beta$ discretized on a $8 \times 48^2 \times 80$ lattice (left) and a $8 \times 64^2 \times 64$ lattice (third from left). Two-fold degeneracies are plotted as bold lines (and some eigenvalues have been slightly shifted to be distinguishable at this resolution). For comparison we plotted in the right panels the free spectra on the same lattices marking their degeneracies by numbers. The lowest singlets on the right panels always belong to the eigenvalue $\lambda = 0$.

for intermediate and small $N_3/N_{1,2}$ it is a doublet.

This ambiguity reflects the fact that we are forcing states of a continuous spectrum into a finite volume, which – like waves in a potential well – are then sensitive to the periodic boundary conditions³. Localized bound states, on the contrary, should not depend much on the discretization.

Indeed, the absolute values and degeneracies of the eigenvalues can be understood by mimicking the caloron with constant links,

$$U_0 = \exp(2\pi i \omega \sigma_3 / N_t), \quad U_i = 1_2, \quad (3.4)$$

that reproduce the holonomy and have zero action. For Laplacian modes in the fundamental representation this approximation was shown to be useful in [67].

In this free-field configuration the eigenmodes are waves proportional to $\prod_{\mu} \exp(2\pi i n_{\mu} x_{\mu} / N_{\mu} a)$ with integer n_{μ} . At nontrivial holonomies and on our lattices with $N_t \ll N_{1,2} \leq N_3$ one can easily convince oneself, that the lowest part of the spectrum is formed by modes in the third color direction, $\phi \sim \sigma_3$, which do not depend on x_0 , $n_0 = 0$. The eigenvalues are then given by trigonometric functions of $2\pi n_i / N_i$, which for large N_i can be well approximated by

$$\lambda \simeq \frac{1}{a^2} \sum_i \left(2\pi \frac{n_i}{N_i} \right)^2 \quad (\text{lowest } \lambda). \quad (3.5)$$

In other words, a wave in the i th direction contributes n_i^2 “quanta” of $(2\pi/N_i)^2$ to the eigenvalue. The lowest eigenvalue in this approximation is always zero. This fits our numerical findings quite well, see Fig. 3.2.

³A similar effect has been observed in Fig. 1 of [36], where the adjoint modes in the background of an instanton over the four-sphere have been shown to depend on the radius of the sphere.

In the asymmetric case, $N_3 = 80$, $N_{1,2} = 48$ obviously the “cheapest excitation” is a wave along the x_3 -axis (connecting the dyons), i.e. $n_3 = \pm 1$. This gives a doublet, which in the presence of the caloron is split into two lines, see Fig. 3.2 left, the first excited mode is thus a singlet (the next modes are those with nontrivial $n_1 = \pm 1$ or $n_2 = \pm 1$ forming an approximate quartet and so on).

In the symmetric case, $N_i = 64$, on the other hand, excitations along all x_i give equal energy contribution. For the excited modes this gives a sextet, which is again split by the caloron, see Fig. 3.2 right. It turns out that the first excited mode remains two-fold degenerate. The eigenmodes are close to combinations of waves with nontrivial $n_1 = \pm 1$ and with nontrivial $n_2 = \pm 1$, reflecting the calorons’ axial symmetry around the x_3 -axis.

This finally explains the different spectra and different shape of the eigenmodes on the different lattices.

3.3.1 The lowest eigenvector and the LAG monopoles

As it turns out, away from the dyons the lowest mode $\phi^{(1)}$ becomes diagonal⁴ and constant, for normalisability reasons it is then approximately $(0, 0, 1/\sqrt{\text{Vol}})^T$ with $\text{Vol} = N_t N_1 N_2 N_3$.

Near each dyon core we find a zero of the third component of the lowest mode, $\phi_{a=3}^{(1)}$, see Fig. 3.3 left panel. Together with the first and second component being very small on the whole x_3 -axis, we expect zeroes in the modulus $|\phi^{(1)}|$ at the constituent dyons, which means that *the dyons are LAG-monopoles*, cf. Fig. 3 in [61] and Fig. 10 in [67].

Such zeroes can be unambiguously detected by a winding number on lattice cubes similar to that of section 3.2. As a result we find almost static LAG-monopole worldlines for large calorons at the locations of their dyons, while

⁴The third direction in color space is distinguished by our (gauge) choice of the holonomy, Eqn. (2.57).

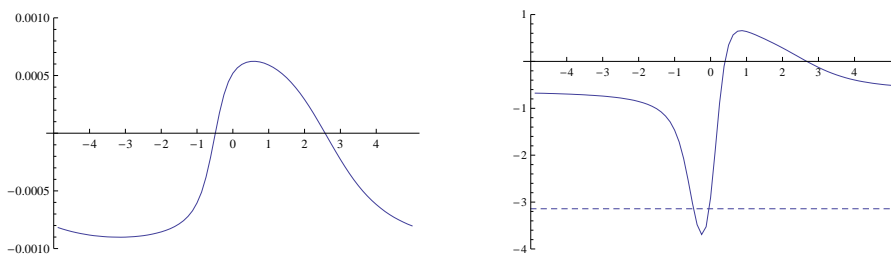


Figure 3.3: Left: The third component of the lowest mode, $\phi^{(1)}_{a=3}$, along the x_3 -axis (in units of β at $x_0 = \beta/2$) for a caloron with intermediate holonomy $\omega = 0.1$ and size $\rho = 1.0$ discretized on a $8 \times 48^2 \times 80$ lattice. The dyons have x_3 -locations -0.63β and 2.51β . Note that for that lattice $1/\sqrt{\text{Vol}} = 0.00082$, a value that is indeed taken on by the lowest mode far away from the dyons. The other components $\phi_{a=1,2}^{(1)}$ are found to be of order 10^{-8} [not shown]. Right: the gauge field $A_0^{a=3}$ (in units of inverse β), which is related to the Higgs field Φ used to explain the behavior of the lowest mode around the dyons (see text). Note that A_0^3 takes the value $-\pi/\beta$ near the twisting dyon.

monopole loops around the caloron center of mass are seen for small calorons (with $\rho \lesssim 0.5$, where the action density is strongly time-dependent as well), see Fig. 3.4. Note that these locations are part of the LCG vortex surface by definition. Similar monopole worldlines have been obtained in the MAG [68, 69]. Adjoint fermionic zero modes, on the other hand, detect the constituent dyons by maxima [70].

The lowest mode also reflects the twist of the caloron: the first and second component of $\phi^{(1)}$ near the dyon core are either static or rotate once with time x_0 evolving from 0 to β . Fig. 3.5 shows this for the lowest mode as well as for the first excited mode. Our results are essentially equal to Fig. 9 of [67], just with a resolution of $N_t = 8$ (instead of $N_t = 4$) more clearly revealing the sine- and cosine-like behaviors.

In order to understand the behavior found for the lowest adjoint mode $\phi^{(1)}$, we propose to compare it to the Higgs field Φ as discussed in section 2.7.2. For the static dyon one has from time-independence $D_0\Phi = 0$ and from the equation of motion $D_i(D_i\Phi) = D_iF_{i0} = 0$. Therefore Φ of a single static dyon is a zero mode of the adjoint Laplacian operator $-\Delta = -D_\mu^2$. For the twisting dyon the same equations apply due to the transformation properties of Φ (under \mathbb{T} , the twist gauge transformation in eqn. (2.77) and the latter is again a zero mode of the Laplacian operator. These zero modes approach a constant (the vev) asymptotically, so they are normalizable like a plane wave.

Around each dyon core, the lowest adjoint mode $\phi^{(1)}$ behaves similar to Φ of that dyon: it vanishes at the dyon core, becomes constant and dominated by the third component away from the dyons, it reveals the Taubes twist (around the twisting dyon) and is in the same gauge as Φ . Since the latter are zero modes of $-\Delta$ in the background of isolated dyons, a combination of them is a natural candidate to be the lowest mode of that (non-negative) operator in the caloron background.

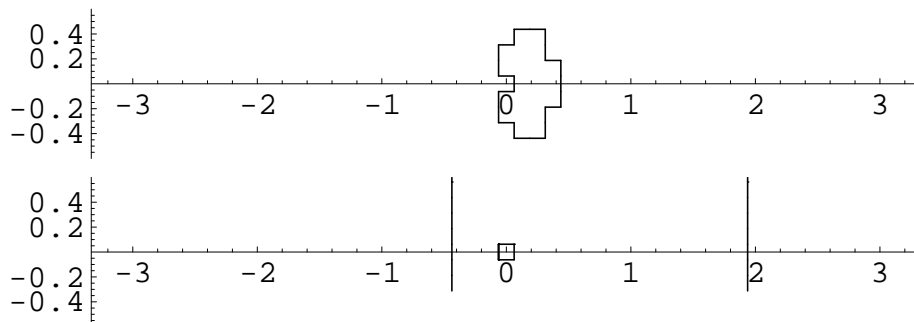


Figure 3.4: Zeroes of the lowest adjoint mode, i.e. monopoles in Laplacian Abelian Gauge, in the (x_0, x_3) -plane (both in units of β , x_3 horizontally, at $x_1 = x_2 = 0$) for calorons of holonomy $\omega = 0.1$ and sizes $\rho = 0.5\beta$ (upper panel, $\vec{y}_1 = (0, 0, -0.16)$, $\vec{y}_2 = (0, 0, 0.63)$) and $\rho = 0.9\beta$ (lower panel, $\vec{y}_1 = (0, 0, -0.51)$, $\vec{y}_2 = (0, 0, 2.04)$). At the origin a closed monopole wordline of minimal size occurs, which we ascribe to the gauge singularity in the caloron gauge field.

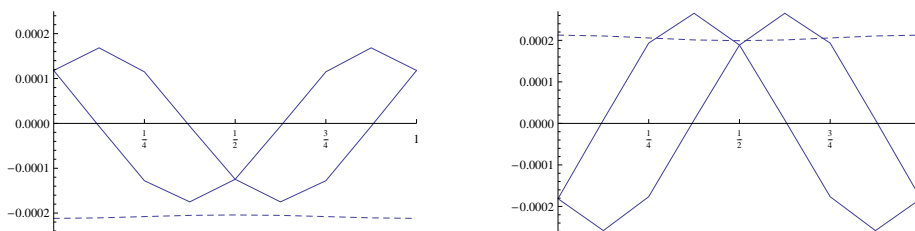


Figure 3.5: The twist of the caloron gauge field reflected in the behavior of the adjoint Laplacian modes. Shown are the individual color components of the lowest mode (left) and the first excited mode (right) as a function of time x_0 in the vicinity of the twisting dyon at \vec{y}_1 . The dashed curve depicts the (almost constant) third color component. The corresponding plots in the vicinity of the static dyon would simply show static lines.

The lowest adjoint mode $\phi^{(1)}$ for calorons with well-separated dyons is therefore best described in the following way, cf. Fig. 3.3: Around the static dyon at \vec{y}_2 one has $\phi^{(1)} \sim \Phi = A_0$, where the proportionality constant of course disappears from the eigenvalue eqn. (2.91), but is approximately given by the normalization: $|\phi^{(1)}| \rightarrow (0, 0, 1/\sqrt{\text{Vol}})^T$. Around the twisting dyon at \vec{y}_1 , one has to compensate for the inhomogeneous term $\phi^{(1)} \sim \Phi = A_0 + \sigma_3(\pi/\beta)$ (cf. eqn. (2.75)). The proportionality constant there turns out to be negative, such that the lowest mode is able to interpolate between these shapes with a rather mild variation throughout the remaining space, see Fig. 3.3 left panel.

3.3.2 Dyon charge induced vortex

In the following we present and discuss one part of the calorons' vortex that is caused by the magnetic charge of constituent dyons. Our findings are summarized schematically in Figs. 3.6 and 3.8.

The ambiguity of the first excited mode $\phi^{(2)}$ of the adjoint Laplacian operator influences this part of the vortex most such that we have to discuss the singlet and doublet cases separately. We find that for the singlet $\phi^{(2)}$, e.g. for $N_3/N_{1,2} = 80/48$, the vortex consists of the whole (x_0, x_3) -plane at $x_1 = x_2 = 0$ only, see Figs. 3.6 and 3.7. Hence this part of the vortex is space-time like. It includes the LAG-monopole worldlines, which are either two open (straight) lines or form

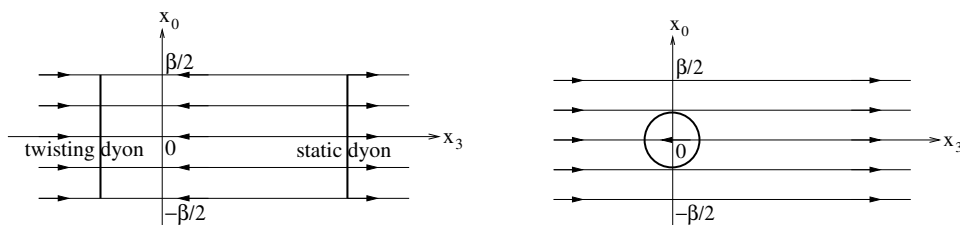


Figure 3.6: The dyon charge induced part of the vortex in case the first excited mode is a singlet: for a large caloron (left) and for a small caloron (right), shown schematically in the plane $x_1 = x_2 = 0$.

one closed loop in that plane. In other words, the space-time vortex connects the dyons once through the center of mass of the caloron and once through the periodic spatial boundary of the lattice.

The magnetic flux (measured through the winding number as described in section 3.2) at every time slice points into the $\pm x_3$ -direction. Its sign changes at the dyons as indicated by arrows⁵ in Fig. 3.6. The flux is always pointing towards the twisting dyon.

Independently of the flux one can investigate the alignment between the lowest and the first excited modes. It changes from parallel⁶ to anti parallel near the static dyon, because the lowest mode $\phi^{(1)}$ vanishes there (i.e. the dyon is a LAG-monopole) [41]. In addition we find two other important facts not mentioned in [41]: the alignment does not change at the twisting dyon since both modes $\phi^{(1)}$ and $\phi^{(2)}$ vanish there and it changes at some other locations outside of the calorons' dyons because $\phi^{(2)}$ has another zero there [not shown].

For the doublet excited mode, i.e. at smaller $N_3/N_{1,2} = 64/64$, the dyon charge induced vortex is slightly different: again it connects the dyons, but now (for a fixed time) via two lines in the “interior” of the caloron, passing near the center of mass, see Figs. 3.8 and 3.9. These lines exist for all times for which the monopole worldline exists, that is *for all times* if the caloron is large and *for some subinterval of x_0* if the caloron is small (and the monopole worldline is a closed loop existing during the subinterval).

These two vortex surfaces spread away from the x_3 -axis which connects the dyons. The axial symmetry around this axis is seemingly broken. However,

⁵We have fixed the ambiguity in the winding number described in section 3.2 by fixing the asymptotic behavior of the lowest mode.

⁶In itself, calling $\phi^{(1)}$ and $\phi^{(2)}$ parallel is ambiguous as that changes when one of these eigenfunctions is multiplied by -1. The *transition* from parallel to anti parallel or vice versa, however, is an unambiguous statement.

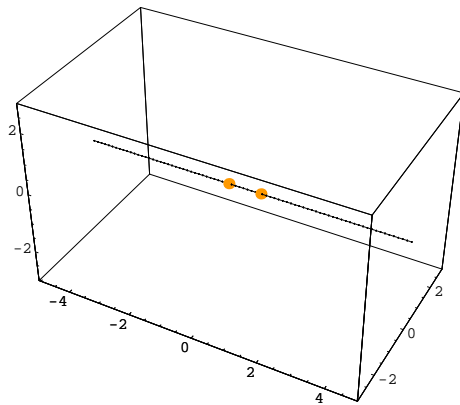


Figure 3.7: The dyon charge induced part of the vortex from the singlet first excited mode as measured in a caloron with holonomy $\omega = 0.25$ and $\rho = 0.6\beta$ in a time slice. The outcome is identical to the x_3 -axis and the same for all time slices. The dots denote points on the vortex (lines along x_0) where the flux changes, i.e. the LAG-monopoles.

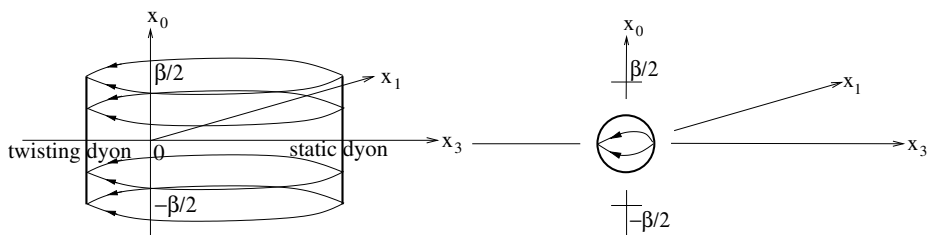


Figure 3.8: The dyon charge induced part of the vortex from the doublet first excited mode for a large caloron (left) and for a small caloron (right) schematically at $x_2 = 0$.

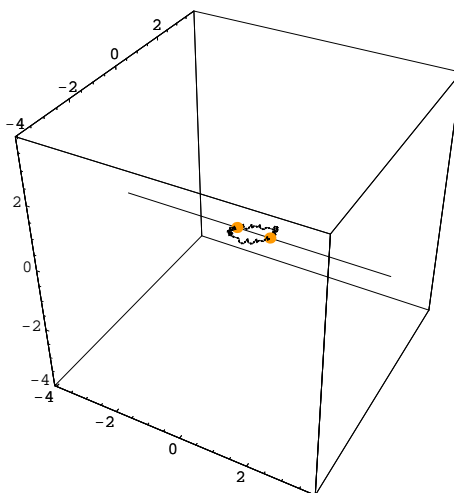


Figure 3.9: The dyon charge induced part of the vortex from the doublet first excited state as measured in a caloron with holonomy $\omega = 0.25$ and $\rho = 0.6\beta$ (same as in Fig. 3.7) at a fixed time slice. Like in Fig. 3.7 the dots denote points on the vortex where the flux flips. The x_3 -axis has been added to guide the eyes, it is not part of the vortex surface here.

using other linear combinations of the doublet in the role of the first excited mode (keeping the lowest one) in the procedure of center projection, the vortex surface is rotated around the x_3 -axis. The situation is very similar to the “breaking” of spherical symmetry in the hydrogen atom by choosing a state of particular quantum number m out of a multiplet with fixed angular momentum l . The magnetic flux flips at the dyons, just like in the case with singlet $\phi^{(2)}$.

Notice that these vortices are predominantly space-time like, but have parts that are purely spatial, in particular for small calorons, namely at minimal and maximal x_0 of the dyon charge induced vortex surface (and at other locations in addition, when the smooth continuum surface is approximated by plaquettes).

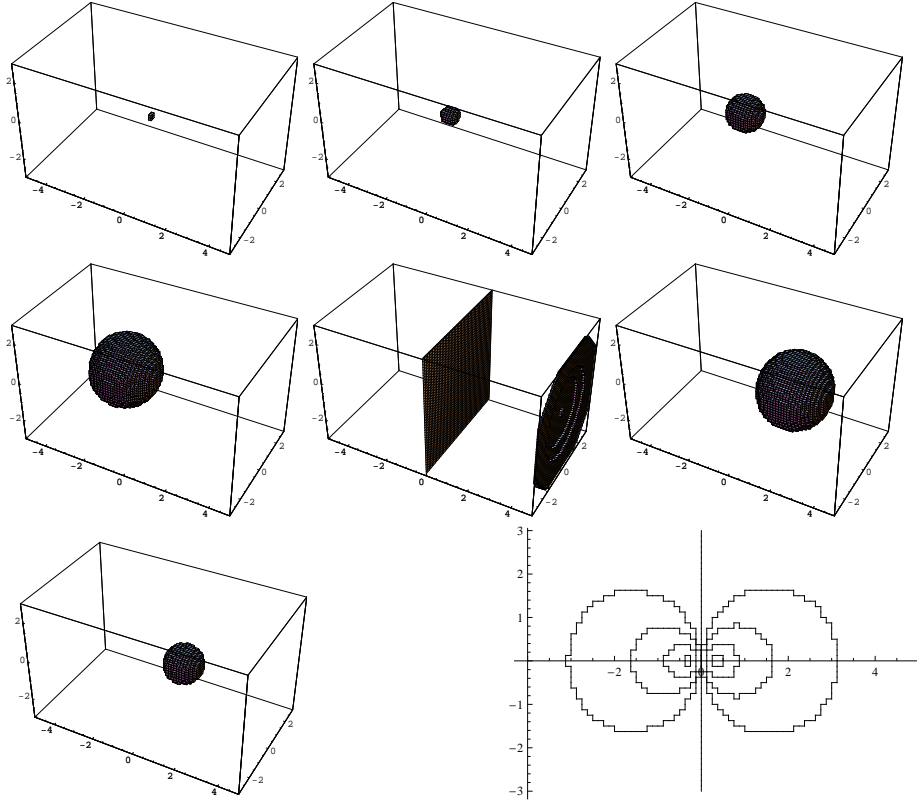


Figure 3.10: Twist-induced part of the vortex (“bubble”) from singlet first excited modes for calorons of size $\rho = 0.6\beta$ and holonomies from left to right: $\omega = 0.1, 0.12, 0.16$ (upper row) $\omega = 0.2, 0.25, 0.3$ (middle row) and $\omega = 0.34$ (lower row, left panel). The plot in the lower right panel summarises the results for $\omega = 0.1, 0.12, 0.16, 0.2, 0.25, 0.3, 0.34$, at $x_1 = 0$, i.e. the bubbles are cut to circles. The plane near the boundary in the $\omega = 0.25$ picture is an artifact caused by periodic boundary conditions.

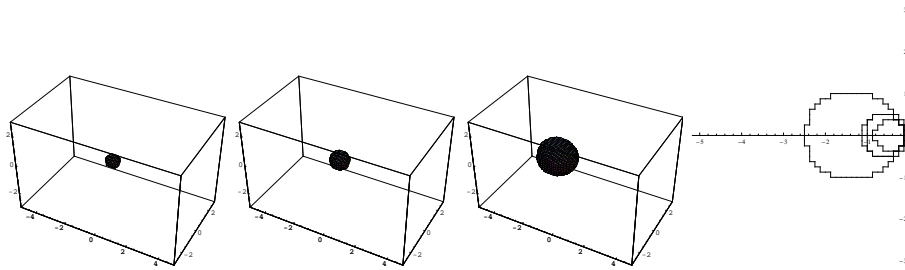


Figure 3.11: Spatial part of the vortex (“bubble”) for calorons of fixed intermediate holonomy $\omega = 0.12$ and sizes from left to right: $\rho = 0.6\beta, 0.7\beta, 0.9\beta$. The panel on the very right shows a summary of the bubbles for $\rho = 0.6\beta, 0.7\beta, 0.8\beta, 0.9\beta$ at $x_1 = 0$. That the bubble for $\rho = 0.9\beta$ is much bigger than that for $\rho = 0.7\beta, 0.8\beta$ is probably a finite volume effect. For small sizes ρ (and also in the limiting cases of holonomy ω close to the trivial values 0 and $1/2$) we have met difficulties in resolving the corresponding small bubbles in the lattice discretization.

3.3.3 Twist-induced vortex

In this section we will discuss the second part of the LCG vortex surfaces we found for individual calorons. We start again by discussing the singlet case. The twist-induced vortex in the singlet case appears at a fixed time slice and hence is a purely spatial vortex. In contrast to the space-time part, this vortex surface does not contain the monopole/dyon worldlines. Hence it is not obvious that this part of the vortex structure is caused by them.

The properties of this spatial vortex depend strongly on the holonomy, which will be very important for the percolation of vortices in caloron ensembles in section 3.4.

In short, our finding is that the twist-induced part of the vortex is a closed surface around the twisting dyon as long as the holonomy parameter is $\omega < 1/4$, and becomes a closed surface around the static dyon for $\omega > 1/4$, we will refer to these surfaces as “bubbles”. For maximal nontrivial holonomy $\omega = 1/4$ the vortex is the $x_3 = 0$ plane, i.e. the mid plane perpendicular to the axis connecting the dyons, we will refer to it as “degenerate bubble”.

The bubble depends on the holonomy ω as shown in Fig. 3.10. For two complementary holonomies $\omega = \omega_0$ and $\omega = \frac{1}{2} - \omega_0$ the bubbles are of same shape just reflected at the origin, thus one of them encloses the static dyon and another encloses the twisting dyon. This is to be expected from the symmetry of the underlying calorons. In the limit of $\omega \rightarrow 1/4$ the bubbles grow to become a flat plane which enables to turn over to the other dyon.

In our $\omega = 0.25$ data we find another piece of the vortex near the boundary of the lattice, see Fig. 3.10. It is an artifact of the finite periodic volume. Likewise, very large bubbles in our results have deformations since they come close to the boundary of the lattice. The intermediate bubbles shown in these figures are generally free from discretization artefacts and can easily be extrapolated (at least qualitatively) to these limits.

The size of the bubble also depends on the size parameter ρ of the caloron, i.e. the distance between the dyons, as shown in Fig. 3.11.

The time-coordinate of LCG bubbles in large calorons is always consistent with $x_0 = 0.5\beta$. For small calorons, on the other hand, $x_0 = 0$ is the exclusive time slice: the action density peaks there and the LAG monopoles are circling around it (cf. Fig. 3.4). However, the bubbles of small calorons are too small to be detected.

In the case of the first excited mode being a doublet, similar bubbles have been found. They also enclose one of the dyons and degenerate to the mid plane for $\omega = 1/4$. Their sizes, however, may be different and they are distributed over several time slices. Considering the collection of all time slices, these fragments add up to full bubbles.

Analytic considerations

In the following we present two analytic arguments – relying on the twist – that support the existence of the bubbles (playing the role of spatial vortices) and help to estimate their sizes.

The first one is specific for vortices in LCG. As we have demonstrated in section 3.3, the lowest mode $\phi^{(1)}$ twists near the twisting dyon and is static near the static dyon. The same holds for the first excited mode $\phi^{(2)}$, see Fig. 3.5.

Then a topological argument shows that they have to be (anti)parallel somewhere in between, cf. Fig. 3.12. As $\phi^{(1)}$, $\phi^{(2)}$ and the diagonalising gauge transformation V are static around the static dyon, so is $V\phi^{(2)}$ and its projection along the third direction (see the right part of Fig. 3.12). We assume that this projection is nonzero, otherwise the two states are obviously (anti)parallel and

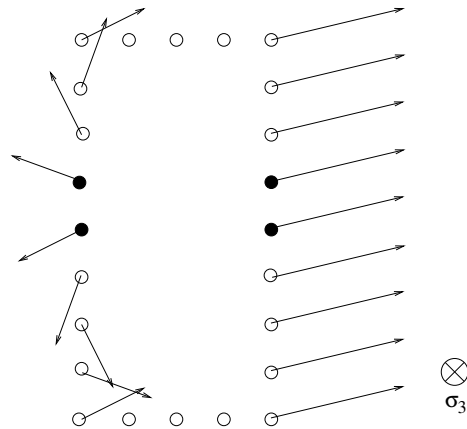


Figure 3.12: Behavior of the non-diagonal elements of V transformed first excited mode $V\phi^{(2)}$ in the twisting region (left) and in the static region (right) with time x_0 evolving upwards. The lattice sites in between are indicated only at $x_0 = 0$. On the entire discretized rectangle the field has winding number 1, meaning it contains the twist-induced vortex. More precisely, it is the “plaquette” marked with filled circles that contains the winding (in analogy to Fig. 3.1) and thus the vortex (in all other plaquettes the field performs a partial winding but then winds back).

the point would belong to the vortex already⁷.

In the twisting region called S , the two lowest modes behave like (suppressing arguments \vec{x})

$$\begin{aligned}\phi^{(1)}(x_0) &= \mathbb{T}(x_0)\phi^{(1)}(x_0=0)\mathbb{T}^\dagger(x_0) \\ \phi^{(2)}(x_0) &= \mathbb{T}(x_0)\phi^{(2)}(x_0=0)\mathbb{T}^\dagger(x_0)\end{aligned}\tag{3.6}$$

with the twisting transformation/rotation from eqn. (2.77). The time dependence of the diagonalising V can be deduced easily⁸,

$$V(x_0) = \mathbb{T}(x_0)V(x_0=0)\mathbb{T}^\dagger(x_0),\tag{3.7}$$

such that

$$V\phi^{(2)}(x_0) = \mathbb{T}(x_0)V\phi^{(2)}(x_0=0)\mathbb{T}^\dagger(x_0).\tag{3.8}$$

Again we assume that the two modes are not (anti)parallel at $x_0 = 0$. Then $V\phi^{(2)}(0)$ has a non-vanishing component perpendicular to σ_3 . According to eqn. (3.8) this component then rotates in time x_0 around the third direction (left part of Fig. 3.12). This immediately implies that there is a space-time ‘‘plaquette’’ (in the sense of Fig. 3.1, marked in Fig. 3.12 with filled circles) that contains a point where the two modes are collinear. Notice the similarity of Figs. 3.12 and 3.1.

This argument applies to all pairs of points with one point in the twisting region S and one point in the static region (its complement) \bar{S} : on any line connecting the two there exists a point which belongs to the vortex. This results in a closed surface at the boundary between S and \bar{S} (see below). The time-coordinate of this surface is not determined by these considerations.

Our argument can be extended to vortices beyond LCG. For that aim we mimic the caloron gauge field by $A_0 = 0$, $A_i = 0$ in the static region \bar{S} and $A_0 = -\sigma_3(\pi/\beta)$, $A_i = 0$ in the twisting region S (cf. eqn. (2.75)) [13].

In this simplified gauge field vortices can be located directly by the definition that -1 Wilson loops are linked with them. Obviously rectangular Wilson loops connecting $(0, \vec{x}_1)$, (β, \vec{x}_1) , (β, \vec{x}_2) , $(0, \vec{x}_2)$ and $(0, \vec{x}_1)$ are -1_2 if and only if \vec{x}_1 belongs to S and \vec{x}_2 belongs to \bar{S} (or vice versa). This again predicts spatial vortices at the boundary between the twisting and the static region.

Actually, this argument is exact if one chooses for the points $\vec{x}_{1,2}$ the dyon locations $\vec{y}_{1,2}$: the path ordered exponentials at fixed $\vec{x}_{1,2}$ are the Polyakov loops $\mp 1_2$ and the remaining spatial parts are inverse to each other because of periodicity and cancel. Hence there should always be a spatial vortex between the two dyons.

Thus *the twist in the gauge field* of the caloron itself *gives rise to a spatial vortex*. This vortex extends in the two spatial directions perpendicular to lines connecting S and \bar{S} , just like a bubble.

Note that the two arguments above do not work purely within the twisting region or purely within the static region.

It remains to be specified where the boundary between the twisting region S and its complement \bar{S} is. To that end one should consider the competing terms

⁷in particular to the space-time part since then the two modes are (anti)parallel for all x_0

⁸The first factor is necessary, otherwise V is singular around the north pole and non-periodic.

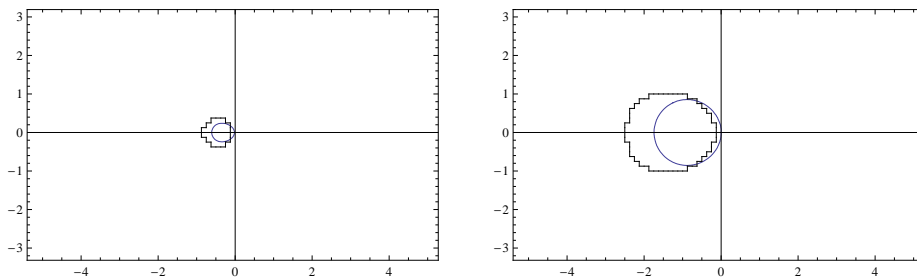


Figure 3.13: The bubbles measured for calorons with holonomy $\omega = 0.12$, size $\rho = 0.6\beta$ (left) and $\rho = 0.9\beta$ (right) respectively as a function of x_2 (vertically) and x_3 (horizontally) at $x_1 = 0$ compared to the boundary of the twisting region S , the smooth curve computed from the equality in eqn. (3.11).

– twisting vs. static – in the relevant function $\tilde{\chi}$, see eqn. (2.65). Actually its derivatives enter the off-diagonal gauge fields, see eqn. (2.58). In the periodic gauge we have used so far, there is an additional term proportional to $\tilde{\chi}$ itself. To decide whether the static or the twisting part dominates (at a given point) it is better to go over to the algebraic gauge, where this term is absent and where $\tilde{\chi}$ must be replaced by $\chi = \exp(4\pi i\omega x_0/\beta)\tilde{\chi}$ [26]. The two competing terms become

$$e^{4\pi i\omega x_0/\beta} \frac{\sinh(4\pi\bar{\omega}r/\beta)}{\psi_r} \equiv f_{\text{static}} \quad (3.9)$$

$$e^{-4\pi i\bar{\omega}x_0/\beta} \frac{\sinh(4\pi\omega s/\beta)}{\psi_s} \equiv f_{\text{twist}} \quad (3.10)$$

with ψ given in eqn. (2.63). Note that the time dependence of these functions still differs by a factor $\exp(2\pi i x_0/\beta)$.

We finally define the twisting region S as where the gradient of f_{twist} dominates

$$|\partial_\mu f_{\text{twist}}|^2 \geq |\partial_\mu f_{\text{static}}|^2. \quad (3.11)$$

and its boundary where the equality holds.

In two particular cases this can be determined analytically. For the case of maximally nontrivial holonomy $\omega = \bar{\omega} = 1/4$, the two functions $f_{\text{static},\text{twist}}$ only differ by the arguments r vs. s . Then the boundary of S is obviously $r = s$, which gives the mid plane between the dyons. This indeed amounts to our numerical finding, the degenerate bubble for $\omega = 1/4$.

In the large caloron limit and if we further assume the solutions of the equality in eqn. (3.11) to obey $\omega r/\beta, \bar{\omega} s/\beta \gg 1$, it is enough to compare in $f_{\text{static},\text{twist}}$ the exponentially large terms in \sinh and ψ . This yields for the boundary of S the equation $\bar{\omega} r = \omega s$, which can be worked out to give

$$x_1^2 + x_2^2 + (x_3 - \Omega d)^2 = (\Omega d)^2, \quad \Omega \equiv \frac{2\omega\bar{\omega}}{\omega - \bar{\omega}} \quad (3.12)$$

Thus the boundary of the twisting region S is a sphere with midpoint $(0, 0, \Omega d)$ and radius $|\Omega|d$. This sphere always touches the origin, is centered at negative and positive x_3 for $\omega < 1/4$ and $\omega > 1/4$, respectively, and again degenerates to the mid plane of the dyons for maximally nontrivial holonomy $\omega = \bar{\omega} = 1/4$.

In Fig. 3.13 we compare the boundary of S obtained from the equality in eqn. (3.11) to the numerically obtained bubbles in LCG for two different values of the caloron parameter ρ . The graphs agree qualitatively.

One could also think of characterising the locations \vec{x} of the twist-induced vortex by a fixed value of the traced Polyakov loop, say $\text{Tr } \mathcal{P}(\vec{x}) = 0$. This also encloses one of the dyons and becomes the mid plane for $\omega = 1/4$. In the large separation limit, however, this surface is that of a single dyon of fixed size set by β and ω (just like the topological density). It does not grow with the separation d , which however seems to be the case for the measured vortices as well as for the boundary of S using the far field limit, eqn. (3.12). Hence the local Polyakov loop seems not a perfect pointer to the spatial vortex.

3.3.4 Intersection and topological charge

To a good approximation the dyon charge induced vortex extends in space and time connecting the dyons twice, whereas the twist induced vortex is purely spatial around one of the dyons. This results in two intersection points generating topological charge as we will describe now.

The notion of topological charge also exists for (singular) vortex sheets. In order to illustrate that let us choose a local coordinate system and denote the two directions perpendicular to the vortex sheet, in which a Wilson loop is -1 , by μ and ν . The Wilson loop can be generated by a circular Abelian gauge field decaying with the inverse distance, which generates a field strength $F_{\mu\nu}$ (the magnetic field, say $B_3 \propto F_{12}$ for a static vortex in the x_3 -direction, is tangential to the vortex, respectively). The corresponding flux is via an Abelian Stokes' Theorem connected to the Wilson loop and is nothing but the winding number used in LCG to detect the vortex.

In order to generate topological charge proportional to $\epsilon^{\mu\nu\rho\sigma} F_{\mu\nu} F_{\rho\sigma}$, the vortex thus needs to “extend in all directions”. This is made more precise by the geometric objects called writhe and self-intersection. The relation to the topological charge including example configurations has been worked out for vortices consisting of hypercubes in [71] and for smooth vortices in [72], [73] and [74]. The result is that a (self)intersection point – where two branches of the vortex meet such that the combined tangential space is four-dimensional – contributes $\pm 1/2$ to the topological charge. The contribution of the writhe is related to gradients of the vortex' tangential and normal space w.r.t. the two coordinates parametrising the vortex. Two trivial examples are important for vortices in a

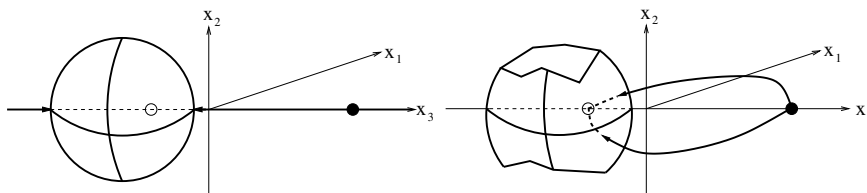


Figure 3.14: The intersection of the spatial bubble (at fixed $x_0 = \beta/2$) for $\omega < 1/4$ with the space-time part of the vortex from the singlet (left) and the doublet (right) excited mode (in the doublet case the bubble is distributed over several time slices).

caloron: a two-dimensional plane as well as a two-dimensional sphere embedded in four-dimensional space have no writhe. Since the two parts of our vortex are of these topologies, we immediately conclude that the topological charge of vortices in calorons comes exclusively from intersection points.

We first discuss the position of the intersection points in the singlet case, cf. Fig. 3.14 left panel. The twist induced bubble occurs at a fixed time slice and so does any intersection point. The dyon induced vortex consists of two static straight lines from one of the dyon to another and therefore intersects the bubble twice on the x_3 -axis.

There are two exceptions to this fact: for small calorons (small ρ) the dyon induced vortex exists in some time slices only and the number of intersection points depends on whether the time-coordinate of the bubble is within that time-interval (but the bubble is usually too small to detect when ρ is small).

The case of maximal nontrivial holonomy is particular because for the corresponding degenerate bubble there is only one intersection point at the center of mass of the caloron, the other one moved to $x_3 \rightarrow \pm\infty$ as $\omega \rightarrow 1/4 \pm 0$ in infinite volume.

Concerning the sign of the contributions, it is essential that the relative sign of the vortex flux is determined: the magnetic flux of the dyon induced vortex flips at the dyons and hence is of opposite sign at the intersection points on the bubble. One can depict the flux on the bubble by an electric field normal to the bubble (i.e. hedgehog-like). It follows that in LCG the contributions of the intersection points to the topological charge of the vortex are both $+1/2$.

The vortex in the caloron is thus an example for a general statement, that a non-orientable vortex surface is needed for a non-vanishing total topological charge. In our case the two branches of the dyon charge induced vortex have been glued together at the dyons in a non-orientable way: the magnetic fluxes start or end at the dyons as LAG-monopoles (this construction is impossible for the bubble as the dyons are not located on them). Thus, vortices without monopoles on them possess trivial total topological charge.

In the doublet case with its fragmented bubbles there are still two intersection points (cf. Fig. 3.14 bottom panel) which again contribute topological charges of $+1/2$ each.

To sum up this section we have demonstrated that the vortex has unit topological charge like the caloron background gauge field. This result is not completely trivial as there is to our knowledge no general proof that the topological charge from the gauge field persists for its vortex ‘‘skeleton’’ after center projection (P-vortices). Moreover, the topological density of the caloron is not maximal at the two points where the topological density of the vortex is concentrated and the total topological charge of the caloron is split into fractions of 2ω and $2\bar{\omega}$ whereas that of the vortex always comes in equal fractions $1/2$ from two intersection points, close to the static dyon if $\omega < 1/4$ and close to the twisting dyon if $\omega > 1/4$.

3.3.5 Results from maximal center gauges

We have performed complementary studies of vortices both in the Direct and in the DMCG and IMCG (see section 2.9) respectively.

In the background of calorons we tried to confirm both dyon charge induced and twist-induced vortices seen in LCG. In DMCG, the dyon charge induced

vortices are observed and the twist induced part splits into several parts in adjacent time slices. Choosing the best among random gauge copies, the dyon charge induced part disappears and the twist-induced vortex bubble occurs at fixed time slice. In both cases, the bubble is much smaller than that found in LCG.

In IMCG, the situation for dyon charge induced vortices is rather stable: we find always a space-time vortex connecting the dyons or better to say the Abelian monopoles representing the dyons in MAG [68, 69]. Similar to the LCG doublet case two vortex lines pass near the center of mass of the caloron. This structure propagates either statically or non-statically in time, depending on the distance between dyons in the caloron.

Straight lines through the center of mass and through the outer space, as found in the LCG singlet case, were never observed. One can convince oneself, that it is actually impossible to get such vortex structures from $Z(2)$ link configurations.

The situation with twist-induced vortices is unstable, as a rule they do not appear in IMCG. The reason for this could be partially understood in IMCG considerations. Let us consider two gauge equivalent Abelian configurations that generate local Polyakov loops $\frac{1}{2}\text{Tr } \mathcal{P}(\vec{x}) = \cos(a(\vec{x}))$ and how their temporal links contribute to the Abelian gauge functional F_{IMCG} given in eqn. (2.89). In the quasi-temporal gauge when all subsequent temporal links are the same, they give a contribution equal to $N_t \cos(a(\vec{x})/N_t)^2$ to the corresponding part of the functional. When, on the other hand, all but one temporal links are trivial, the contribution is equal to $N_t - 1 + \cos(a(\vec{x}))^2$. For $\cos(a(\vec{x})) \neq -1$ and for sufficiently large N_t we have $N_t \cos(a(\vec{x})/N_t)^2 \simeq N_t - a(\vec{x})^2/N_t > N_t - \sin(a(\vec{x}))^2$. This means that after maximizing the functional (2.89) and projecting onto $Z(2)$, we get all temporal links trivial in all points \vec{x} where the Polyakov loop is not equal to -1 . So, the twist-induced vortex shrinks to one point where the (untraced) Polyakov loop is equal to -1_2 .

Maximization of the functional (2.89) is equivalent to the minimization of the functional

$$F[U] = \sum_{\mu, x} (\sin(\alpha\theta_\mu(x)))^2. \quad (3.13)$$

If we would replace it by the functional

$$F'[U] = \sum_{\mu, x} \sqrt{(\sin(\alpha\theta_\mu(x)))^2}. \quad (3.14)$$

the situation with the $Z(2)$ projected Polyakov loop would change because $N_t \sqrt{\sin(a(\vec{x})/N_t)^2} > \sqrt{\sin(a(\vec{x}))^2}$ on points where $\cos(a(\vec{x})) < 0$ and now we would have -1_2 temporal links in some time slice and trivial temporal links in all other time slices in the spatial region where the Polyakov loop is negative as well as trivial temporal $Z(2)$ links in all time slices in the region where the Polyakov loop is positive. Numerical studies support the appearance of twist-induced vortex on the boundary where initial Polyakov loop changes the sign from negative to positive.

One may conclude from this section that the Gribov copy problems of DMCG and IMCG persist for the smooth caloron backgrounds. The basic features of the vortices can be reproduced, but for clarity we stick to the vortices obtained in the Laplacian Center gauge.

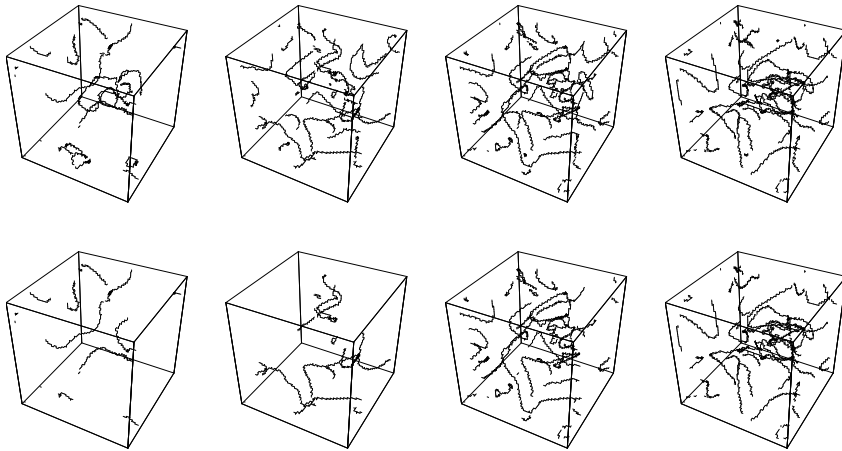


Figure 3.15: The space-time part of vortices in caloron ensembles in a fixed time slice. Only the holonomy varies from left to right: $\omega = \{0.0625, 0.0125, 0.01875, 0.25\}$ (from deconfined phase to confined phase). The upper row shows the entire vortex content in each caloron ensemble, the lower row shows the corresponding biggest vortex cluster.

3.4 Vortices in caloron ensembles

In this section we present the vortex content of ensembles of calorons. The generation of the latter has been described in section 3.1.1. We superposed 6 calorons and 6 anti-calorons with an average size of $\bar{\rho} = 0.6\beta$ on a 8×64^3 lattice.

The most important feature of these ensembles is their holonomy $\mathcal{P}_\infty = \exp(2\pi i \omega \sigma_3)$. In particular, caloron ensembles with maximally nontrivial holonomy $\omega = 1/4$ mimic the confined phase with $\langle \frac{1}{2} \text{Tr} L \rangle = 0$.

For each of the holonomy parameters $\omega = \{0.0625, 0.0125, 0.01875, 0.25\}$ we considered one caloron ensemble with otherwise equal parameters. Again we computed the lowest adjoint modes in these backgrounds and used the routines based on winding numbers to detect the LCG vortex contents.

In Figs. 3.15 and 3.16 we show the space-time part and the purely spatial part of the corresponding vortices as a function of the holonomy ω respectively. One can clearly see that *with holonomy approaching the confining value 1/4 the vortices grow in size, especially the spatial vortices start to percolate*, which will be quantified below.

Fig. 3.17 shows another view on this property. In these plots we have fixed one of the spatial coordinates to a particular value, such that vortices become line-like or remain surfaces (and may appear to be non-closed, when they actually close through other slices than the fixed one). These plots should be compared to Fig. 7 of Ref. [50], which however does not show a particular vortex configuration, but the authors' interpretation of measurements (in addition, the authors of [50] seem to have overlooked that vortices cut at fixed spatial coordinate still have surface-like parts, i.e. dual plaquettes).

We find that vortices in the deconfined phase tend to align in the time-like direction, while in the confined phase vortices percolate in the spatial directions. We remind the reader that we distinguish the different phases by the values of

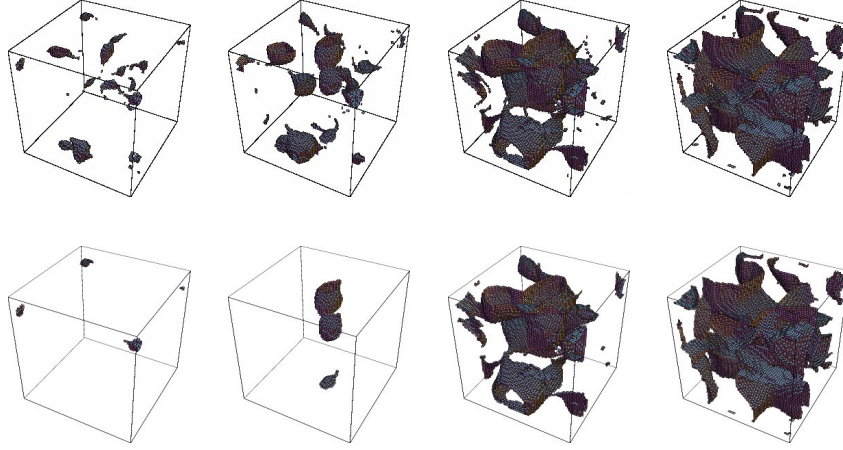


Figure 3.16: The spatial part of vortices in the caloron ensembles of Fig. 3.15 (with the same values of the holonomy ω) summed over all time slices. Again the upper row shows the entire vortex content and the lower row the corresponding biggest vortex cluster.

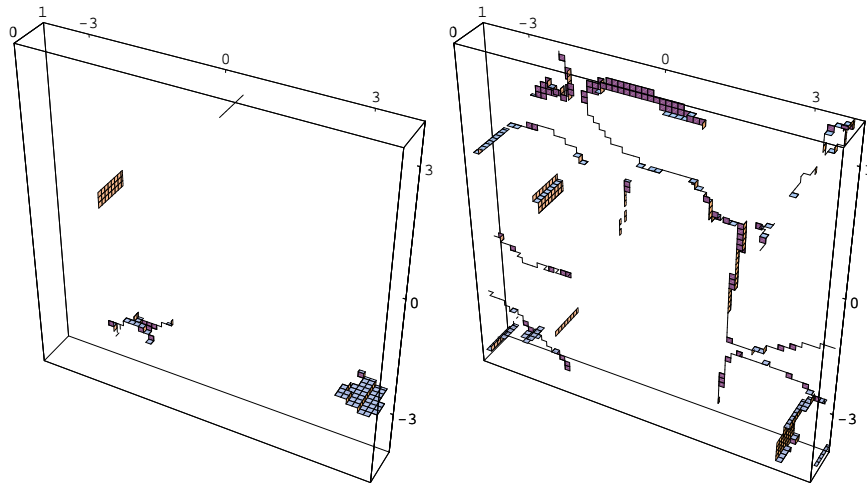


Figure 3.17: The vortex content of a caloron ensemble in the deconfined phase (left panel, mimicked by holonomy $\omega = 0.0625$ close to trivial) and in the confined phase (right panel, maximal nontrivial holonomy $\omega = 0.25$) in a lattice slice at fixed spatial coordinate. The short direction is x_0 while the other directions are the remaining spatial ones, all given in units of β .

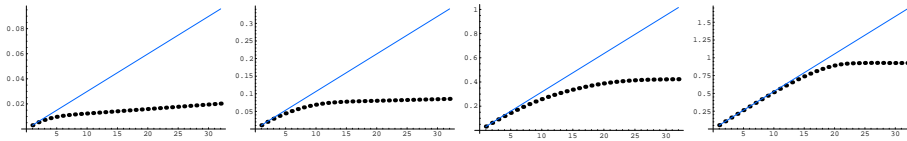


Figure 3.18: The observable $-\log\langle W(L, \beta) \rangle$ as a function of L in units of lattice spacing $a = \beta/8$ from vortices in caloron ensembles with holonomies as in Figs. 3.15 and 3.16 (from left to right: $\omega = \{0.0625, 0.0125, 0.01875, 0.25\}$). Note the very different scales. Percolating vortices, i.e. random penetrations, would give a linear behavior. The lines shown here are linear extrapolations of the first data point. The caloron vortices follow this line for longer and longer distances L when the holonomy approaches the confinement value $1/4$, thus inducing confinement in the Polyakov loop correlator (see text).

the holonomy, $\omega \simeq 0$, $\omega \simeq 1/2$ vs. $\omega = 1/4$, and not by different temperatures, which would lead to different caloron density and size distribution.

We start our interpretation of these results by the fact that the caloron background is dilute in the sense that the topological density is well approximated by the sum over the constituent dyons of individual calorons (of course, the long-range $A_\mu^{a=3}$ components still “interact” with the short-range $A_\mu^{a=1,2}$ components inside other dyon cores). Therefore it is permissible and helpful to interpret the vortices in caloron ensembles as approximate *recombination of vortices from individual calorons* presented in the previous sections.

Indeed, the space-time vortices resemble the dyon-induced vortices which are mostly space-time like and therefore line-like at fixed x_0 . The spatial vortices, on the other hand, resemble the twist-induced bubbles in individual calorons.

Following the recombination interpretation, the bubbles should become larger and larger when the holonomy approaches the confining holonomy $\omega = 1/4$, where they degenerate to flat planes. This is indeed the case in caloron ensembles: towards $\omega = 1/4$ the individual vortices merge to form one big vortex, see also the schematic plot Fig. 7 in [13]. In other words, *the maximal nontrivial holonomy has the effect of forcing the spatial vortices to percolate*. Consequently the vortices yield exponentially decaying Polyakov loop correlators, the equivalent of the Wilson loop area law at finite temperature (see below).

Note also that there is no similar scenario for the space-time vortices. The dyon-induced vortices in each caloron are either always as large as the lattice (in the singlet case) or are always confined to the interior of the caloron (in the doublet case). This is consistent with the physical picture, that spatial Wilson loops do not change much across the phase transition.

holonomy parameter	0.0625	0.125	0.1875	0.25
space-time extension	47	56	56	56
spatial extension	20	35	56	56

Table 3.1: Extensions of the largest vortex cluster (see text) in the caloron ensembles of Figs. 3.15 and 3.16. Note that the largest extension on a $8 \cdot 64^3$ lattice is $\sqrt{(8/2)^2 + 3 \cdot (32/2)^2} = 55.6$.

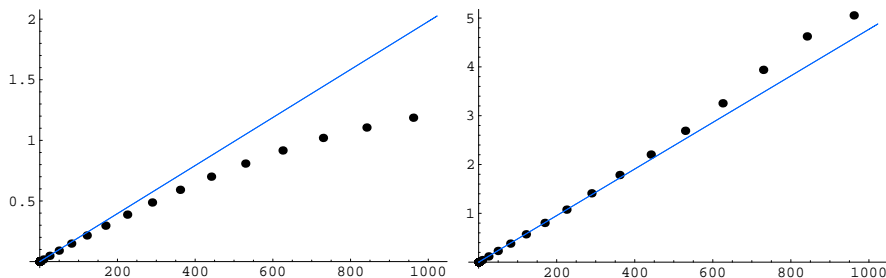


Figure 3.19: The observable $-\log\langle W(A) \rangle$ as a function of the area A in lattice units $a^2 = \beta^2/64$ from vortices in caloron ensembles with holonomy parameters $\omega = 0.0625$ (left) and $\omega = 0.25$ (right). Percolating vortices, i.e. random penetrations, would give a linear behavior. The lines shown here are linear extrapolations of the first data point.

In order to quantify the percolation we measured two observables. The first one concerns the spatial and space-time extensions of the largest vortices. We have included plots of them in the second row of Figs. 3.15 and 3.16 respectively.

For the spatial extension we superpose the purely spatial vortex plaquettes of all time slices in one 3d lattice, whereas for the space-time extension we remove all purely spatial vortex plaquettes. Then we pick the largest connected cluster in the remaining vortex structure.

Table 3.1 shows the extension of the largest spatial and space-time vortex clusters for different holonomy parameters of otherwise identical caloron ensembles. The purely spatial vortex cluster extension changes drastically with the holonomy parameter ω whereas the space-time one almost keeps to percolate.

The second row in Table 3.1 is related to confinement generated by vortices. If center vortices penetrate a Wilson loop with extensions T and L *randomly*, the probability to find n vortices penetrating the area $A = TL$ is given by the Poisson distribution (see eqn. (2.107))

$$P_r(n; T, L) = \frac{(pA)^n}{n!} e^{-pA} \quad (3.15)$$

as we described in eqn. (2.107), where p is the density of (spatial) vortices and the Wilson loop in such a center configuration obtains an area law with a string tension $\sigma = 2p$.

We explore space-time Wilson loops $\langle W(L, \beta) \rangle$, which amount to Polyakov loop correlators at distance L and probe confinement, as well as purely spatial Wilson loops as a function of their area, $\langle W(L, L') \rangle \equiv \langle W(A = LL') \rangle$. As Fig. 3.18 clearly shows, the values of $\log\langle W(L, \beta) \rangle$ show a confining linear behavior (like from random vortices) reaching longer and longer distances L when the holonomy approaches the confinement value $\omega = 1/4$. At the same time the corresponding string tensions also grow by an order of magnitude.

One can also explain the deviation from the confining behavior in holonomies far from $1/4$. The probability $P(2; L, \beta)$ for two vortices penetrating the Wilson loop is found much larger than in the case of Poisson distribution [not shown]. This comes from small bubbles, which very likely penetrate a given rectangular twice.

References [75, 50] found that the spatial Wilson loop by vortices keeps the area law in deconfined phase. Similarly the behavior of $\log\langle W(A) \rangle$ on the other hand changes only slightly for different holonomies, see Fig. 3.19. The corresponding slopes (“string tensions”) vary by a factor of approximately 2. For holonomy $\omega = 0.25$ we find an exponential decay stronger than proportional to the area. A quantitative analysis of this effect needs to include suitable caloron densities and size distributions around the critical temperature.

3.5 Summary

In this chapter we have extracted the vortex content of $SU(2)$ calorons and ensembles made of them, mainly with the help of the Laplacian Center Gauge, and studied the properties of the emerging vortices. Our main results are

(1) The constituent dyons of calorons induce zeroes of the lowest adjoint mode and therefore appear as monopoles in the Laplacian Abelian Gauge. The corresponding worldlines are either two static lines or one closed loop for large and small calorons, respectively.

(2) One part of the calorons’ vortex surface contains the dyon/monopole worldlines. The vortex changes its flux there (hence the surface should be viewed as non-orientable). These are general properties of LCG vortices. The specific shapes of these dyon-induced vortices depend on the caloron size as well as on the lattice extensions. These vortices are predominantly space-time like.

(3) Another part of the vortex surface consists of a “bubble” around one of the dyons, depending on the holonomy. The bubble degenerates into the mid plane of the dyon “molecule” in the case of maximal nontrivial holonomy $\omega = 1/4$. This part is predominantly spatial. We have argued that it is induced by the relative twist between different dyons in the caloron.

(4) Both parts of the vortex together reproduce the unit topological charge of the caloron by 2 intersection points with contributions 1/2.

(5) In dilute caloron ensembles – that differ only in the holonomy mimicking confined and deconfined phase – the vortices can be described to a good approximation by recombination of vortices from individual calorons. The spatial vortices in ensembles with deconfining holonomies $\omega \simeq 0$ form small bubbles. With the holonomy approaching the confinement value $\omega = 1/4$, the spatial bubbles grow and merge with each other, i.e. they percolate in spatial directions. We have quantified this by the extension of the largest cluster on one hand and by the quark-antiquark potential revealed by the Polyakov loop correlator on the other.

In particular the last finding is in agreement with the (de)confinement mechanism based on the percolation of center vortices.

Chapter 4

Vortices in $SU(3)$ calorons

4.1 $SU(N)$ calorons

As explored in the previous chapter, a unit charge $SU(2)$ caloron has two constituent monopoles (dyons) with a relative twist between. An $SU(N)$ unit charge caloron [76] [77] has N constituent monopoles. I will describe it in detail below.

$SU(N)$ calorons are also governed by the holonomy (Polyakov loop at spatial infinity) of the caloron, which we again diagonalise

$$P_\infty^0 = e^{2\pi i \mu \beta} = \text{diag}(e^{2\pi i \mu_1 \beta}, \dots, e^{2\pi i \mu_N \beta}). \quad (4.1)$$

where $2\pi\mu$ (we take $\beta = 1$ for simplicity) is the A_0 at infinity (in periodic gauge),

$$A_0(t, \vec{x} \rightarrow \infty) = 2\pi\mu \equiv 2\pi \text{diag}(\mu_1, \dots, \mu_N). \quad (4.2)$$

Without loss of generality, we can choose the ascending order of the μ 's, while the trace of μ vanishes.

$$\mu_1 \leq \mu_2 \leq \dots \leq \mu_{N-1} \leq \mu_N \leq \mu_{N+1} \equiv \mu_1 + 1, \quad \sum_{i=1}^N \mu_i = 0. \quad (4.3)$$

The difference of two adjacent μ 's, say μ_{m+1} and μ_m , is proportional to the mass of the m th constituent dyon: $\nu_m = \mu_{m+1} - \mu_m$. The (diagonalised) holonomy has $N - 1$ free parameters.

Parameters of an $SU(N)$ unit charge caloron also include the spatial locations of the constituent dyons \vec{y}_i , which are $3N$ free parameters. The last parameter is the period (β) of the $SU(N)$ caloron, which is here taken as 1 for convenience.

There are two different gauges for the caloron field A_μ , the algebraic gauge and the periodic gauge, the former one has a simple form while the later one is physical. The algebraic gauge means the caloron field A_μ is periodic up to the holonomy ($A_\mu(\beta, \vec{x}) = P_\infty^0 A_\mu(0, \vec{x}) P_\infty^{0\dagger}$). In this gauge, A_0 vanishes at infinity. We apply $V(t)$ to transform the gauge field to periodic gauge:

$${}^{per} A_\mu(x, t) = V(t) {}^{alg} A_\mu V^\dagger(t) - 2\pi i \mu, \quad V(t) = \exp(-2\pi i t \mu) \quad (4.4)$$

The caloron gauge field of a unit charge $SU(N)$ caloron in the algebraic gauge is

$${}^{alg}A_\alpha(x) = \frac{i}{2}\phi^{\frac{1}{2}}(x)C_\alpha(x)\phi^{\frac{1}{2}}(x) + \frac{i}{2}[\phi^{-\frac{1}{2}}(x), \partial_\alpha\phi^{\frac{1}{2}}(x)] \quad (4.5)$$

where C_α is an $N \times N$ matrix and ϕ is a positive definite $N \times N$ matrix, their definitions are

$$C_\alpha^{mk}(x) \equiv \zeta_m \bar{\eta}_{\alpha\beta} \zeta_k^\dagger \partial_\beta \hat{f}_x(\mu_m, \mu_k), \quad \phi_{mk}^{-1} \equiv \delta_{mk} - \zeta_m \zeta_k^\dagger \hat{f}_x(\mu_m, \mu_k). \quad (4.6)$$

The ζ , $\bar{\eta}$ and \hat{f} in the definitions of C and ϕ above are

$$\zeta_m^\dagger \zeta_m = \frac{|\vec{\rho}_m| \mathbf{1} - \vec{\rho}_m \cdot \vec{\tau}}{2\pi} \quad (4.7)$$

where $\vec{\rho}_m$ is the relative coordinate of the m th dyon to the $m-1$ th dyon ($\vec{\rho}_m \equiv \vec{y}_m - \vec{y}_{m-1}$). In $SU(3)$, without loss of generality, one can put all the constituent dyons on the $z=0$ plane and the formula for ζ_m becomes $\zeta_m = (|\vec{\rho}_m|, i\rho_m^2 - \rho_m^1) / \sqrt{2\pi|\vec{\rho}_m|}$. $\bar{\eta}_{\alpha\beta}$ is the self-dual 't Hooft tensor defined in eqn. (2.51). $\hat{f}_x(z, z')$ with $\mu_m \leq z' \leq z \leq \mu_{m+1}$ ($\hat{f}_x(z, z') = \hat{f}_x^*(z', z)$) is

$$\begin{aligned} \hat{f}_x(z, z') &= \frac{\pi e^{2\pi it(z-z')}}{r_m \psi} (e^{-2\pi it} \sinh(2\pi(z-z')r_m) \\ &\quad + \langle v_m(z') | A_{m-1} \dots A_1 A_N \dots A_m | \omega_m(z) \rangle) \end{aligned} \quad (4.8)$$

where $r_m = |\vec{x} - \vec{y}_m|$. A_m are 2×2 matrices:

$$A_m \equiv \frac{1}{r_m} \begin{pmatrix} r_m & |\vec{\rho}_{m+1}| \\ 0 & r_{m+1} \end{pmatrix} \begin{pmatrix} \cosh(2\pi\nu_m r_m) & \sinh(2\pi\nu_m r_m) \\ \sinh(2\pi\nu_m r_m) & \cosh(2\pi\nu_m r_m) \end{pmatrix}. \quad (4.9)$$

v_m and ω_m are column vectors

$$v_m(z') \equiv \begin{pmatrix} \sinh(2\pi(z' - \mu_m)r_m) \\ \cosh(2\pi(z' - \mu_m)r_m) \end{pmatrix}, \quad \omega_m(z) \equiv \begin{pmatrix} \cosh(2\pi(z - \mu_m)r_m) \\ -\sinh(2\pi(z - \mu_m)r_m) \end{pmatrix} \quad (4.10)$$

and finally ψ is:

$$\psi(x) \equiv \frac{1}{2} \text{Tr}(A_N \dots A_1) - \cos(2\pi t) \quad (4.11)$$

The $SU(N=2)$ caloron field A_μ formula degenerates to the caloron gauge field formulae in [26] which we have shown in section 2.7 if we put the constituent dyons on the z axis.

In [77], the definition of $\hat{f}_x(z, z')$ is only given for the $\mu_m \leq z' \leq z \leq \mu_{m+1}$ (and the $\mu_m \leq z \leq z' \leq \mu_{m+1}$) case, but it is enough for $SU(3)$, which only has 3 μ 's that any combination of 2 μ 's out of the 3 is an adjacent μ pair. $\hat{f}_x(\mu_1, \mu_3)$ is a bit different, it can be classified in the $\mu_N \leq z' \leq z \leq \mu_1 + 1 \equiv \mu_{N+1}$ case that

$$\hat{f}_x(\mu_1, \mu_3) = \frac{\pi e^{2\pi it\nu_3}}{r_3 \psi} (e^{-2\pi it} \sinh(2\pi\nu_3 r_3) + \langle v_3(\mu_3) | A_2 A_1 A_3 | \omega_m(\mu_1 + 1) \rangle). \quad (4.12)$$

The action density of an $SU(3)$ caloron has a simple form,

$$\text{Tr} F_{\mu\nu}^2(x) = \partial_\mu^2 \partial_\nu^2 \log \psi(x). \quad (4.13)$$

Generically, the action density has 3 lumps, corresponding to the 3 dyons.

These formulae will be used to discretize the caloron on a lattice (like we did in the previous chapter) followed by a numerical calculation of the Laplacian eigenmodes.

4.2 $SU(3)$ Laplacian center gauge and its ambiguity

Laplacian center gauge [41], as described in section 2.9.3, finds vortices as defects in the gauge fixing of lowest eigenmodes of the adjoint Laplacian operator in eqn. (2.92).

The adjoint representation is real, and the adjoint Laplacian operator and its eigenmodes are all real, the eigenmodes of adjoint representation can be taken as a column vector $\phi_a^{(i)}(x)$ or as a matrix $\Phi^{(i)}(x)$ whose gauge transformation is

$$\Phi^{(i)}(x) = \phi_a^{(i)}(x)T^a \quad \Phi^{(i)}(x) \xrightarrow{\Omega} \Phi^{(i)'}(x) = \Omega(x)\Phi^{(i)}(x)\Omega^\dagger(x) \quad (4.14)$$

where T^a are the generators of $SU(N)$ group. The adjoint matrix of a center element of $SU(N)$ gauge group is

$$U_A(Z_N^k) = \mathbf{1}_N \quad Z_N^k = e^{\frac{2\pi ki}{N}} \mathbf{1}_N. \quad (4.15)$$

So one can reduce the gauge symmetry from $SU(N)$ to Z_N by fixing the eigenmodes of the adjoint Laplacian operator which are blind to Z_N .

Let us consider the LCG [41]. LCG, as introduced in section 2.9.3, consists of two steps, the first step rotates the lowest eigenmode $\Phi^{(1)}(x)$ diagonal, which reduces the gauge symmetry from $SU(N)$ to $U(1)^{(N-1)}$, the Cartan subgroup, while the second mode is rotated to $\Phi^{(2)'}$ accordingly. The second step rotates $N-1$ non-diagonal entries of $\Phi^{(2)'}$ from complex numbers to positive real numbers, it reduces the symmetry from $U(1)^{(N-1)}$ to Z_N .

In $SU(3)$, the second mode after LCG is

$$\Phi^{(2)''} = \begin{pmatrix} \phi_3^{(2)'} + \frac{1}{\sqrt{3}}\phi_8^{(2)'}, & (\phi_1^{(2)'} - i\phi_2^{(2)'})e^{3i\alpha}, & (\phi_4^{(2)'} - i\phi_5^{(2)'})e^{3i(\alpha+\beta)} \\ (\phi_1^{(2)'} + i\phi_2^{(2)'})e^{-3i\alpha}, & -\phi_3^{(2)'} + \frac{1}{\sqrt{3}}\phi_8^{(2)'}, & (\phi_6^{(2)'} - i\phi_7^{(2)'})e^{3i\beta} \\ (\phi_4^{(2)'} + i\phi_5^{(2)'})e^{-3i(\alpha+\beta)}, & (\phi_6^{(2)'} + i\phi_7^{(2)'})e^{-3i\beta}, & -\frac{2}{\sqrt{3}}\phi_8^{(2)'} \end{pmatrix}, \quad (4.16)$$

which is the $\Phi^{(2)'}$ after we have applied

$$V(x) = \text{diag}(e^{2\alpha(x)+\beta(x)}, e^{i(-\alpha(x)+\beta(x))}, e^{-i(\alpha(x)+2\beta(x))}). \quad (4.17)$$

To the remaining symmetry of Cartan subgroup, which has two real parameters in $SU(3)$, one needs to gauge fix two of the non-diagonal entries of $\Phi^{(2)''}$ real and positive, which means choosing two of the three conditions below

$$\begin{aligned} \phi_1^{(2)''}(x) > 0 \quad \text{and} \quad \phi_2^{(2)''}(x) &= 0 \\ \phi_6^{(2)''}(x) > 0 \quad \text{and} \quad \phi_7^{(2)''}(x) &= 0 \\ \phi_4^{(2)''}(x) > 0 \quad \text{and} \quad \phi_5^{(2)''}(x) &= 0. \end{aligned} \quad (4.18)$$

Note that back to the $SU(2)$ case, $\Phi^{(2)''}$ has only one non-diagonal entry and the gauge fixing needs also only one condition.

Defects in the LCG procedure can occur in both steps. In the first step, points where $\Phi^{(1)}$ has degenerate eigenvalues are the defects. In $SU(3)$, the

diagonalized $\Phi^{(1)}$ is

$$\Phi^{(1)'}(x) = \begin{pmatrix} \phi_3^{(1)'}(x) + \frac{1}{\sqrt{3}}\phi_8^{(1)'}(x) & 0 & 0 \\ 0 & -\phi_3^{(1)'}(x) + \frac{1}{\sqrt{3}}\phi_8^{(1)'}(x) & 0 \\ 0 & 0 & -\frac{2}{\sqrt{3}}\phi_8^{(1)'}(x) \end{pmatrix}, \quad (4.19)$$

so the defects appear where one of the following conditions is fulfilled

$$\begin{aligned} \phi_3^{(1)'}(x) &= 0 \\ \phi_3^{(1)'}(x) &= \sqrt{3}\phi_8^{(1)'}(x). \end{aligned} \quad (4.20)$$

The number of real conditions for the defects in the first step of LCG seems to be one and the monopole world lines would be $D - 1$ dimensional. This is not true because the real condition number of this defect condition is actually not one. To see this, let us consider the $SU(2)$ case, where to take equal eigenvalues means that the matrix itself vanishes since ϕ as an element of the Lie algebra is traceless. So the equivalence of eigenvalues of an $su(2)$ matrix gives 3 real conditions. Let us return to the $SU(3)$ case and consider the first condition in eqn. (4.20). First, we can gauge fix two non-diagonal entries ($\Phi_{1,3}^{(1)}$ and $\Phi_{2,3}^{(1)}$) of $\Phi^{(1)}$ to 0, which is equivalent to rotating the third eigenvector to the third complex direction, then the first condition in eqn. (4.20) is equivalent to the vanishing of the remaining $su(2)$ sub-matrix, it gives 3 real conditions. Therefore the defect of the first step is a 1 dimensional line in 4 dimensional space-time, if one of the two conditions is satisfied, the local remaining gauge symmetry will be promoted to $SU(2)$. The same argument applies to the second condition in eqn. (4.20) whose defects give another kind of monopole in $SU(3)$.

The second step of the LCG procedure fixes $N - 1$ of the $N(N - 1)/2$ non-diagonal entries of $\Phi^{(2)''}$ real and positive. The defects of the second step occur where some of these entries vanish. Let us discuss the $SU(3)$ case in detail. We take the first and the second gauge fixing conditions in eqn. (4.18), means fixing $V(x)$ by rotate $\Phi_{1,2}^{(2)''} = (\phi_1^{(2)'}(x) - i\phi_2^{(2)'}(x))e^{3i\alpha}$ and $\Phi_{2,3}^{(2)''} = (\phi_6^{(2)'}(x) - i\phi_7^{(2)'}(x))e^{3i\beta}$ real positive. It gives

$$\begin{aligned} \alpha(x) &= \frac{1}{3} \arg(\phi_1^{(2)'}(x) + i\phi_2^{(2)'}(x)) \\ \beta(x) &= \frac{1}{3} \arg(\phi_6^{(2)'}(x) + i\phi_7^{(2)'}(x)). \end{aligned} \quad (4.21)$$

If one of these two non-diagonal entries of $\Phi^{(2)'}$ vanishes

$$\phi_1^{(2)'}(x) + i\phi_2^{(2)'}(x) = 0 \quad \text{or} \quad \phi_6^{(2)'}(x) + i\phi_7^{(2)'}(x) = 0, \quad (4.22)$$

we can not fix $V(x)$, and the remaining gauge symmetry is $U(1)$ instead of Z_3 , the number of real conditions is 2. Therefore the defects of the second step form a $2 = 4 - 2$ dimensional vortex surface in the 4 dimensional space-time. So far, the center projection works as it should.

However, Laplacian center gauge in $SU(N)$ ($N \geq 3$) has an ambiguity:

In higher $SU(N)$ gauge groups ($N \geq 3$) like $SU(3)$, the second step of the LCG has $N - 1$ conditions, rotates $N - 1$ of the $N(N - 1)/2$ non-diagonal

entries of $\Phi^{(2)'}$ real positive. The vanishing of any of these $N - 1$ conditions gives a vortex. This immediately leads to the question, how to choose $N - 1$ conditions from the $N(N - 1)/2$. In $SU(2)$, this ambiguity does not occur because $N - 1 = N(N - 1)/2 = 1$, but in $SU(3)$, the number of non-diagonal entries becomes 3 while the number of remaining $U(1)$ symmetries is 2. As there is no restriction on the non-diagonal entries of $\Phi^{(2)'}$ like

$$\arg(\Phi_{1,2}^{(2)'}) + \arg(\Phi_{2,3}^{(2)'}) + \arg(\Phi_{3,1}^{(2)'}) = 0 \quad (4.23)$$

to assure different choices of entries give the same vortices, different choices of the $N - 1$ conditions in $SU(N)$ LCG give different results. In the next section, we will see the consequences of this ambiguity in the vortex contents of $SU(3)$ calorons.

This ambiguity in $SU(3)$ or higher gauge groups can be viewed in another aspect. In the end of section 2.9.3, the argument for the existence of center vortices in $SU(2)$ was made explicit by the $\frac{i}{g}V\partial_\mu V^\dagger$ contribution of the gauge fixing transformation V around the defects where $\Phi_{1,2}^{(2)'}(x_V) = 0$. But in $SU(3)$, it has an ambiguity. Without loss of generality, let us choose the two conditions in eqn. (4.22). If the first condition of eqn. (4.22) is satisfied on x_V : $\Phi_{1,2}^{(2)'}(x_V) = 0$, like we argued in section 2.9.3, we find a plane through x_V on which $\Phi_{1,2}^{(2)'} = f(r)\exp(i\theta)$ near x_V . So the $SU(3)$ gauge fixing transformation V is $V(\theta) = \exp\{\text{diag}[i(2\theta/3 + \beta), i(-\theta/3 + \beta), i(-\theta/3 - 2\beta)]\}$ which is not completely fixed and does not give a definite $\frac{i}{g}V\partial_\mu V^\dagger$ contribution. Because of this ambiguity, we can not reproduce the arguments for the existence of center vortices as we did in $SU(2)$, and the flux penetrating the defect has an ambiguity.

This ambiguity can be fixed if the other condition is also satisfied. But because each condition of eqn. (4.22) gives two real conditions, the defects where both conditions are satisfied form a $D - 4$ dimensional object, this does not fit the vortex surface dimension of $D - 2$.

In our private communications with Ph. de Forcrand, one of the inventors of Laplacian center gauge in [41], he acknowledged that different choices of the $N - 1$ conditions give different vortices, but also expected that their existence is choice independent. The smooth and well-understood background of $SU(3)$ calorons should therefore be a good test to investigate the consequences of the ambiguity for vortex mechanisms.

4.3 Twists and vortices in $SU(3)$ calorons

In section 3.3, we have found that there are two part of vortices in $SU(2)$ calorons, the magnetic flux between the two dyons forms the space-time part, monopole world lines resides on this part. The second part, whose percolation is related to the confinement in Polyakov loop correlators, is induced by the relative twists between the dyons.

Furthermore, we have found the lowest Laplacian modes inherit the twists in the gauge field, and so does $\Phi^{(2)'}$. This is the reason why the boundary of twists implies purely spatial vortices as we presented there.

The structure of an $SU(3)$ caloron is similar to that of an $SU(2)$ caloron. It is composed of dyons and there are twists, so in particular, the purely spatial vortices should occur and be related to the boundary of twists.

The twists in $SU(3)$ caloron can be revealed in the gauge field ${}^{per}A_\mu$ in eqn. (4.4). It is immediately clear that both ingredients ϕ and C are given in terms of the \hat{f} in which we will identify the twists in the caloron (in section 2.7.2, we identified the twists in $SU(2)$ calorons also by \hat{f}).

Let us specify the $SU(3)$ formulae for \hat{f} from section 4.1 (algebraic gauge):

$$\begin{aligned} f_{2,1} &\equiv \hat{f}_x(\mu_2, \mu_1) = \frac{\pi e^{2\pi i \nu_1 t}}{r_1 \psi} \left(e^{-2\pi i t} s_1 + \frac{r_1}{r_3} \left(s_3 \left(c_2 + \frac{\rho_3}{r_2} s_2 \right) + \frac{r_3}{r_2} c_3 s_2 \right) \right) \\ f_{3,2} &\equiv \hat{f}_x(\mu_3, \mu_2) = \frac{\pi e^{2\pi i \nu_2 t}}{r_2 \psi} \left(e^{-2\pi i t} s_2 + \frac{r_2}{r_1} \left(s_1 \left(c_3 + \frac{\rho_1}{r_3} s_3 \right) + \frac{r_1}{r_3} c_1 s_3 \right) \right) \\ f_{1,3} &\equiv \hat{f}_x(\mu_1, \mu_3) = \frac{\pi e^{2\pi i \nu_3 t}}{r_3 \psi} \left(e^{-2\pi i t} s_3 + \frac{r_3}{r_2} \left(s_2 \left(c_1 + \frac{\rho_2}{r_1} s_1 \right) + \frac{r_2}{r_1} c_2 s_1 \right) \right) \end{aligned} \quad (4.24)$$

where $s_i = \sinh(2\pi \nu_i r_i)$, $c_i = \cosh(2\pi \nu_i r_i)$ and $r_i = |\vec{x} - \vec{y}_i|$.

The twists should be identified in the periodic gauge, which will give additional factors of $e^{-2\pi i \nu_1 t}$, $e^{-2\pi i \nu_2 t}$ and $e^{2\pi i t - 2\pi i \nu_1 t}$ to $f_{2,1}$, $f_{3,2}$ and $f_{1,3}$ respectively. In the asymptotic limit where the distance to all dyons become large ($r_i \rightarrow \infty$), the \hat{f} s become:

$$\begin{aligned} f_{2,1} &\propto e^{-2\pi i t} K_1 + O(r_1, r_2, r_3, \rho_3) K_2 K_3 \\ f_{3,2} &\propto e^{-2\pi i t} K_2 + O(r_2, r_3, r_1, \rho_1) K_3 K_1 \\ f_{1,3} &\propto K_3 + O(r_3, r_1, r_2, \rho_2) e^{2\pi i t} K_1 K_2 \end{aligned} \quad (4.25)$$

where $K_i = e^{2\pi \nu_i r_i}$ and O s are fractional functions of r_i and ρ . So the twists in the off-diagonal gauge field entries A_{21} , A_{32} and A_{13} in the $r_i \rightarrow \infty$ limit (far from all dyons) are:

$$\begin{aligned} T(A_{21}) &= \begin{cases} -1 & \text{for } \nu_1 r_1 > \nu_2 r_2 + \nu_3 r_3 \\ 0 & \text{for } \nu_1 r_1 < \nu_2 r_2 + \nu_3 r_3 \end{cases} \\ T(A_{32}) &= \begin{cases} -1 & \text{for } \nu_2 r_2 > \nu_3 r_3 + \nu_1 r_1 \\ 0 & \text{for } \nu_2 r_2 < \nu_3 r_3 + \nu_1 r_1 \end{cases} \\ T(A_{13}) &= \begin{cases} 0 & \text{for } \nu_3 r_3 > \nu_1 r_1 + \nu_2 r_2 \\ 1 & \text{for } \nu_3 r_3 < \nu_1 r_1 + \nu_2 r_2 \end{cases} \end{aligned} \quad (4.26)$$

where $T(A)$ is the twist (winding number) in temporal direction, a field of $\phi = e^{2\pi i t}$ has a twist of 1.

Let us consider some special cases. The first one is moving one of the dyons to infinity. If we move the third dyon, which means $r_3 \rightarrow \infty$, the twists in the rest part of the caloron is $T(A_{21}) = T(A_{32}) = T(A_{13}) = 0$, i.e. the rest of the caloron becomes static. If we move the second dyon, the result is a bit different, $T(A_{21}) = 0$, $T(A_{32}) = -1$, $T(A_{13}) = 1$, which means the rest of the caloron is static up to a global gauge transformation $V_1 = \exp[\text{diag}(\frac{2\pi i}{3}, \frac{2\pi i}{3}, -\frac{4\pi i}{3})t]$. Similarly, if we move the first dyon to infinity, we get $T(A_{21}) = -1$, $T(A_{32}) = 0$, $T(A_{13}) = 1$, and the rest part of the caloron is static up to a global gauge transformation $V_2 = \exp[\text{diag}(\frac{4\pi i}{3}, -\frac{2\pi i}{3}, -\frac{2\pi i}{3})t]$. At first, the twist consideration seems to distinguish the third dyon from the others. However, the periodic gauge we used so far is not unique, In $SU(3)$ we can apply the gauge transformations $\exp[\text{diag}(\frac{-2\pi i t}{3}, \frac{-2\pi i t}{3}, \frac{4\pi i t}{3})]$ or $\exp[\text{diag}(\frac{4\pi i t}{3}, \frac{-2\pi i t}{3}, \frac{-2\pi i t}{3})]$ which are exactly the V_1 and V_2 , to the caloron (these transformations keep the gauge

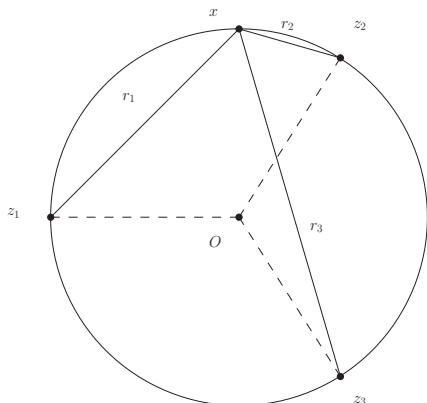


Figure 4.1: The 3 twist boundary conditions $r_i = r_j + r_k$ do not wrap any finite volume but shrink to a circle around the center of mass.

field periodic and plaquettes invariant). These transformations exchange the roles of the dyons, e.g. which one to move to infinity to end up a static rest. It shows that none of the dyons is special, their relation is democratic.

In the second case, we put the 3 dyons on the corners of an equilateral triangle and the dyons of equal weights $\nu_i = \frac{1}{3}$. In this case, there is no region in space satisfying $r_i > r_j + r_k$, but there are 3 curves with $r_i = r_j + r_k$ as shown in Fig. 4.1. It is easy to prove that these 3 curves form a circle around the center of mass that all the dyons sit on. As the condition of the twist boundaries in eqn. (4.26) are approximate conditions in the $r_i \rightarrow \infty$ limit, the vortices we get by LCG procedures – numerically calculate the lowest modes and find defects in the second step of LCG – do not degenerate to this circle but become small bubbles around the corresponding $r_i = r_j + r_k$ curves, as shown in Fig. 4.2.

We can move one of the dyons a bit in the last case, toward the center of the equilateral triangle or in the opposite direction. The twist boundaries of these two cases are shown in Fig. 4.3 and Fig. 4.4 respectively, the former consists of two surfaces from $T(A_{2,1})$ and $T(A_{3,2})$ and the latter consists of one surface from $T(A_{1,3})$.

The third case is that the weight of one dyon is $1/2$, equal to the sum of weights of the other two dyons. As shown in Fig. 4.5, the twist boundary of one of the entries is close to a plane while the twist boundaries of the other two entries vanish. This is very similar to our $SU(2)$ purely spatial vortices, in which case the weight of the two dyons are equal.

Fig. 4.3, 4.4 and 4.5 are twist boundaries by eqn. (4.26). The LCG vortices follow the expectations up to some deformations, compare Fig. 4.1 with Fig. 4.2. and Fig. 4.5 with Fig. 4.6.

As we mentioned in section 4.2, Laplacian center gauge suffers from an ambiguity as one needs to choose 2 of the 3 non-diagonal entries of $\Phi^{(2)'}$, and the corresponding zero points of the 2 entries are vortices. From Fig. 4.2 we see that different choices gives different vortex contents indeed, also the twist boundaries of different non-diagonal entries do not coincide with each other.

From the twist analysis above we see that, different from the $SU(2)$ case in which the twist centers coincide with the dyon centers, in $SU(3)$ the twist

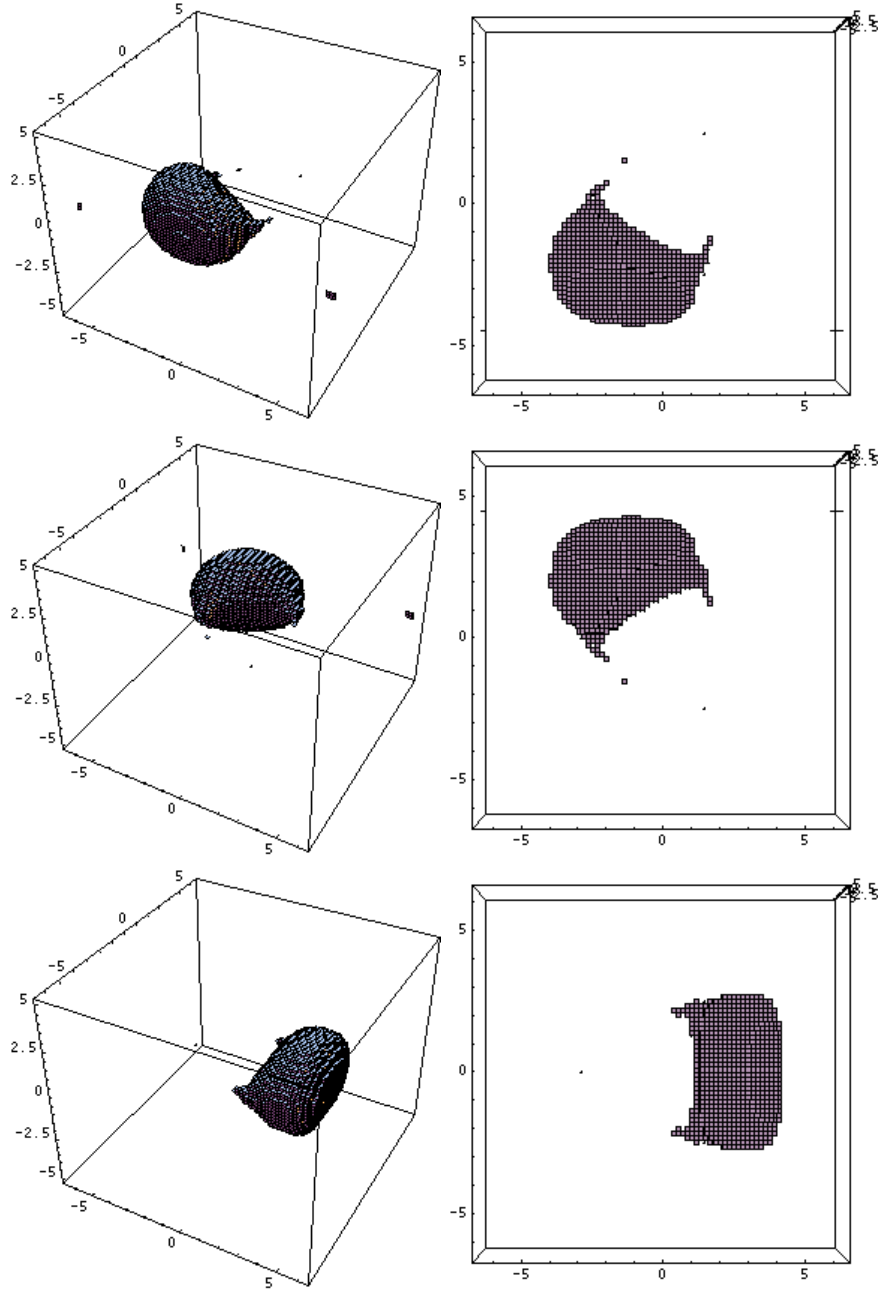


Figure 4.2: The possible vortices of an $SU(3)$ caloron with $\nu_1 = \nu_2 = \nu_3 = 1/3$, $y_1 = (3/2, 3\sqrt{3}/2, 0)$, $y_2 = (3/2, -3\sqrt{3}/2, 0)$ and $y_3 = (-3, 0, 0)$. The upper panel shows the vortices we get from $\Phi_{21}^{(2)'}$, the middle and lower panel shows those from $\Phi_{32}^{(2)'}$ and $\Phi_{13}^{(2)'}$, respectively. The right column gives the top view of the left column.

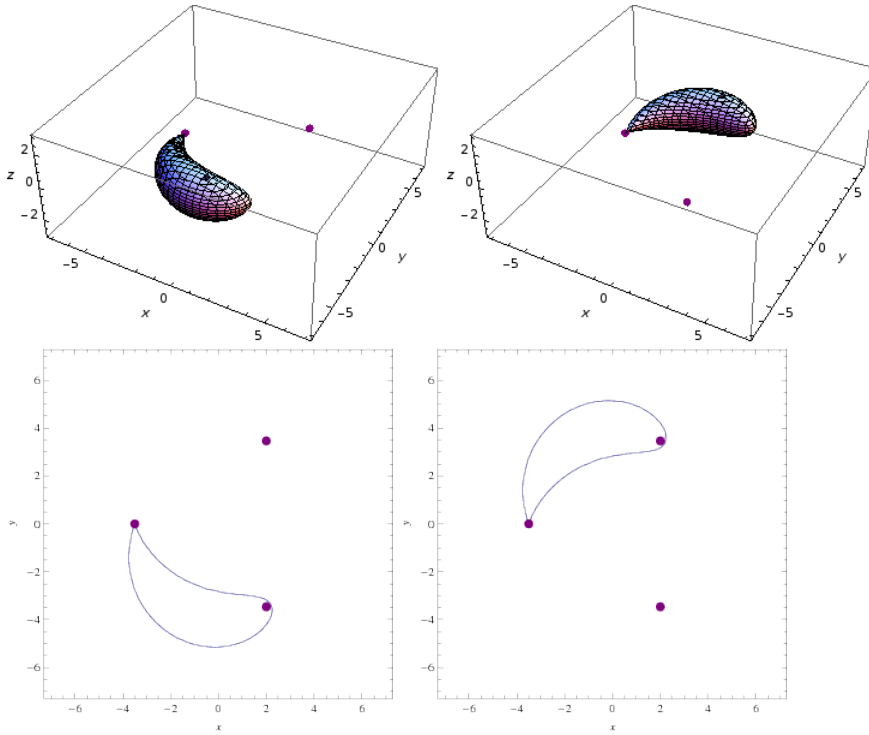


Figure 4.3: The twist boundaries of an $SU(3)$ caloron of equal weight dyons, $\nu_1 = \nu_2 = \nu_3 = 1/3$, at locations $y_1 = \{2, 2\sqrt{3}, 0\}$, $y_2 = \{2, -2\sqrt{3}, 0\}$ and $y_3 = \{-3.5, 0, 0\}$ as marked by the violet points. The third dyon is closer to the center of the triangle. The first row shows 3D views of twist boundaries and the second row shows corresponding intersections with the plane $z = 0$. The first column and the second column are the twist boundary of $T(A_{2,1})$ and $T(A_{3,2})$, respectively, while the twist boundary of $T_{1,3}$ vanishes. The twists within the two bubbles are -1 .

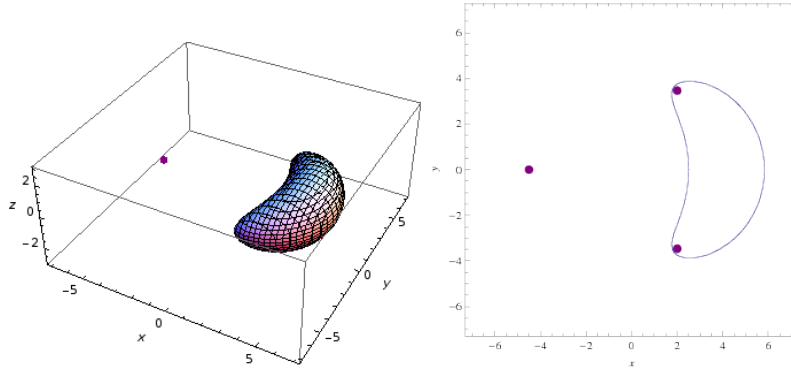


Figure 4.4: The twist boundaries of an $SU(3)$ caloron of equal weight dyons, $\nu_1 = \nu_2 = \nu_3 = 1/3$, at locations $y_1 = \{2, 2\sqrt{3}, 0\}$, $y_2 = \{2, -2\sqrt{3}, 0\}$ and $y_3 = \{-4.5, 0, 0\}$ as marked by the violet points. The third dyon is a bit further away from the center of the triangle. The left panel shows the 3D view of $T(A_{1,3})$ twist boundaries and the right shows the corresponding intersection with the plane $z = 0$. The other two twist boundaries vanish. The twist within the bubble is 0 and is +1 outside of it.

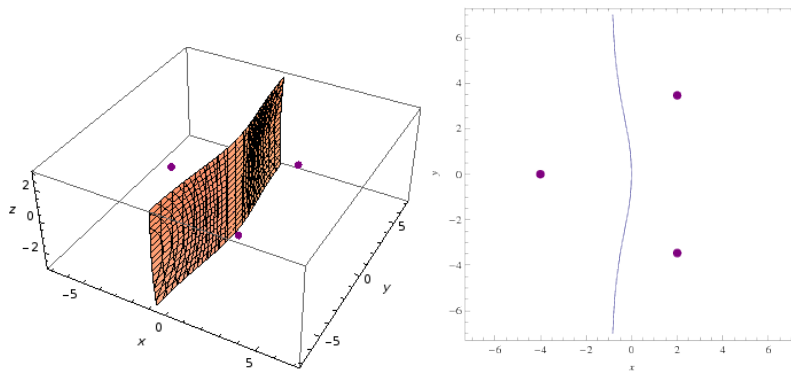


Figure 4.5: The twist boundaries of $T(A_{1,3})$ of an $SU(3)$ caloron with dyons of different weights, $\nu_3 = 1/2$ and $\nu_1 = \nu_2 = 1/4$, at locations $y_1 = \{2, 2\sqrt{3}, 0\}$, $y_2 = \{2, -2\sqrt{3}, 0\}$ and $y_3 = \{-4, 0, 0\}$ as marked by the violet points. The dyons are in the corners of an equilateral triangle.

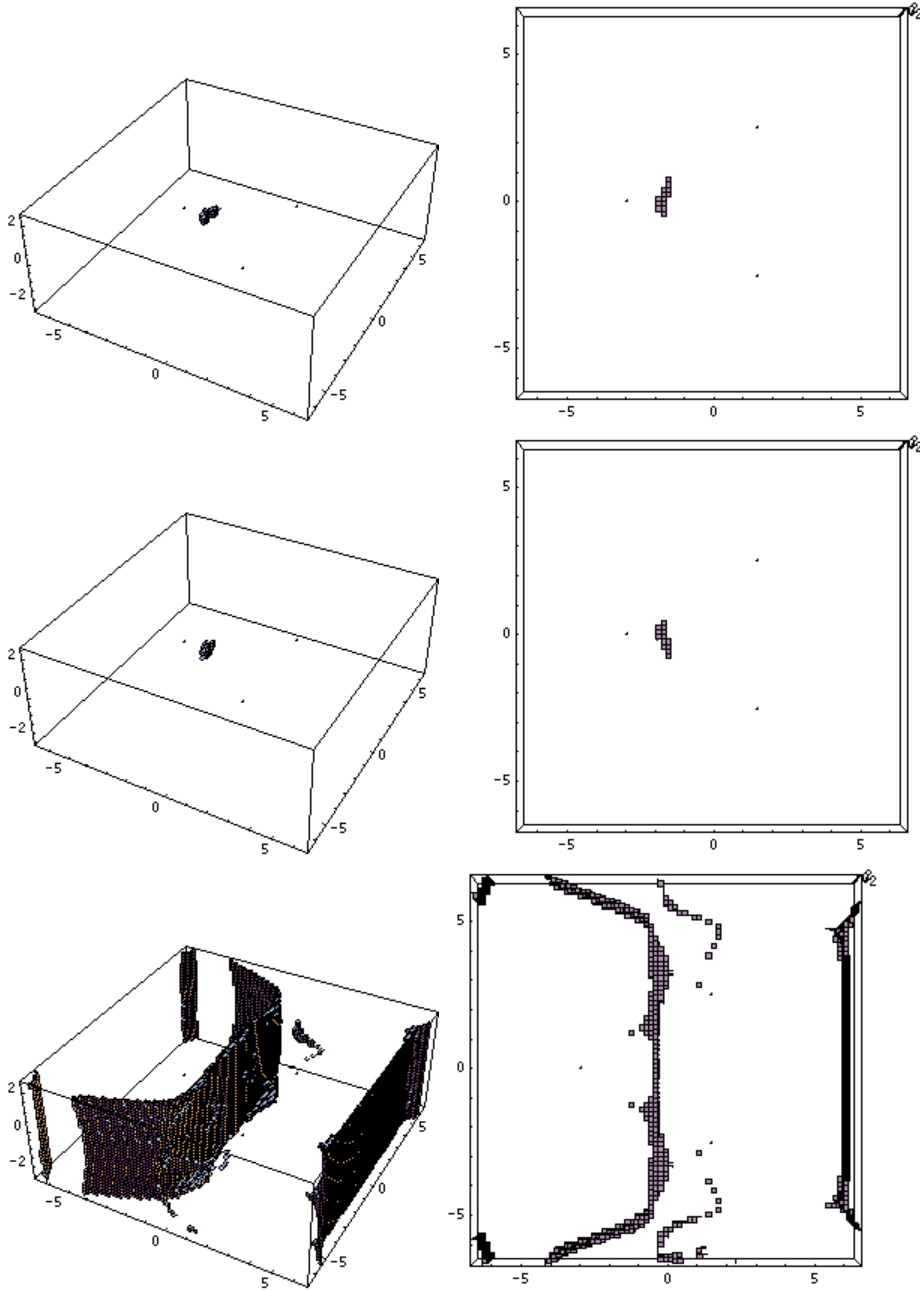


Figure 4.6: The possible vortices of an $SU(3)$ caloron with $\nu_1 = \nu_2 = 1/4$, $\nu_3 = 1/2$, $y_1 = (1, \sqrt{3}, 0)$, $y_2 = (1, -\sqrt{3}, 0)$ and $y_3 = (-2, 0, 0)$. The upper panel shows the vortices we get from $\Phi_{21}^{(2)'}$, the middle and lower panel shows that from $\Phi_{32}^{(2)'}$ and $\Phi_{13}^{(2)'}$ respectively. The right column gives the top view of the left column. The last row has an artefact plane and some deformation near the boundary as the lattice is periodic.

centers (in our case are the volumes wrapped by the twist boundaries in Fig. 4.3, Fig. 4.4 and Fig. 4.2) are *between* the dyon centers, and the accumulated twist of one period $T(\beta)$ of the 3 twist centers are the 3 center elements of $SU(3)$ gauge field.

In $SU(2)$, it is very clear that just the calorons composed of equal weight dyons extend their purely spatial vortices to infinity which eventually in caloron ensembles yields percolations just in the confined phase. But how can we relate the $SU(3)$ caloron vortices with the different phases? We know that the calorons in the confined phase should possess equal weight dyons ($\nu_1 = \nu_2 = \nu_3 = 1/3$), because the trace of Polyakov loop vanishes in this phase. However, the vortices we get for such $SU(3)$ calorons in Fig. 4.2 are finite size bubbles.

The answer might be that the vortices in $SU(3)$ calorons are not thin vortices, as we see that twist boundaries of different $\Phi^{(2)'}$ entries do not coincide with each other. If we consider a big “plaquette” across two of the twist boundaries, say that of $\Phi_{1,2}^{(2)'}$ and $\Phi_{2,3}^{(2)'}$, then on this plaquette there are two zeros of $\Phi_{1,2}^{(2)'}$ and $\Phi_{2,3}^{(2)'}$ respectively, so that the V around this plaquette is completely determined, and the $\frac{i}{g}V\partial_\mu V^\dagger$ contribution through A_μ to the Wilson loop around this big plaquette is a center element of $SU(3)$, and the argument for center vortices stands.

Chapter 5

Dual condensate and dual quark density

In the QCD phase transition at finite temperature, the most important phenomena are deconfinement and chiral symmetry restoration. As we discussed in Chapter 1, order parameters for these effects are the Polyakov loop and the chiral condensate.

But how to connect confinement and chiral symmetry breaking? Or how to connect order parameters of the two phenomena? In [11, 12] a novel order parameter has been given, the dual condensate. It is the first Fourier component of the quark condensate with respect to the boundary conditions. On the other hand, it is sensitive to center symmetry like the Polyakov loop. We will discuss the connection and the details of dual condensate in the next section, show our numerical results of the dual condensate on dynamical lattice configurations [8] using staggered fermions and explore a new dual operator, the dual quark density, theoretically and numerically. Unsmearred dual condensate results can be found in our proceedings [82].

5.1 Dual condensate and dressed Polyakov loop

5.1.1 Definitions and mechanisms

The chiral condensate, the massless limit of the quark condensate, is an important order parameter of QCD phases. It breaks chiral symmetry spontaneously as we mentioned in Chapter 1.

More generally, the quark condensate is the trace of quark propagator as

$$\begin{aligned}\langle \bar{\psi}\psi \rangle &= \frac{\int dA \int d\bar{\psi}d\psi \bar{\psi}(x)\psi(x)e^{-i \int d^4x \bar{\psi}(D+m)\psi + \dots}}{V_4 Z} \\ &= \frac{\int dA \text{Tr} \left(\frac{1}{D+m} \right)_{xx} e^{-iS}}{V_4 Z} = \frac{1}{V_4} \langle \text{Tr} \frac{1}{D+m} \rangle\end{aligned}\quad (5.1)$$

On the lattice, the quark condensate as the trace of quark propagator, can be obtained in two different ways. The first way estimates $\text{Tr} (D + m)^{-1}$ by iterative steps using stochastic vectors, see e.g. [78]. The second method which

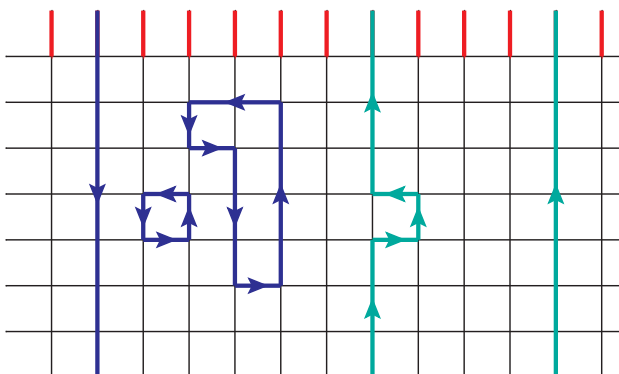


Figure 5.1: Loops with different powers of the boundary condition introduced phase $e^{i\phi}$, horizontal lines are spatial links, vertical lines are temporal links. Blue and green lines represent closed loops but only the green loops have winding number 1 in the compact time.

we will adopt uses the spectral representation of the quark propagator:

$$\text{Tr} \frac{1}{D + m} = \sum_{\lambda} \frac{1}{i\lambda + m}. \quad (5.2)$$

where $i\lambda$ are eigenvalues of the massless Dirac operator D that need to be measured. The result is dominated by the infrared part of the spectrum. Consider the fact that D is anti-Hermitian and anti-commutes with γ_5 , which means the eigenvalues of D are imaginary and in $\pm i\lambda$ pairs, we have

$$\text{Tr} \frac{1}{D + m} = \sum_{\lambda > 0} \frac{2m}{\lambda^2 + m^2}. \quad (5.3)$$

It is clear that the ultraviolet contributions are suppressed by the denominator. In the massless limit, the term in the sum approaches $\delta(\lambda)$. Hence the chiral condensate is given by the eigenmode density at $\lambda = 0$, $\rho(0)$, which is the famous Banks-Casher relation [57].

The physical quark boundary condition without (imaginary) chemical potential is the anti-periodic boundary condition

$$\psi(t + \beta) = -\psi(t). \quad (5.4)$$

The idea of [11] is to apply general phase boundary conditions. Then the corresponding quark condensate is the general quark condensate [12, 92]

$$\begin{aligned} \psi_{\phi}(t + \beta) &= e^{i\phi} \psi_{\phi}(t) \\ D_{\phi} \psi_{\phi} &= \pm i\lambda_{\phi} \psi_{\phi} \\ \Sigma(m, V, \phi) &\equiv \langle \text{Tr} \frac{1}{D_{\phi} + m} \rangle = \frac{1}{V} \langle \sum_{\lambda_{\phi}} \frac{1}{i\lambda_{\phi} + m} \rangle. \end{aligned} \quad (5.5)$$

These boundary conditions are similar to an imaginary chemical potential of $\mu_I = i(\phi - \pi)T$, however, they are only applied on the valence quarks. Likewise, the probe mass m does not need to agree with the mass of sea quarks.

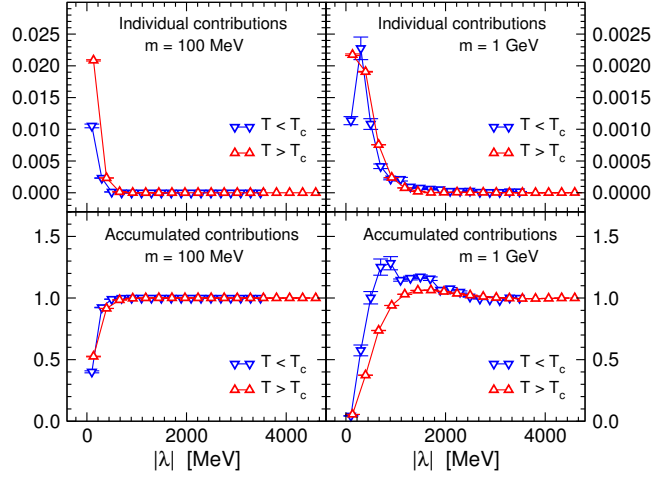


Figure 5.2: Individual and accumulated contributions to the (quenched) dual condensates from different parts of the spectra by Bilgici et al [12].

On the lattice, one can implement the general boundary condition by giving an additional phase ϕ to all the temporal links in the last time slice,

$$U(N_t, \vec{x}) \rightarrow e^{i\phi} U(N_t, \vec{x}), \quad (5.6)$$

visualised by the red lines in Fig. 5.1.

If the mass is large enough, one can expand the expression of general quark condensate in eqn. (5.5) like:

$$\Sigma(m, V, \phi) = \left\langle \text{Tr} \frac{1}{D + m} \right\rangle = \frac{1}{m} \left\langle \sum_{i=0}^{\infty} \frac{(-1)^i \text{Tr}(D^i)}{(m)^i} \right\rangle. \quad (5.7)$$

$\text{Tr}(D^i)$ in this expansion tells us that only closed loops contribute. Also in general, the general quark condensate $\Sigma(m, V, \phi)$ consists of closed loops only, because it is a gauge invariant functional of the links. Moreover, $\text{Tr}(D^i)$ contains loops of length i (provided D contains just nearest neighbor links), these loops are suppressed by factors $(2am)^i$ (with $1/2a$ coming from the Dirac operator, cf. eqn. 5.44).

Through the implementation of the general boundary condition in eqn. (5.5), closed loops get different powers of the boundary condition induced phase $e^{i\phi}$, and the power of $e^{i\phi}$ is its winding number in time direction as shown in Fig. 5.1.

Dual condensates are defined to be the Fourier components of the general quark condensates with respect to ϕ [11]:

$$\tilde{\Sigma}_k(m, V) = \frac{1}{2\pi} \int_0^{2\pi} d\phi e^{-ik\phi} \Sigma(m, V, \phi), \quad (5.8)$$

picking out closed loops of winding number k . In particular, the first Fourier component $\tilde{\Sigma}_1$ is the “dressed Polyakov loop”, shown in Fig. 5.1 as green lines. It follows immediately that $\tilde{\Sigma}_1$ transforms under the center symmetry transformations like the Polyakov loop.

In the large mass limit, the leading term of the dual condensate is $\text{Tr}(D^{N_t})/m^{N_t}$ where N_t is the time direction size of the lattice. The leading contributions to dual condensates are from the straight closed loops with winding number one, the conventional Polyakov loops, see also [79]. Given that the dual condensate includes contributions of longer loops of the same winding number (at higher orders of inverse mass), it can be interpreted as a “dressed Polyakov loop”.

Another important aspect of the dual condensate is its IR dominance. We know that the quark condensates are IR dominated (especially the chiral condensate). The dual condensate, which is the first Fourier component of the general quark condensate, reflects the boundary condition phase dependence of it. Given that the spectra of D_ϕ with different ϕ 's mainly differ in the lowest part, the dual condensate is even stronger IR dominated [82]. Fig. 5.2 shows that the dominating contributions are from the infrared part of the spectrum.

The renormalization of the quark condensate [9] is

$$\Sigma_R = m_q(\Sigma_B(T) - \Sigma_B(T = 0)), \quad (5.9)$$

where m_q is the bare quark mass, or normalize it to be dimensionless by m_X^4 where m_X is a dimension 1 constant. The bare dual condensate vanishes in the confined phase as $\Sigma_B(\phi)$ is a flat curve there, we can see this in section 5.5.1. Consider $\tilde{\Sigma}_B(T = 0) = 0$, the renormalized dual condensate becomes

$$\tilde{\Sigma}_{1R}(T) = m_q \tilde{\Sigma}_{1B}(T), \quad (5.10)$$

We know that the Polyakov loop is proportional to $e^{-\beta F}$ where F is the free energy of an infinitely heavy quark, so $-\frac{1}{\beta} \ln L = F(T) + c$ reflects the change of free energy. As the dual condensate is proportional to the dressed Polyakov loop, we will also measure

$$-\frac{1}{\beta} \ln(\tilde{\Sigma}_{1R}/m_X^4) = F'(T) + c + 4T \ln m_X, \quad (5.11)$$

which is an analogue of the free energy.

Former results of the quenched dual condensates in [12] and [80], preliminary unquenched $SU(3)$ results in [81] and our unquenched $SU(3)$ results of unsmear dual condensates in [82] confirm that the dual condensate is an infrared dominated order parameter.

5.1.2 Applications beyond the lattice and in other gauge systems

There have been other investigations using the dual condensate to get a handle on the phase transition in QCD and related gauge systems, which are briefly summarized in this section.

By functional renormalization group methods, Braun et al. have computed the partition function at imaginary chemical potential as well as the dual condensates [96].

Through Dyson-Schwinger equations, Fischer and Müller have incorporated the boundary angle into the quark propagator via Matsubara frequencies and obtained results for the general and dual condensate similar to ours [97].

In the Nambu-Jona-Lasinio model and its Polyakov loop extended version, Mukherjee et al. and Kashima et al. used the dressed Polyakov loop to investigate the chiral and deconfinement transition [99] [98]. Similarly, Gatto and Ruggieri studied the effects of a magnetic field [100].

On the lattice, Danzer et al. used the dual condensate to investigate the phase transitions of the G_2 gauge theory [101] (which is interesting with respect to the vortex picture since it has no nontrivial center) and Bilgici et al. used the dual chiral condensate of $SU(2)$ adjoint quarks [102] (where chiral restoration and deconfinement occur at very different temperatures).

A related idea to dressed Wilson loops has recently been suggested in [103].

5.2 More fermionic observables

The chiral condensate $\langle \bar{\psi}\psi \rangle$ is an order parameter for chiral symmetry breaking, we will analyze and numerically measure more condensates $\langle \bar{\psi}\Gamma\psi \rangle$ with Γ being a matrix in the Clifford algebra to find other aspects of QCD phase transition.

5.2.1 General fermionic observables

Let us consider fermion operator condensates in the framework of the Path Integral.

$$\langle \bar{\psi}\Gamma\psi \rangle = \frac{\int d\bar{\psi}d\psi dA \bar{\psi}\Gamma\psi e^{-S}}{\int d\bar{\psi}d\psi dA e^{-S}} \quad (5.12)$$

Then one can find the expression for the numerator of eqn. (5.12) in terms of eigenvalues and eigenvectors of D .

$$\begin{aligned} \int d\bar{\psi}d\psi \bar{\psi}\Gamma\psi e^{-S} &= \int d\bar{\psi} \frac{d\Gamma\psi}{D[\Gamma]} \bar{\psi}\Gamma\psi e^{-[\bar{\psi}(D+m)\psi+\dots]} \\ &= \int d\bar{\psi} \frac{d\psi'}{D[\Gamma]} \bar{\psi}\psi' e^{-[\bar{\psi}(D+m)\Gamma^{-1}\psi'+\dots]} \\ &= \int d\bar{\psi}d\psi'' \bar{\psi}D[\Gamma]\psi'' e^{-[\bar{\psi}(D+m)\Gamma^{-1}D[\Gamma]\psi''+\dots]} \\ &= \langle \text{Tr}[(D+m)\Gamma^{-1}] \rangle = \langle \text{Tr}[\Gamma(D+m)^{-1}] \rangle, \end{aligned} \quad (5.13)$$

where $\psi' = \Gamma\psi$, $\psi'' = \frac{\psi'}{D[\Gamma]}$ ($D[\Gamma]$ is the determinant of Γ), the spectral representation follows immediately as

$$\langle \bar{\psi}\Gamma\psi \rangle = \left\langle \sum_{\lambda_i} \frac{\langle \nu_i | \Gamma | \nu_i \rangle}{i\lambda_i + m} \right\rangle \quad (5.14)$$

where $i\lambda_i$ are eigenvalues of D , ν_i are corresponding eigenmodes of D and $\Gamma_{i,j} = \langle \nu_i | \Gamma | \nu_j \rangle$. We can further simplify the results of eqn. (5.14) by using the relation between $|\nu_i\rangle$ and $|\nu_{-i}\rangle = \gamma_5 |\nu_i\rangle$ (which is the eigenmode with eigenvalue $-i\lambda_i$)

$$\langle \nu_{-i} | \Gamma | \nu_{-i} \rangle = \langle \nu_i | \gamma_5 \Gamma \gamma_5 | \nu_i \rangle = \pm \langle \nu_i | \Gamma | \nu_i \rangle \quad (5.15)$$

where the minus sign applies for Γ 's that anti-commute with γ_5 and plus sign for Γ 's that commute with γ_5 , we will use this equation in section 5.4.4.

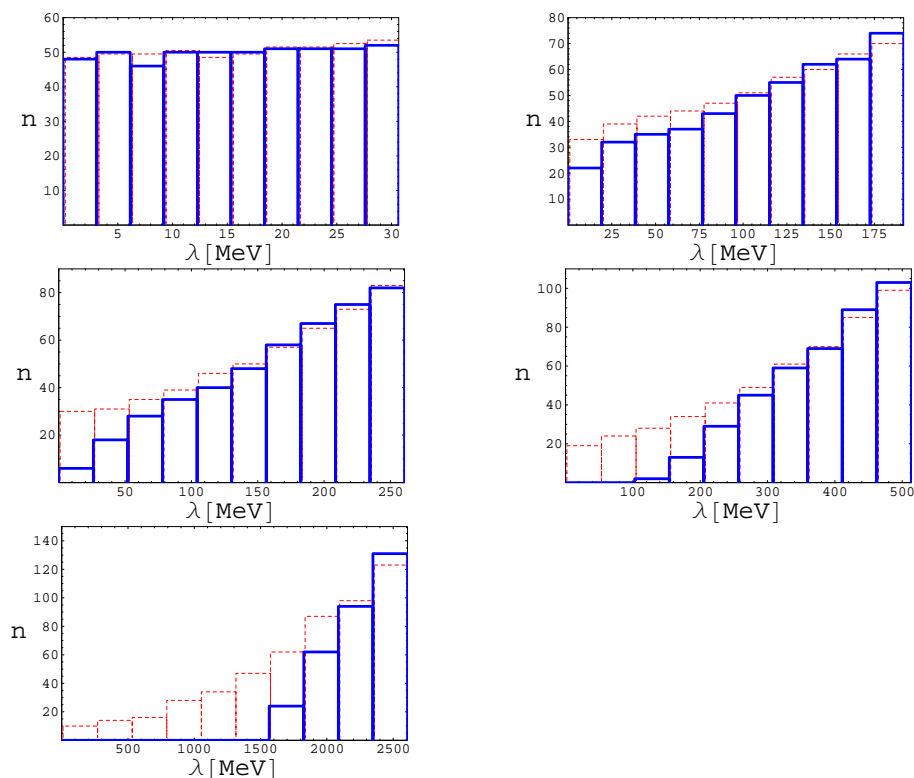


Figure 5.3: The spectral density of D , red dashed columns show $\rho(\lambda)$ at physical boundary conditions, blue solid ones show that at periodic boundary conditions. The temperature of these plots are: 78MeV (upper left), 152MeV (upper right), 172MeV (mid left), 250MeV (mid right) and 892MeV (last) respectively.

Eqn. (5.14) shows that we need both the spectra and the expectation values of $\langle \nu_i | \Gamma | \nu_i \rangle$ to calculate the generalized fermionic condensates, the chiral condensate is an exception because its $\Gamma = \mathbf{1}$ always gives $\langle \nu_i | \mathbf{1} | \nu_i \rangle = 1$.

5.2.2 Susceptibilities

We know that the quark condensate $\langle \bar{\psi} \psi \rangle = \frac{\partial}{\partial m} \ln Z$ is the first derivative of the logarithm of the partition function $\ln Z$ with respect to the mass. The second derivative of $\ln Z$ is the conventional quark susceptibility. This generates three terms [91]:

$$\begin{aligned} \chi_{\bar{\psi}\psi} &= \frac{\partial^2}{\partial m^2} \ln Z = \frac{1}{V_4} \left(\frac{\partial_m^2 Z}{Z} - \left(\frac{\partial_m Z}{Z} \right)^2 \right) \\ &= \frac{1}{V_4} \langle \left(\text{Tr} \frac{1}{D+m} \right)^2 \rangle - \frac{1}{V_4} \langle \text{Tr} \frac{1}{(D+m)^2} \rangle - \frac{1}{V_4} \langle \text{Tr} \frac{1}{D+m} \rangle^2. \end{aligned} \quad (5.16)$$

The sum of the first term and the last term is the squared standard deviation of the quark condensate $\langle \text{Tr} \frac{1}{D+m} \rangle$, in the chiral limit, it reflects the fluctuation

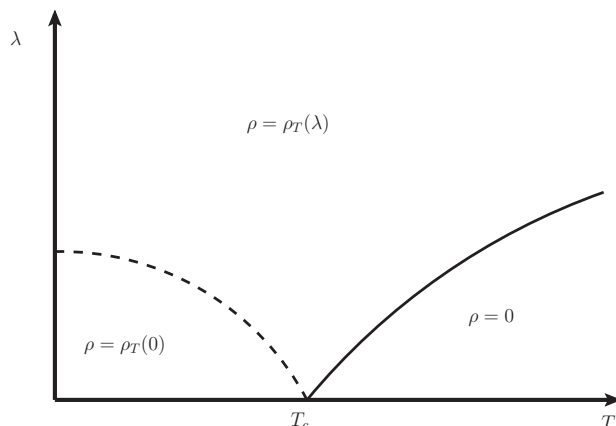


Figure 5.4: Schematic spectrum density $\rho(\lambda, T)$ with anti-periodic boundary condition, the measured spectrum density results are shown in Fig. 5.3.

of chiral condensate, and is also called disconnected chiral susceptibility. The second term is called the connected chiral susceptibility and corresponds to the integrated scalar meson correlation function [91].

The chiral symmetry breaking/restoration signal in the chiral susceptibility is a peak near T_c . In the disconnected part, it is easy to understand as it is proportional to the squared standard deviation of the quark condensate. The connected part can be understood with the Banks-Casher relation [57], that the quark condensate.

$$\langle \bar{\psi}\psi \rangle = \frac{1}{V_4} \langle \text{Tr} \frac{1}{D+m} \rangle = \frac{1}{V_4} \int \frac{2m\rho(\lambda)d\lambda}{\lambda^2+m^2} \xrightarrow{m \rightarrow 0} \frac{\pi}{V_4} \rho(0). \quad (5.17)$$

It gets $\rho(0)$ in the chiral limit because $\frac{2m}{\lambda^2+m^2} \xrightarrow{m \rightarrow 0} \pi\delta(\lambda)$. But for a finite mass, $2m/(\lambda^2+m^2)$ is a narrow peak (width equals m). So the integration of a function $f(\lambda)$ with weight factor $2m/(\lambda^2+m^2)$ is a kind of average of $f(\lambda)$ within the width of the peak. The chiral condensate as the order parameter of chiral symmetry breaking is non-vanishing in the low temperature chirally symmetric phase, but vanishes in the high temperature chiral symmetry breaking phase. $\rho(0)$ behaves accordingly as shown schematically in Fig. 5.4. The spectrum density results of smeared $N_f = 2 + 1$ configurations from the Wuppertal-Budapest collaborations [8] are shown in Fig. 5.3.

As the quark condensate with finite quark mass is actually an average of $\rho(\lambda)$ from $\lambda = 0$ to $\lambda = m$ with weight function $2m/(\lambda^2+m^2)$, the derivative of this average should be small in the chiral symmetric phase because the lowest part of the spectrum density in this phase is flat so the average changes slowly with m . This average is also small in the chiral symmetry breaking phase because the lowest part of the spectrum has a gap. The only peak comes from the phase transition region $T \approx T_c$ where the lowest part of the spectrum is neither a gap nor flat.

Our quark susceptibility result in Fig. 5.5 reproduces the chiral susceptibility results of [8], One can find that the disconnected contributions and the connected contributions are approximately of the same magnitude, which is dif-

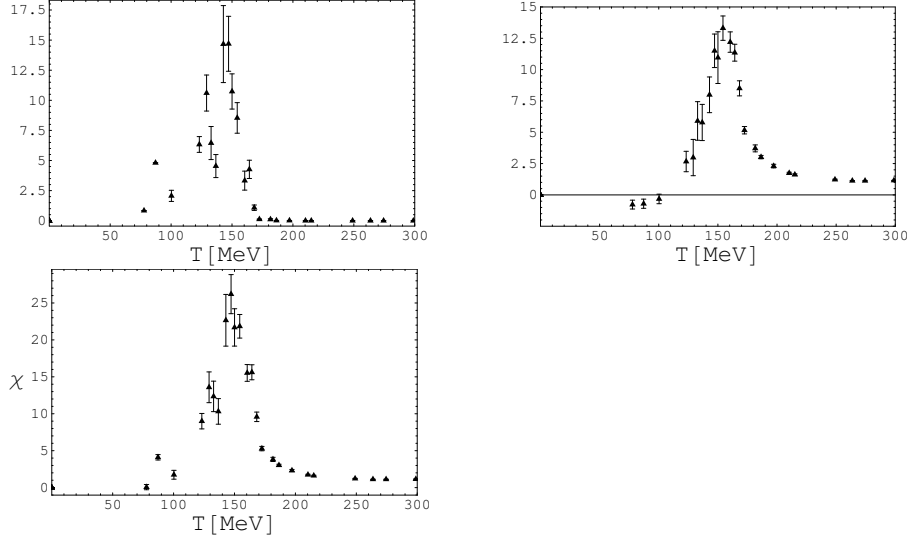


Figure 5.5: (Unrenormalized) conventional chiral susceptibility results measured with the spectral method at low mass ($m = 1\text{MeV}$). The plots are, from upper left clockwise: disconnected chiral susceptibility, connected chiral susceptibility and full chiral susceptibility.

ferent from the conclusion by the hotQCD collaboration [91].

One can define general susceptibilities like the quark number susceptibility similarly:

$$\begin{aligned}
\frac{1}{V_4} \partial_\mu^2 \ln Z &= \frac{1}{V_4} \partial_\mu \left(\frac{\partial_\mu Z}{Z} \right) = \frac{1}{V_4} \left(\frac{\partial_\mu^2 Z}{Z} - \left(\frac{\partial_\mu Z}{Z} \right)^2 \right) \\
&= \frac{1}{V_4} \left(\langle [\text{Tr} \frac{\gamma_0}{D+m+\mu\gamma_0}]^2 \rangle - \langle \text{Tr} [\gamma_0 \frac{1}{D+m+\mu\gamma_0} \gamma_0 \frac{1}{D+m+\mu\gamma_0}] \rangle \right. \\
&\quad \left. - \langle \text{Tr} \frac{\gamma_0}{D+m+\mu\gamma_0} \rangle^2 \right), \tag{5.18}
\end{aligned}$$

and the $\mu \rightarrow 0$ limit is

$$\begin{aligned}
&\frac{1}{V_4} \partial_\mu^2 \ln Z \Big|_{\mu \rightarrow 0} \\
&= \frac{1}{V_4} \left(\langle [\text{Tr} \frac{\gamma_0}{D+m}]^2 \rangle - \langle \text{Tr} [\gamma_0 \frac{1}{D+m} \gamma_0 \frac{1}{D+m}] \rangle - \langle \text{Tr} [\frac{\gamma_0}{D+m}] \rangle^2 \right). \tag{5.19}
\end{aligned}$$

For a general matrix Γ , the middle term will read in the spectral representation as

$$\text{Tr} \left[\Gamma \frac{1}{D+m} \Gamma \frac{1}{D+m} \right] = \sum_i \sum_j \frac{1}{(i\lambda_i + m)(i\lambda_j + m)} \Gamma_{ij} \Gamma_{ji}, \tag{5.20}$$

where $\Gamma_{ij} = \langle \nu_i | \Gamma | \nu_j \rangle$.

This is the simplest form of this term, we can not further simplify by apply formulas like $\sum_\alpha |\alpha\rangle \langle \alpha| = 1$. So we can not calculate a general susceptibility by

having measured Γ_{ii} only, except the $\Gamma = 1$ case of quark susceptibility which has $\Gamma_{ij} = \delta_{ij}$. But one can find that the rest two terms in the general susceptibility that can be determined from our data are proportional to the squared standard deviation of the corresponding condensate just like the disconnected quark susceptibility.

5.3 Dual quark density

The condensate with $\Gamma = \gamma_0$ is the quark density $n = \langle \bar{\psi}\gamma_0\psi \rangle$, it is of particular interest as it couples to the chemical potential. Similar to the general quark condensate, we can define the general quark density $n(\phi) = \langle \bar{\psi}\gamma_0\psi \rangle_\phi$ and its dual \tilde{n}_k . Different from the general quark condensate, which is renormalized by the bare masses as shown in eqn. (5.9), the general quark density $\partial_\mu \ln Z$ does not need renormalization [9].

5.3.1 The Stefan-Boltzmann limit of dual quark density

Let us discuss its high temperature limit first. We know that in the high temperature limit, the QCD is asymptotically free, gluons and quarks decouple, which means we can simulate the high temperature limit of QCD with a free gas of gluons and quarks. Then the theoretical high temperature limit for $n(\phi)$ and \tilde{n}_k can be estimated in statistical mechanics.

In the free gas of gluons and quarks, the fermion part of the partition function is

$$Z = \prod_i (1 + e^{-(E_i - \mu)/T})^{N(E_i)} \quad (5.21)$$

where our boundary condition $\psi(\beta + x_0) = e^{i\phi}\psi(x_0)$ equals an imaginary chemical potential $\mu_I = i(\phi - \pi)T$ which only is felt by the valence quarks (vanishing chemical potential $\mu = 0$ corresponds to $\phi = \pi$), E_i runs over all energy eigenstates and $N(E_i)$ are the degeneracies.

The general quark density of the free quark gas system is

$$n(\mu, T) = \frac{1}{V_4} T \left(\frac{\partial \ln Z}{\partial \mu} \right)_{V, T} = \frac{1}{V_4} \sum_i \frac{N(E_i)}{1 + e^{(E_i - \mu)/T}} \quad (5.22)$$

and the continuous version of $n(\mu, T)$ is

$$n(\phi, T) = \frac{1}{V_4} \int_0^\infty dE \left(\frac{D_q(E)}{1 + e^{(E - \mu)/T}} - \frac{D_{\bar{q}}(E)}{1 + e^{(E + \mu)/T}} \right) \quad (5.23)$$

where $D_q(E)$ is the density of quark eigenstates and $D_{\bar{q}}(E)$ is that of the anti-quarks.

Putting the imaginary chemical potential $\mu_I = i(\phi - \pi)T$ in and doing the Fourier transformation, we get the dual quark density

$$\tilde{n}_1(T) = \int_0^{2\pi} \frac{e^{-i\phi} d\phi}{2\pi} \int_0^\infty dE \left(\frac{D_q(E)}{1 - e^{E/T} e^{-i\phi}} - \frac{D_{\bar{q}}(E)}{1 - e^{E/T} e^{i\phi}} \right), \quad (5.24)$$

The eigenstate density of the free quark gas is clearly

$$D_q(E) = D_{\bar{q}}(E) = \frac{4\pi p^2}{(2\pi)^3} \frac{d|\vec{p}|}{dE}. \quad (5.25)$$

In the chiral limit where $E = |\vec{p}|$ (could also be done for $E = \sqrt{p^2 + m^2}$ up to some numerical integrations), we do the tricks of changing the integral variable to $z = e^{-i\phi}$ and the order of integration, apply the residue theorem and get

$$\tilde{n}_1(T) = -\frac{T^3}{\pi^2} \quad (5.26)$$

This result is the dual quark density of a single fermion freedom. Including the flavor number N_f , 3 colors and two spin directions, the dual quark density is

$$\tilde{n}_1(T) = -\frac{6N_f T^3}{\pi^2}. \quad (5.27)$$

This results can be easily generalized to dual quark densities of higher winding numbers:

$$\tilde{n}_k(T) = -\frac{6N_f T^3}{\pi^2 k^3}. \quad (5.28)$$

A sum of them can be connected to the connected part of quark number susceptibility $\chi_2 = \frac{1}{V_4} \frac{\partial^2}{\partial \mu^2} \ln Z|_{\mu \rightarrow 0}$ in [9, 8], given by eqn. (5.19) (note that the disconnected part of quark number susceptibility contributes only near T_c , does not contribute to the high temperature limit value of quark number susceptibility), which is a conventional operator, not a dual operator. At high temperature, we recover its Stefan-Boltzmann limit by dual quark densities,

$$\chi_2 = \sum_k k(-1)^k \frac{-\tilde{n}_k}{T} = N_f T^2 \quad (5.29)$$

We see that the dual quark density has a nice high temperature limit, but what is the physical meaning of dual quark density? We will discuss the leading contribution to the dual quark density below.

Keeping the high temperature limit, and replace the Dirac-Fermi statistics in eqn. (5.23) by Maxwell-Boltzmann statistics, one gets

$$\begin{aligned} n(\phi) &\approx \sum_{\alpha} D_q(\alpha) e^{-(E(\alpha)-\mu)/T} - \sum_{\gamma} D_{\bar{q}}(\gamma) e^{-(E(\gamma)+\mu)/T} \\ &\approx e^{\mu/T} n_q(\mu=0) - e^{-\mu/T} n_{\bar{q}}(\mu=0) \end{aligned} \quad (5.30)$$

where

$$n_q(\mu=0) = n_{\bar{q}}(\mu=0) = \sum_{\alpha} D_q(\alpha) e^{E(\alpha)/T} \quad (5.31)$$

are the densities of quarks and anti-quarks with $\mu=0$ in this statistics, $n_q(\mu=0)$ and $n_{\bar{q}}(\mu=0)$ are the same because $\mu=0$ means no favor on quarks or anti-quarks. We can simplify eqn. (5.30):

$$n(\phi) \approx -2i \sin \phi n_q(0). \quad (5.32)$$

Then it is clear that the leading contribution to the dual quark density (in the high temperature limit) is $n_q(\mu=0) = n_{\bar{q}}(\mu=0)$, the density of quarks (or anti-quarks) without chemical potential.

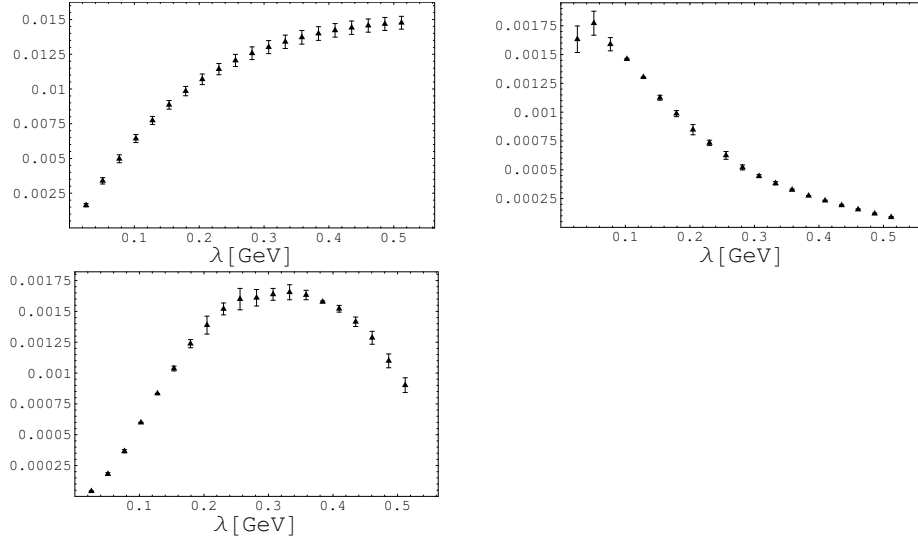


Figure 5.6: The left and right panels in the first row are the accumulated and individual contributions to \tilde{n}_1 [GeV³] at $T = 182\text{MeV}$ and $m = 1\text{MeV}$, respectively, the lower panel is $2i\lambda\tilde{D}_1(\lambda)$. Results in this figure use the lowest 1500 eigenmodes (the 500th eigenmode is around 0.33GeV).

5.3.2 Convergence problems of dual quark density

In the last subsection, we have found that the leading contribution to the dual quark density is the density of quarks n_q or the density of anti-quarks $n_{\bar{q}}$ without chemical potential. This operator is obviously not IR dominated. Our numerical results indeed show that the dual quark density \tilde{n} converges slowly compared to the dual condensate.

Let us start from the general quark density with $\Gamma = \gamma_0$, which is (see details in section 5.4.3)

$$n(\phi) = \sum_{\lambda_{\phi j}} \frac{\langle \nu_{\phi j} | \gamma_0 | \nu_{\phi j} \rangle}{i\lambda_{\phi j} + m} = -i \sum_{\lambda_{\phi j} > 0} \frac{2\lambda_{\phi j} \langle \nu_{\phi j} | \gamma_0 | \nu_{\phi j} \rangle}{\lambda_{\phi j}^2 + m^2}. \quad (5.33)$$

We can write it in the continuous form:

$$n(\phi) = -i \int_0^\infty \frac{2\lambda P_\phi(\lambda) \rho_\phi(\lambda)}{\lambda^2 + m^2} d\lambda \quad (5.34)$$

where $P_\phi(\lambda) = \langle \nu_{\lambda_\phi} | \gamma_0 | \nu_{\lambda_\phi} \rangle$ is the γ_0 expectation value of fermion eigenmodes and $\rho_\phi(\lambda)$ is the density of eigenmodes, both are ϕ dependent. The additional factor of λ in the numerator hints on a worse IR dominance compared to the dual condensates.

We can Fourier transform $n(\phi)$ and get the formula for the dual quark density

$$\tilde{n}_1 = \int_0^\infty \frac{-2i\lambda\tilde{D}_1(\lambda)}{\lambda^2 + m^2} d\lambda \quad (5.35)$$

where

$$\tilde{D}_1(\lambda) = \int P_\phi(\lambda) \rho_\phi(\lambda) \frac{e^{-i\phi} d\phi}{2\pi} \quad (5.36)$$

is the first Fourier component of $P_\phi(\lambda)\rho_\phi(\lambda)$. \tilde{n}_1 is basically real because $n(\phi)$ is odd around the $\phi = \pi$, as we will see in section 5.5.

The accumulated and individual contributions to \tilde{n}_1 in Fig. 5.6 show that the sum of the lowest 500 or even 1500 eigenmode contributions is not the really well converged dual quark density. However, looking at just the term $2i\lambda\tilde{D}_1(\lambda)$ suggests a method to estimate the upper limit of the higher mode contributions beyond the 500 lowest modes.

Suppose that $f(\lambda) = 2i\lambda\tilde{D}_1(\lambda)$ is less or equal to $f(K)$ if $\lambda > K$ as Fig. 5.6 shows such a trend to decrease with λ when it is large enough. Then we can estimate the upper bounds of the higher spectrum contributions because

$$\int_K^\infty \frac{f(\lambda)d\lambda}{\lambda^2 + m^2} < \frac{f(K)}{m} \arctan\left(\frac{m}{K}\right). \quad (5.37)$$

If $K \gg m$, we can simplify this upper limit to $f(K)/K$. This is a very conservative estimation of the upper bounds of the higher spectrum contributions.

5.4 Technical details of staggered fermions

In this section, we collect some technicalities of staggered fermions, especially those needed for the computation of $\langle \bar{\psi}\Gamma\psi \rangle$ observables in section 5.2.

5.4.1 The staggered fermion action

The staggered fermion is a type of fermion in lattice QCD that reduces the number of redundant fermion resonances from 16 to 4.

The fermion part of QCD Euclidean space-time Lagrangian is

$$L_\phi(x) = -\bar{\psi}(\gamma_E^\mu D_\mu + m)\psi, \quad (5.38)$$

where $\gamma_E^4 = \gamma^0$ and $\gamma_E^i = i\gamma^i$ (for simplicity, we write γ^μ instead of γ_E^μ below), and $\bar{\psi} = \psi^\dagger$ for Lorentz invariance in Euclidean space-time. The naive lattice Lagrangian is [83]

$$\begin{aligned} L_{naive} &= \frac{1}{2a} \sum_\mu [\bar{\psi}(x)\gamma^\mu U_\mu(x)\psi(x + \hat{\mu}) - \bar{\psi}(x)\gamma^\mu U_\mu(x - \hat{\mu})\psi(x - \hat{\mu})] \\ &+ m \sum_x \bar{\psi}(x)\psi(x). \end{aligned} \quad (5.39)$$

This naive lattice Lagrangian has a big difference from the continuum Lagrangian—the doubling problem.

To show the doubling problem, let us begin with the propagator of a free fermion.

$$\frac{1}{a}S(p) = (i\gamma^\mu \sin p_\mu a + m)^{-1} = \frac{-i\gamma^\mu \sin p_\mu a + m}{\sum_\mu \sin^2 p_\mu a + m^2 a^2}. \quad (5.40)$$

Like atoms in crystals, the momentum space of lattice fermions also have a Brillouin zone from $-\pi/a$ to π/a . The continuum fermion propagator $(i\gamma^\mu p_\mu + m)^{-1}$ has large contributions from the small $|p|$ region around $p_\mu = (0, 0, 0, 0)$, but the naive lattice fermion propagator in eqn. (5.40) has 15 more similar

regions around p_μ from $(0, 0, 0, \pi)$ to (π, π, π, π) . The result is that a fermion resonance in continuum has 16 ‘‘copies’’ of fermions on lattice if we adopt the naive fermion Lagrangian.

One way to avoid the fermion doubling problem is to add some terms in the Lagrangian to shift redundant ‘‘copies’’, like that done in Wilson fermions. It adds a second derivative term to the Lagrangian [83]

$$S^W = r\bar{\psi}D_W\psi = -\frac{r}{2a}\sum_{x,\mu}\psi_x(\psi_{x+\hat{\mu}} - 2\psi_x + \psi_{x-\hat{\mu}}) \sim -\frac{r}{2a}\bar{\psi}D^2\psi \quad (5.41)$$

but the price is the chiral symmetry, it is explicitly broken by the Wilson term.

The staggered fermion [88, 89] gives a method that can reduce the number of fermion copies to 4 and keep the chiral symmetry. It starts with the naive lattice fermion Lagrangian in eqn. (5.39), applies the redefinition of fermion fields by $\psi_x \rightarrow \Omega_x\chi_x$ and $\bar{\psi}_x \rightarrow \bar{\chi}_x\Omega_x^\dagger$ where

$$\Omega_x = (\gamma_1)^{x_1}(\gamma_2)^{x_2}(\gamma_3)^{x_3}(\gamma_4)^{x_4} \quad \text{and} \quad \Omega_x^\dagger = (\gamma_4)^{x_4}(\gamma_3)^{x_3}(\gamma_2)^{x_2}(\gamma_1)^{x_1}. \quad (5.42)$$

Using the anti-commutation relation of γ matrices

$$\{\gamma_E^\mu, \gamma_E^\nu\} = 2g_E^{\mu\nu}\mathbf{1} = 2\delta^{\mu\nu}\mathbf{1}, \quad (5.43)$$

we can simplify the fermion field redefined Lagrangian to

$$\sum_{x,\mu}\frac{1}{2a}\eta_\mu(x)\bar{\chi}(x)\mathbf{1}(U_\mu(x)\chi(x+\hat{\mu}) - U_\mu^\dagger(x-\hat{\mu})\chi(x-\hat{\mu})) + m\bar{\chi}(x)\mathbf{1}\chi(x). \quad (5.44)$$

where

$$\eta_\mu = (-1)^{x_1+x_2+\dots+x_{\mu-1}}. \quad (5.45)$$

The Dirac space structure of this Lagrangian is trivial. Restricting to one of the Dirac components, we get the staggered fermion Lagrangian

$$L = \sum_{x,\mu}\frac{1}{2a}\eta_\mu(x)\bar{\chi}(x)(U_\mu(x)\chi(x+\hat{\mu}) - U_\mu^\dagger(x-\hat{\mu})\chi(x-\hat{\mu})) + m\bar{\chi}(x)\chi(x) \quad (5.46)$$

η_μ shows a mixture of Dirac index and spatial index, its sign alternates with a period of 2 in all directions. This period suggests that 2^4 -hypercubes are basic units for staggered fermions. We will come to this later.

The remaining redundancies are called ‘tastes’, one can confirm this 4 degeneracy from the staggered fermion spectrum of smooth lattice configurations.

5.4.2 Properties of the staggered fermion Dirac operator

The massless Dirac operator D of a staggered fermion is

$$D_{x,y} = \frac{1}{2a}\sum_{\mu}\eta_\mu(x)[U_\mu(x)\delta_{x+\hat{\mu},y} - U_\mu^\dagger(x-\hat{\mu})\delta_{x-\hat{\mu},y}]. \quad (5.47)$$

We can define a site of the lattice even or odd by

$$\eta_5 = (-1)^{x_1+x_2+x_3+x_4}, \quad (5.48)$$

$\eta_5 = 1$ sites are even sites and $\eta_5 = -1$ sites are odd sites. Every even site is surrounded by 16 odd sites and every odd site is surrounded by 16 even sites. The hopping terms of $D_{x,y}$ in eqn. (5.47) are always between adjacent sites, means $D_{x,y}$ is between odd sites and even sites. By moving all odd sites to the upper half and all even sites to the lower half, the Dirac operator $D_{x,y}$ is of the form:

$$D = \begin{pmatrix} 0 & R \\ -R^\dagger & 0 \end{pmatrix} \quad (5.49)$$

where R is the part of $D_{x,y}$ that includes all the links from even sites to odd sites and $-R^\dagger$ includes all the links from odd sites to even sites. Thus the matrix D^2 is block-diagonal, negative definite and Hermitian:

$$D^2 = \begin{pmatrix} -RR^\dagger & 0 \\ 0 & -R^\dagger R \end{pmatrix}. \quad (5.50)$$

By projecting this D^2 to the sub-lattice of odd sites (or the sub lattice of even sites), the staggered fermion field becomes $\nu' = \frac{(1-\eta_5)}{2}\nu$, D^2 becomes $D_o^2 = D^2 \frac{1-\eta_5}{2}$ and clearly we can reduce the size of the matrix by half [84]. In numerical eigenvalue problems, reducing the dimension of the matrix is of course very helpful.

The massless Dirac operator is anti-Hermitian, we can understand it from both the continuous and the lattice form of D . The continuous D is $D = \gamma^\mu(\partial_\mu + iA_\mu)$, in which the γ_μ in Euclidean definition is Hermitian, and $D_\mu = \partial_\mu + iA_\mu$ is anti-Hermitian, so D is anti-Hermitian. The staggered fermion massless Dirac operator D in eqn. (5.47) between x and $x + \hat{\mu}$ is $D_{x,x+\hat{\mu}} = \frac{1}{2a}\eta_\mu(x)U_\mu(x)$ and $D_{x+\hat{\mu},x} = -\frac{1}{2a}\eta_\mu(x+\hat{\mu})U_\mu^\dagger(x)$, consider $\eta_\mu(x) = \eta_\mu(x + \hat{\mu})$, we get $D_{x,x+\hat{\mu}} = -D_{x+\hat{\mu},x}^\dagger$. Thus D (or $D_{x,y}$) as an anti-Hermitian operator should have a purely imaginary spectrum.

We can get more information from the fact that the massless Dirac operator D anti-commutes with γ_5 and D^2 commute with γ_5

$$\{D, \gamma_5\} = 0, \quad [D^2, \gamma_5] = 0, \quad (5.51)$$

the corresponding staggered relation is

$$\{D, \eta_5\} = 0, \quad [D^2, \eta_5] = 0. \quad (5.52)$$

The (anti-)commutation relations above tells us:

1. We can choose eigenmodes of D^2 to reside on the even sites only or on the odd sites only to reduce the dimension of the matrix. A set of operators commuting with each other makes these operators can have common eigenvectors. The eigenvectors of $\eta_5(x)$ reside on the odd sites only or on the even sites only, and D^2 commutes with η_5 , so we can choose the eigenmodes of D^2 on the odd sub-lattice or on the even sub-lattice (by linearly recombinations of the degenerated eigenmodes of D^2 on the full lattice), we have got this from the block-diagonal structure of D^2 .

2. Eigenvectors of D come in pairs, a pair of eigenvectors has opposite eigenvalues. If ν is an eigenvector of D : $D\nu = \lambda\nu$, then $\eta_5\nu$ is the paired eigenvector of D : $D(\eta_5\nu) = -\eta_5 D\nu = -\lambda(\eta_5\nu)$.

3. Eigenvectors of D^2 are linear combinations of paired eigenvectors, which means if we choose the eigenvectors of D^2 on the odd (even) sub-lattice, these

eigenvectors are not eigenvectors of D in general. On the other hand, an eigenvector of D is always an eigenvector of D^2 , and we know that eigenvectors of D appear in pairs which have opposite and imaginary eigenvalues, then ν and $\eta_5\nu$ are non-degenerate modes of D but degenerate modes of D^2 . Consider D not commuting with η_5 , eigenvectors of D^2 can only be the recombination of ν and $\eta_5\nu$: $\frac{1+\eta_5}{2}\nu$ and $\frac{1-\eta_5}{2}\nu$, their eigenvalues are negative and real.

We can recover the eigenvectors of D if we have both the spectrum and eigenmodes of $D_o^2 = D^2 \frac{1-\eta_5}{2}$ (or $D_e^2 = D^2 \frac{1+\eta_5}{2}$). An eigenvector $A = \frac{1-\eta_5}{2}\nu$ of D_o^2 , should satisfy

$$D\nu = \begin{pmatrix} 0 & R \\ -R^\dagger & 0 \end{pmatrix} \begin{pmatrix} A \\ B \end{pmatrix} = \begin{pmatrix} RB \\ -R^\dagger A \end{pmatrix} = \begin{pmatrix} \lambda A \\ \lambda B \end{pmatrix} = \lambda\nu \quad (5.53)$$

where $B = \frac{1+\eta_5}{2}\nu$ is the even site part of ν . So we get

$$\lambda B = -R^\dagger A \Rightarrow B = \frac{-R^\dagger}{\lambda} A = \frac{D}{\lambda} A \quad (5.54)$$

Let us summarize the method to calculate the eigenmodes and the eigenvectors of D :

1. Calculate the eigenmodes and the spectrum of D_o^2 .
2. An eigenmode ν_o of D_o^2 with eigenvalue $-\lambda^2$ corresponds to two eigenmodes of D :

$$\nu_1 = \begin{pmatrix} \nu_o \\ \frac{D}{i\lambda}\nu_o \end{pmatrix} \quad \text{and} \quad \nu_2 = \begin{pmatrix} \nu_o \\ \frac{D}{-i\lambda}\nu_o \end{pmatrix}, \quad (5.55)$$

their eigenvalues are $\lambda_1 = i\lambda$ and $\lambda_2 = -i\lambda$, respectively.

5.4.3 Staggered fermion operators

As worked out in section 5.2, one needs the expectation values $\langle \nu_i | \Gamma | \nu_i \rangle$ for the condensates $\langle \bar{\psi} \Gamma \psi \rangle$. The definition of $\langle \nu_i | \Gamma | \nu_i \rangle$ is clear in the continuum and for the naive lattice fermion, but is not straightforward for staggered fermions because the spinor index is mixed with the space index. In other words, the operator acting in staggered taste space needs to be determined. In this section we will discuss the definition of $\langle \nu_i | \Gamma | \nu_i \rangle$ for staggered fermions.

The first possibility that comes to one's mind is to apply the staggered field redefinition in eqn. (5.42) to $\langle \bar{\psi} \Gamma \psi \rangle$ just like we did to the naive lattice fermion Lagrangian in eqn. (5.39).

Let us try $\Gamma = \gamma_\mu$, the naive matrix element $\langle \bar{\psi} \gamma_\mu \psi \rangle$ after the redefinition is

$$\sum_x \bar{\psi}(x) \gamma_\mu \psi(x) \Rightarrow \sum_x \eta_5(x) (-1)^{x_\mu} \bar{\chi}(x) \gamma_\mu \chi(x). \quad (5.56)$$

We find that $\langle \bar{\psi} \gamma_\mu \psi \rangle$ after the redefinition has a non-trivial structure in the spinor space, so we can not reduce the Dirac fermion operator to a staggered fermion operator this way.

An alternative is to define from staggered fermions on a 2^4 hypercube, four "tastes" of Dirac fermions (4 component in Dirac space) which transform like fields on the base site of the hypercube [85, 89, 90]:

$$q_{\alpha,a}^c(y) = \sum_\rho (U_y)^{c,c'}(\rho) (\Gamma_\rho)_{\alpha,a} \chi_y^{c'}(\rho) \quad (5.57)$$

where α is the Dirac index, a is the taste index, and c is the color index. $2y$ is the hypercube base site, while ρ ($\rho_\mu \in \{0, 1\}$) is the relative coordinate of a site ($2y + \rho$) in the hypercube to the hypercube base site. The staggered fermion field $\chi_y(\rho) = \chi(2y + \rho)$ and U_ρ is the link from $2y + \rho$ to the base site of the hypercube. There are two different possibilities to define U_ρ , the first one is a product of links along a definite path from ρ to $\{0, 0, 0, 0\}$ like

$$U_y(\rho) = [U_1(2y)]^{\rho_1} [U_2(2y + \rho_1)]^{\rho_2} [U_3(2y + \rho_1 + \rho_2)]^{\rho_3} [U_4(2y + \rho_1 + \rho_2 + \rho_3)]^{\rho_4}, \quad (5.58)$$

the second one is the permutation definition which is an average over different paths from ρ to $\{0, 0, 0, 0\}$:

$$U_y(\rho) = \frac{1}{N_{[C]}} \sum_{[C]} U_C(2y + \rho \rightarrow 2y). \quad (5.59)$$

We will discuss the difference of these two definitions in detail in the end of this subsection.

Similarly, Γ_ρ is the product of γ matrices along the path from ρ to $\{0, 0, 0, 0\}$:

$$\Gamma_\rho = [\gamma_1]^{\rho_1} [\gamma_2]^{\rho_2} [\gamma_3]^{\rho_3} [\gamma_4]^{\rho_4}. \quad (5.60)$$

One can define ‘‘Dirac fermions’’ this way because the staggered fermion Lagrangian equals the naive ‘recovered’ Dirac fermion Lagrangian in the continuum limit [86, 87].

$$\begin{aligned} S_F + S_m &= (2a)^d \sum_{y, \mu} \{ \bar{q}(y) (\gamma_\mu \otimes \mathbf{1}) \Delta_\mu q(y) + a \bar{q}(y) (\gamma_5^\dagger \otimes t_\mu^\dagger t_\mu^\dagger) \delta_\mu q(y) \} \\ &\quad + (2a)^d m \sum_y \bar{q}(y) (\mathbf{1} \otimes \mathbf{1}) q(y). \end{aligned} \quad (5.61)$$

where both

$$\Delta_\mu f(y) = \frac{1}{4a} [f(y + \hat{\mu}) - f(y - \hat{\mu})] \quad (5.62)$$

and

$$\delta_\mu f(y) = \frac{1}{4a^2} [f(y + \hat{\mu}) - 2f(y) + f(y - \hat{\mu})] \quad (5.63)$$

have a finite continuum limit, which means the second term of eqn. (5.61) disappears in the continuum limit.

The ‘‘recovered’’ Dirac fermions have a degeneracy of 4, for the tastes. Each of these 4 tastes of fermions has 4 components in Dirac space. An operator composed of ‘‘recovered’’ Dirac fermions includes a structure in taste space and a structure in spinor space

$$\langle q | O_{ST} | q \rangle \equiv (\bar{q})_{a\alpha} (\gamma_S)_{\alpha\beta} q_{\beta b} (\gamma_T)_{ba} = \text{Tr}(\bar{q} \gamma_S q \gamma_T) = \bar{q} (\gamma_S \otimes \gamma_T) q. \quad (5.64)$$

From the ‘‘recovered’’ Dirac fermions of eqn. (5.57), O_{ST} is a bilinear in staggered fermion on each hypercube. For a conventional operator $\langle \bar{\psi} \Gamma \psi \rangle$ in the continuum, the corresponding staggered fermion operator O_{ST} should give $\gamma_S = \Gamma$, but what is the taste space structure? Let us start with ‘‘local’’ denoted observables, that couple staggered fermions from the same sites only. The term $\bar{\chi}(x) \chi(x)$ is an example, $\bar{\chi}(x) U_\mu(x) \chi(x + \hat{\mu})$ is not. The condition for a ‘‘local’’

operator is that its structure in taste space and in Dirac space are the same. One can find this by expanding eqn. (5.64)

$$\langle q|O_{ST}|q\rangle = \sum_{\rho,\rho',y} \bar{\chi}_y(\rho)U_y^\dagger(\rho)U_y(\rho')\chi_y(\rho')\text{Tr}(\Gamma_\rho^\dagger\gamma_S\Gamma_{\rho'}\gamma_T). \quad (5.65)$$

Here, both γ_S and γ_T are 4×4 matrices, one can choose the Clifford algebra as the basis for spinor and taste space matrices. Consequently, O_{ST} is non-zero only if the numbers of all the 4 γ_μ matrices are even in the product $\Gamma_A^\dagger\gamma_S\Gamma_B\gamma_T$. So the condition for a “local” operators is $\gamma_S = \gamma_T$.

The advantage for “local” operators is that they are easy to compute, another reason for choosing “local” operators is that particles defined this way usually have the lowest mass among all the possible definitions [9].

The next question is the content of fermionic operators defined this way in terms of staggered fermion fields. Let us expand the corresponding “local” operator of $\bar{\psi}\gamma_\mu\psi$

$$\begin{aligned} \bar{q}(\gamma_\mu \otimes \gamma_\mu)q &= \sum_y \bar{q}_{a,\alpha}(y)\gamma_{\alpha,\beta}^\mu q_{\beta,b}(y)\gamma_{b,a}^\mu \\ &= \sum_y \sum_{\rho,\rho'} \bar{\chi}_y(\rho)U_y^\dagger(\rho)U_y(\rho')\chi_y(\rho')\Gamma_{a,\alpha}^{\rho\dagger}\gamma_{\alpha,\beta}^\mu\Gamma_{\beta,b}^{\rho'}\chi_y(\rho')\gamma_{b,a}^\mu \\ &= \sum_{y,\rho} 4\eta_5(x)(-1)^4(-1)^{x_\mu-1}\bar{\chi}_y(\rho)U_y^\dagger(\rho)U_y(\rho)\chi_y(\rho) \\ &= -\sum_{y,\rho} 4\eta_5(x)(-1)^{x_\mu}\bar{\chi}_y(\rho)U_y^\dagger(\rho)U_y(\rho)\chi_y(\rho). \end{aligned} \quad (5.66)$$

If we adopt the definite path definition of U_ρ in eqn. (5.57), one gets $U_y(\rho)U_y^\dagger(\rho) = 1$ and can simplify this expression to

$$\bar{q}(\gamma_\mu \otimes \gamma_\mu)q = 4 \sum_y \eta_5(x)(-1)^{x_\mu}\bar{\chi}(x)\chi(x). \quad (5.67)$$

The condensates with trivial structure in taste space, $\gamma_T = \mathbf{1}$, is different:

$$\begin{aligned} \bar{q}(\gamma_\mu \otimes \mathbf{1})q &= \sum_y \bar{q}_{a,\alpha}(y)\gamma_{\alpha,\beta}^\mu q_{\beta,b}(y)\mathbf{1}_{b,a} \\ &= \sum_y \sum_{\rho,\rho'} \bar{\chi}_y(\rho)U_y^\dagger(\rho)U_y(\rho')\chi_y(\rho')\Gamma_{a,\alpha}^{\rho\dagger}\gamma_{\alpha,\beta}^\mu\Gamma_{\beta,b}^{\rho'}\mathbf{1}_{b,a} \\ &= \sum_y \sum_{\rho,\rho'} 4\eta_\mu(\rho')\bar{\chi}_y(\rho)U_y^\dagger(\rho)U_y(\rho')\chi_y(\rho')(\delta_{\rho+\mu,\rho'} + \delta_{\rho-\mu,\rho'}) \\ &= \sum_y \sum_{\rho,\rho'} 4\eta_\mu(\rho')\bar{\chi}_y(\rho)U_y^\dagger(\rho)U_y(\rho')\chi_y(\rho')(\delta_{\rho+\mu,\rho'} + \delta_{\rho-\mu,\rho'}). \end{aligned} \quad (5.68)$$

The staggered form of the simplest operator $\langle q|q \rangle$ is that of $\gamma_T = \gamma_S = \mathbf{1}$:

$$\begin{aligned}
\bar{q}(\mathbf{1} \otimes \mathbf{1})q &= \sum_y \bar{q}_{a,\alpha}(y) \mathbf{1}_{\alpha,\beta} q_{\beta,b}(y) \mathbf{1}_{b,a} \\
&= \sum_y \sum_{\rho,\rho'} \bar{\chi}_y(\rho) U^\dagger(\rho) U(\rho') \chi_y(\rho') \Gamma_{a,\alpha}^{\rho\dagger} \mathbf{1}_{\alpha,\beta} \Gamma_{\beta,b}^{\rho'} \mathbf{1}_{b,a} \\
&= \sum_y \sum_{\rho} 4 \bar{\chi}_y(\rho) U^\dagger(\rho) U(\rho) \chi_y(\rho) \delta_{\rho,\rho'} \\
&= \sum_x 4 \bar{\chi}(x) \chi(x) = 4,
\end{aligned} \tag{5.69}$$

it telling us that we should normalize our results by 4 which is from the number of tastes. Another operator with a simple form on the staggered fermion level is $\langle \bar{q}\gamma_0 q \rangle$ with $\gamma_T = \mathbf{1}$ (a particular case of eqn. 5.68):

$$\bar{q}(\gamma_0 \otimes \mathbf{1})q = \sum_y \sum_{\vec{\rho}} 4 \eta_0(\vec{\rho}) (\bar{\chi}_y(0, \vec{\rho}) U_y(0, \vec{\rho}) \chi(1, \vec{\rho}) + c.c). \tag{5.70}$$

where $\vec{\rho}$ are the spatial components of ρ , and the $U_y(0, \vec{\rho})$ is a single link rather than a path of links in the general case in eqn. ((5.68)).

There is another way of defining $\frac{\partial}{\partial \mu} \ln Z = \frac{1}{V_4} \langle \text{Tr} ((D+m)^{-1} \partial_\mu (D+m)) \rangle$, which is purely on lattice and can be used to derive an expression for the quark density of staggered fermions [9]. It implements the chemical potential by

$$U_0(\mu) = e^\mu U_0, \quad U_0^\dagger(\mu) = e^{-\mu} U_0^\dagger. \tag{5.71}$$

So the $\partial_\mu (D+m)$ as a matrix on lattice is

$$\left(\frac{\partial}{\partial \mu} (D(\mu) + m) \right) \Big|_{\mu \rightarrow 0} \Big|_{x,y} = \eta_0(x) (\delta_{x,y+\hat{0}} U_0^\dagger(y) + \delta_{x,y-\hat{0}} U_0(y - \hat{0})). \tag{5.72}$$

which is the same to eqn. (5.70) (if we average eqn. (5.70) over all possible definitions of hypercubes). So the quark density at $\mu = 0$ defined this way is the same to ours (with $\gamma_T = \mathbf{1}$).

So far we did not discuss the link $U(\rho)$ appearing in the operators above, the problem is the definition of the link in eqn. (5.57).

To repeat, there are two possible choices, the first one in eqn. (5.58) is to fix a path for each point $x = 2y + \rho$ in the hypercube to the base site y of the hypercube, the second one is the permutation definition which averages over all pathes from x to y .

The latter [90] in eqn. (5.59) is smoother because it averages over many pathes. But it also has a problem, the orthogonality problem. The corresponding ‘‘recovered’’ Dirac fermions of two orthogonal staggered fermion fields are not orthogonal anymore, We can find this by expanding $\langle q_1|q_2 \rangle$:

$$\langle q_1|q_2 \rangle = \sum_y \sum_{\rho} \bar{\chi}_{1,y}(\rho) U_y^\dagger(\rho) U_y(\rho) \chi_{2,y}(\rho). \tag{5.73}$$

If $U_y(\rho)$ includes only one path, then it is a unitary matrix which gives $U_y^\dagger(\rho) U_y(\rho) = 1$ and consequently $\langle q_1|q_2 \rangle = \langle \chi_1|\chi_2 \rangle = 0$. But if $U_y(\rho)$ includes

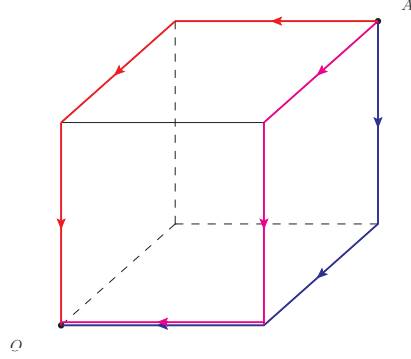


Figure 5.7: Different paths of links in the permutation definition of $U_y(\rho)$ in a cube from a site ρ to the base site O .

different paths, $U_y(\rho)$ is not unitary, and $\langle q_1|q_2\rangle \neq \langle \chi_1|\chi_2\rangle$. Starting with orthogonal staggered fermion fields χ_1 and χ_2 , we get non-orthogonal fermions q_1 and q_2 . Re-orthogonalization, which one might suggest, can give $\langle q'_1|q'_2\rangle = 0$, but will mix χ_1 and χ_2 .

Along with the orthogonal problem is the normalization problem, replacing q_2 by q_1 in eqn. (5.73), one finds that with permutation definition of $U_y(\rho)$, the “recovered” fermion fields are not properly normalized. One can normalize it, but the factor depends both on the configuration and the fermion field.

5.4.4 General fermionic observables

We select 7 operators: $\{\gamma_S = \mathbf{1}, \gamma_0, \gamma_0\gamma_5, \gamma_5; \gamma_T = \mathbf{1}, \gamma_S\}$, all the other structures in the spinor space will give vanishing condensates because of rotational invariance as they include γ_i (γ_0 is distinguished at finite temperature). The corresponding condensates of these 7 operators are

$$\Sigma_{ST}(\phi) = \sum_{\lambda_\phi} \frac{\langle \nu_{i\lambda_\phi} | O_{ST} | \nu_{i\lambda_\phi} \rangle}{m + i\lambda_\phi}. \quad (5.74)$$

These operator condensates are either purely real or purely imaginary as we will find below.

The expectation values $\langle \nu | O_{ST} | \nu \rangle$ of a local operator ($\gamma_S = \gamma_T$) is real because the sum of the contributions from a pair of eigenmodes ($\pm i\lambda$) is real. Using the relation $\nu_- = \eta_5 \nu_+$ (the continuous version is $\nu_- = \gamma_5 \nu_+$) between two eigenmodes in a pair ν_+ and ν_- that satisfies $D\nu_+ = i\lambda\nu_+$ and $D\nu_- = -i\lambda\nu_-$ respectively, we find the expectation value of the ν_- is

$$\begin{aligned} \langle \nu_- | O_{S=T} | \nu_- \rangle &= \sum_y \sum_\rho \bar{\nu}_{+y}(\rho) \eta_5(\rho) \eta_5(\rho) \nu_{+y}(\rho) \text{Tr}(\Gamma_\rho^\dagger \gamma_S \Gamma_\rho \gamma_S) \\ &= \sum_y \sum_\rho \bar{\nu}_{+y}(\rho) \nu_{+y}(\rho) \text{Tr}(\Gamma_\rho^\dagger \gamma_S \Gamma_\rho \gamma_S) \\ &= \langle \nu_+ | O_{S=T} | \nu_+ \rangle. \end{aligned} \quad (5.75)$$

It is real because $\text{Tr}(\Gamma_\rho^\dagger \gamma_S \Gamma_\rho \gamma_S)$ is always real.

The sum of the contributions from this pair of eigenmodes ν_+ and ν_- to the condensate $\langle \bar{\psi} O_{S=T} \psi \rangle$ is

$$\begin{aligned} \frac{\langle \nu_+ | O_{S=T} | \nu_+ \rangle}{i\lambda + m} + \frac{\langle \nu_- | O_{S=T} | \nu_- \rangle}{-i\lambda + m} &= \frac{\langle \nu_+ | O_{S=T} | \nu_+ \rangle}{i\lambda + m} + \frac{\langle \nu_+ | O_{S=T} | \nu_+ \rangle}{-i\lambda + m} \\ &= \frac{2\langle \nu_+ | O_{S=T} | \nu_+ \rangle m}{\lambda^2 + m^2}, \end{aligned} \quad (5.76)$$

which is purely real. So we know that the general condensates $\Sigma_{ST}(\phi)$ of local operators $O_{S=T}$ with arbitrary boundary angle ϕ are purely real.

Let us consider the other 3 condensates which $\gamma_T = \mathbf{1}$ namely $\gamma_S = \gamma_0, \gamma_0\gamma_5$ or γ_5 . One will find the general condensates of these 4 operators are either purely real or purely imaginary.

The proofs include two parts, the first part is the relation between $\langle \nu_+ | \mathbf{1}^T \otimes \gamma_S | \nu_+ \rangle$ and $\langle \nu_- | \mathbf{1}^T \otimes \gamma_S | \nu_- \rangle$:

$$\begin{aligned} &\langle \nu_- | \mathbf{1}^T \otimes \gamma_S | \nu_- \rangle \\ &= \sum_y \sum_{\rho, \rho'} \bar{\nu}_{+y}(\rho) \eta_5(\rho) U_y^\dagger(\rho) U_y(\rho') \eta_5(\rho') \nu_{+y}(\rho') \text{Tr}(\Gamma_\rho^\dagger \mathbf{1}^T \Gamma_{\rho'} \gamma_S) \\ &= n_\gamma(S) \langle \nu_+ | \mathbf{1}^T \otimes \gamma_S | \nu_+ \rangle \end{aligned} \quad (5.77)$$

where $n_\gamma(S)$ is the number of γ_μ matrices in γ_S . $n_\gamma = 0$ for $\mathbf{1}$, $n_\gamma = 1$ for γ_μ , $n_\gamma = 2$ for $\sigma_{\mu,\nu}$, $n_\gamma = 3$ for $\gamma_\mu\gamma_5$ and $n_\gamma = 4$ for γ_5 . So the sign between $\langle \nu_- | \mathbf{1}^T \otimes \gamma_S | \nu_- \rangle$ and $\langle \nu_+ | \mathbf{1}^T \otimes \gamma_S | \nu_+ \rangle$ is “-” for $\gamma_S = \gamma_0$ and $\gamma_0\gamma_5$, is “+” for $\gamma_S = \gamma_5$.

The second part of the proof is that for any eigenmode ν , $\langle \nu | \mathbf{1}^T \otimes \gamma_S | \nu \rangle$ is either purely imaginary or purely real.

$$\begin{aligned} &\langle \nu | \mathbf{1}^T \otimes \gamma_S | \nu \rangle \\ &= \frac{1}{2} \sum_y \sum_{\rho, \rho'} [\bar{\nu}_y(\rho) U_y^\dagger(\rho) U_y(\rho') \nu_y(\rho') \text{Tr}(\Gamma_\rho^\dagger \mathbf{1}^T \Gamma_{\rho'} \gamma_S) \\ &\quad + \bar{\nu}_y(\rho') U_y^\dagger(\rho') U_y(\rho) \nu_y(\rho) \text{Tr}(\Gamma_{\rho'}^\dagger \mathbf{1}^T \Gamma_\rho \gamma_S)] \\ &= \frac{1}{2} \sum_y \sum_{\rho, \rho'} [C_y(\rho, \rho') \text{Tr}(\Gamma_\rho^\dagger \Gamma_{\rho'} \gamma_S) + C_y^*(\rho, \rho') \text{Tr}(\Gamma_{\rho'}^\dagger \Gamma_\rho \gamma_S)] \\ &= \frac{1}{2} \sum_y \sum_{\rho, \rho'} [C_y(\rho, \rho') \text{Tr}(\Gamma_\rho^\dagger \Gamma_{\rho'} \gamma_S) + C_y^*(\rho, \rho') \text{Tr}(\Gamma_\rho^\dagger \Gamma_{\rho'} \gamma^{S\dagger})] \end{aligned} \quad (5.78)$$

where $C_y(\rho, \rho') = \bar{\nu}_y(\rho) U_y^\dagger(\rho) U_y(\rho') \nu_y(\rho')$ is a complex number and $\text{Tr}(\Gamma_\rho^\dagger \Gamma_{\rho'} \gamma_S) \in \{\pm 4, 0\}$ is real. In the Euclidean space time, $(\gamma_0)^\dagger = \gamma_0$, $(\gamma_5)^\dagger = \gamma_5$ and $(\gamma_0\gamma_5)^\dagger = -\gamma_0\gamma_5$. So we get $\langle \nu | \mathbf{1}^T \otimes \gamma_S | \nu \rangle$ is purely real for the $\gamma_S = \gamma_0$ and γ_5 cases while it is purely imaginary for $\gamma_S = \gamma_0\gamma_5$ case.

The two parts of the proof together give a purely imaginary result for the general condensate corresponding to $O_{ST} = \{\gamma_T = \mathbf{1}, \gamma_S = \gamma_0\}$ and purely real results for $O_{ST} = \{\gamma_T = \mathbf{1}, \gamma_S = \gamma_0\gamma_5, \gamma_5\}$. Table 5.1 summarizes the results of the 7 general condensates, the conclusion is independent of ϕ .

γ_T	γ_S	$\Sigma_{ST}(\phi)$
$\mathbf{1}$	$\mathbf{1}$	purely real
$\mathbf{1}$	γ_0	purely imaginary
$\mathbf{1}$	$\gamma_0\gamma_5$	purely real
$\mathbf{1}$	γ_5	purely real
γ_0	γ_0	purely real
$\gamma_0\gamma_5$	$\gamma_0\gamma_5$	purely real
γ_5	γ_5	purely real

Table 5.1: The 7 general condensates are either purely real or purely imaginary.

One should notice that the 7 condensates $\Sigma_{ST}(\phi)$ listed above being either purely real or purely imaginary does not mean the corresponding dual observables $\tilde{\Sigma}_{SF}$ are purely real or purely imaginary.

The last operator $O_{ST} = \{\gamma_T = \gamma_5, \gamma_S = \gamma_5\}$ vanishes generically. We first simplify it:

$$\begin{aligned}
\sum_y \bar{q}_{a,\alpha}(y) \gamma_{\alpha,\beta}^5 q_{\beta,b}(y) \gamma_{b,a}^5 &= \sum_y \sum_\rho \bar{\chi}_y(\rho) \chi_y(\rho) \text{Tr}[\Gamma^{\rho\dagger} \gamma^5 \Gamma^\rho \gamma^5] \\
&= \sum_y \sum_\rho \bar{\chi}_y(\rho) \eta_5(\rho) \chi_y(\rho) \\
&= \bar{\chi} \eta_5 \chi.
\end{aligned} \tag{5.79}$$

To this expression, only exact zero modes contribute, and they are absent for generic staggered configurations.

5.5 Numerical results

We use smeared dynamical improved staggered fermion configurations from [8] on lattices of size 8×24^3 , for temperatures ranging from 78 MeV to 890 MeV, lattice spacings from 0.282 fm to 0.028 fm and β from 3.3226 to 4.66. We compute the 500 lowest eigenmodes of the staggered Dirac operator D and the corresponding expectation values $\langle \nu | \Gamma | \nu \rangle$ for the seven operators discussed in the previous section for 8 equally spaced boundary conditions (see App. 7.2) $\varphi \in [0, 2\pi]$ by PARPACK [65] on the supercomputer Athene at the University of Regensburg and on HLRB2 of Leibniz-Rechenzentrum München (project No.pr42ni).

Among the 7 dual observables of fermionic operator condensates in section 5.4.4, we find that only the dual quark condensate and the dual quark density have clear signals as order parameters of the QCD crossover.

5.5.1 General quark condensate

The general quark condensate $\Sigma(\phi)$ as a function of the boundary angle ϕ and the temperature T is shown in Fig. 5.8, at specific temperatures it is also shown in Fig. 5.9. $\phi = \pi$ is the physical boundary condition, $\phi = 0$ or 2π is the periodic boundary condition far from the physical one (valence quarks couple with

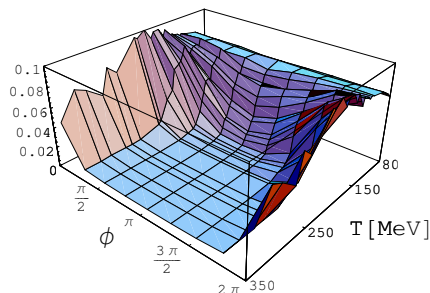


Figure 5.8: (Unrenormalized) general quark condensate $\tilde{\Sigma}_1$ as a function of the temperature T and the boundary angle ϕ at probe mass $m = 1\text{MeV}$.

largest imaginary chemical potential). At low temperature, the general quark condensate $\Sigma(\phi)$ is almost flat. With increasing temperature, $\Sigma(\phi)$ becomes a curve with an almost perfect cosine behavior, compatible with the quenched lattice data [12]. At very high temperature, $\Sigma(\phi)$ is flat everywhere except near $\phi = 0$.

5.5.2 Dual condensate

We get dual condensate results from the spectrum. Because of the limited computational resources, we can only calculate the lowest parts of the spectra. It means that we can only get the contributions from the lowest part of spectra, is the result converged? Arguments in section 5.1.1 tell us that the dual condensate is infrared dominated, quenched numerical results of the dual condensate in [92, 93] have confirmed infrared dominance. Our results of accumulated contributions to the dual condensate are shown in Fig. 5.10 and also confirm the infrared dominance.

The dual condensate connects center symmetry breaking and chiral symmetry restoration, we find its behavior in the small mass limit reflects this. In the large mass limit, the dual condensate is proportional to Polyakov loop, so it grows with the temperature increasing. In the small mass limit, there are two trends for the dual condensate with the growth of temperature [104], the first is caused by chiral symmetry restoration. Although the transition temperature depends on the boundary condition, the chiral condensate with all the boundary conditions decreases with the increasing temperature. This trend demands the dual condensate to decrease with temperature increasing. On the other hand, the dual condensate is the first Fourier component of the general quark condensate, or in other words, it reflects the boundary condition angle ϕ dependence of the chiral condensate, so center symmetry breaking wants the dual condensate to grow with temperature increasing. Consider that the temperature of chiral symmetry restoration and center symmetry breaking could be different, there are two scenarios of the dual condensate in chiral limit as shown in Fig. 5.11.

Our numerical results for the dual condensates with different masses are shown in Fig. 5.12 (left panel). They show that the dual condensates change at the crossover like order parameters indeed. The dual condensate shows a tendency to change with the mass, it is similar to the Polyakov loop shown in

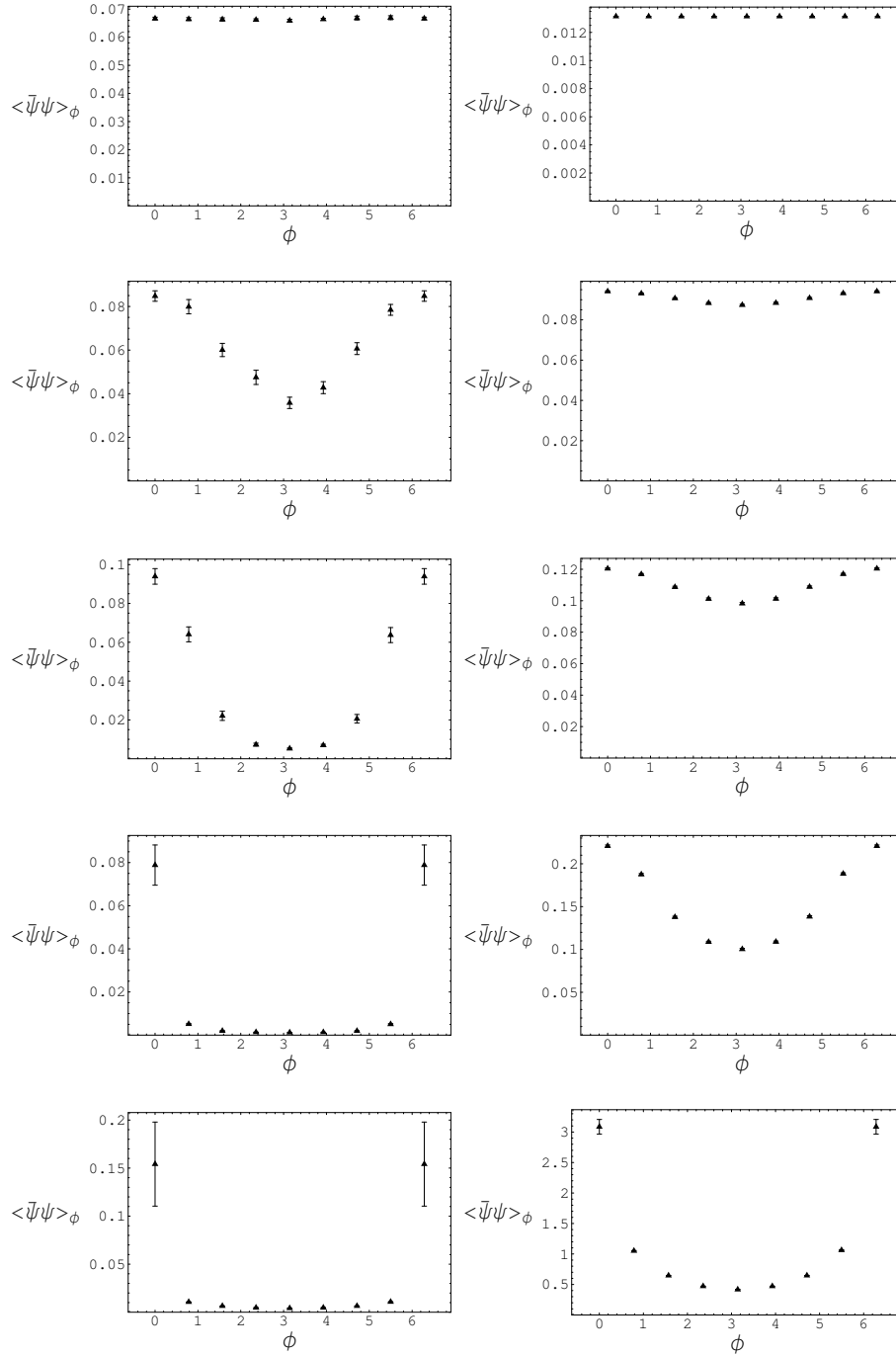


Figure 5.9: (Unrenormalized) general quark condensate $\Sigma(\phi)$ [GeV^4] at temperatures $T = 74\text{MeV}$, $T = 152\text{MeV}$, $T = 172\text{MeV}$, $T = 250\text{MeV}$ and $T = 892\text{MeV}$ from the first to the last row. The mass parameter is $m = 1\text{MeV}$ for plots in the left column, and $m = 100\text{MeV}$ in the right column.

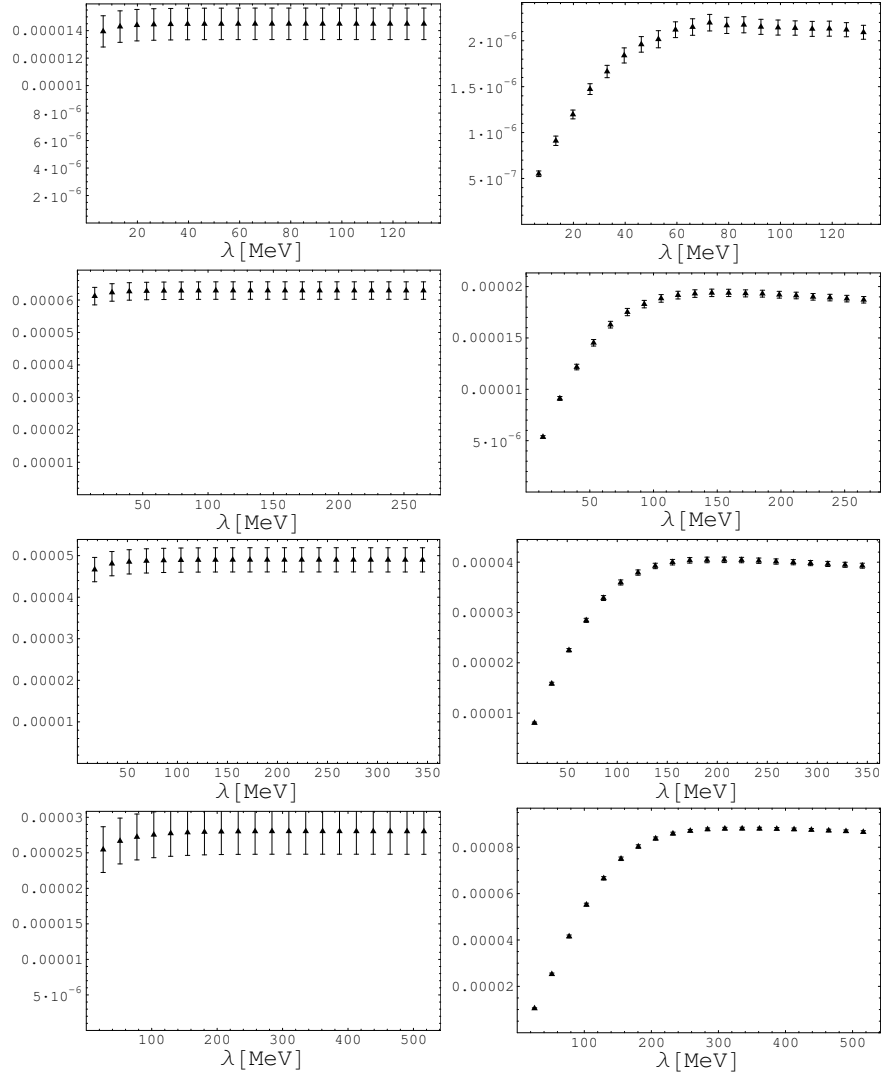


Figure 5.10: Accumulated contributions of the renormalized dual condensate $\tilde{\Sigma}_R$ [GeV⁴]. The temperature from the first row to the last is 129MeV, 172MeV, 197MeV and 250MeV, respectively. The masses is $m = 1$ MeV for the left column and is $m = 100$ MeV for the right column.

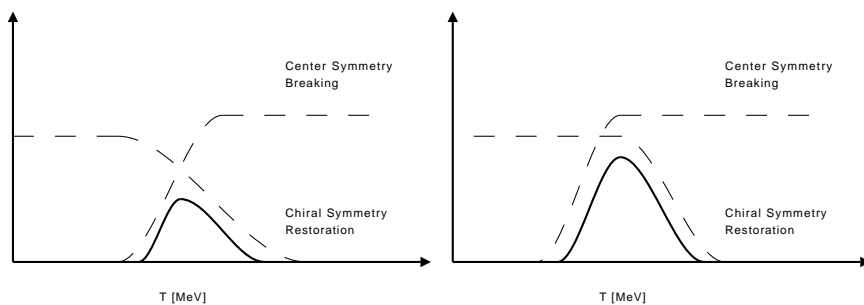


Figure 5.11: Both scenarios of the dual condensate in the chiral limit give a peak between the chiral symmetry restoration temperature and center symmetry breaking temperature [94]. $T_C(P) > T_C(\chi)$ (left) and $T_C(\chi) > T_C(P)$ (right).

Fig. 5.13 (left panel) for large masses, and gives a peak as we expected from Fig. 5.11 in the chiral limit.

As we mentioned in section 5.1.1, the dual condensate is the dressed Polyakov loop. We show its free energy using eqn. (5.11) with $m_X = 1\text{GeV}$ for simplicity in Fig. 5.12 (right panel) and compare it to the free energy from the conventional Polyakov loops in Fig. 5.13 (right panel). We find the crossover temperatures in the dual condensate as the inflection points of the free energy (the $4T \ln m_X$ term can dominate the scale, but as it is a linear term, the inflection point does not feel it).

Table 5.2 shows the mass dependence of the crossover temperature, higher crossover temperature for larger mass. It agrees with the expectation: in the large mass limit, the dual condensate is proportional to Polyakov loop while in chiral limit the dual condensate becomes dual (chiral) condensate and reflects the features of chiral condensate. We can compare it with crossover temperature from Wuppertal-Budapest group [9] results are $T_C(\langle \bar{\psi}\psi \rangle_R) = 155(3)(3)$ and $T_C(L) = 170(4)(3)$ (these are continuum limits, $N_t = 8$ ones are lower, $T_C(L) \approx 166\text{MeV}$ and $T_C(L) \approx 151\text{MeV}$, read from Fig.4 of [7]).

$m[\text{MeV}]$	$T_c[\text{MeV}]$
1	128(12)
10	143(2)
100	156(4)

Table 5.2: Crossover temperature as the inflection points of $-T \ln \tilde{\Sigma}_R$ with $m = 1 \sim 100\text{MeV}$ (we get T_c by fitting the free energy as a fifth order polynomial of temperature).

5.5.3 Dual quark density

The general quark density $n(\phi)$ is purely imaginary, its imaginary part is shown in Fig. 5.14. It is odd around the physical boundary condition $\phi = \pi$ on average, so it basically includes $i \sin k\phi$ components only, which means the dual quark density \tilde{n}_k is approximately real. As the general quark density is less IR

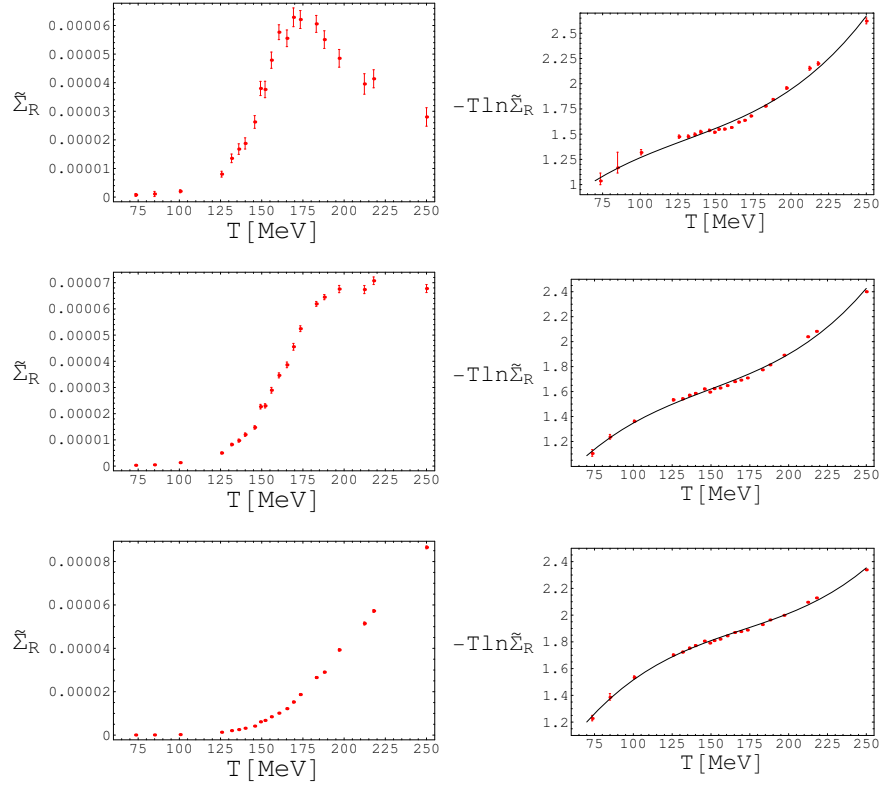


Figure 5.12: Renormalized dual condensate $\tilde{\Sigma}_R$ [GeV^3] and its “free energy” $F' + 4T \ln M + c = -T \ln \tilde{\Sigma}_R$ in the left and right columns respectively ($m_X = 1 \text{ GeV}$ for simplicity in this figure and we fitted the free energy curve as polynomials of temperature). The mass is $m = 1 \text{ MeV}$ for the upper panel, $m = 10 \text{ MeV}$ and $m = 100 \text{ MeV}$ for the middle and lower panel respectively.

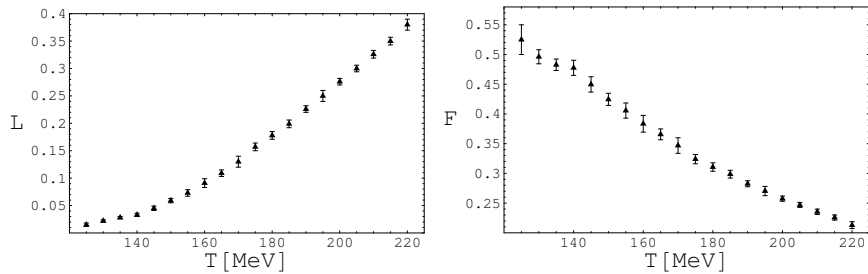


Figure 5.13: The left panel shows renormalized Polyakov loop L and the right panel shows $F(T) + c = -T \ln L$ from [9].

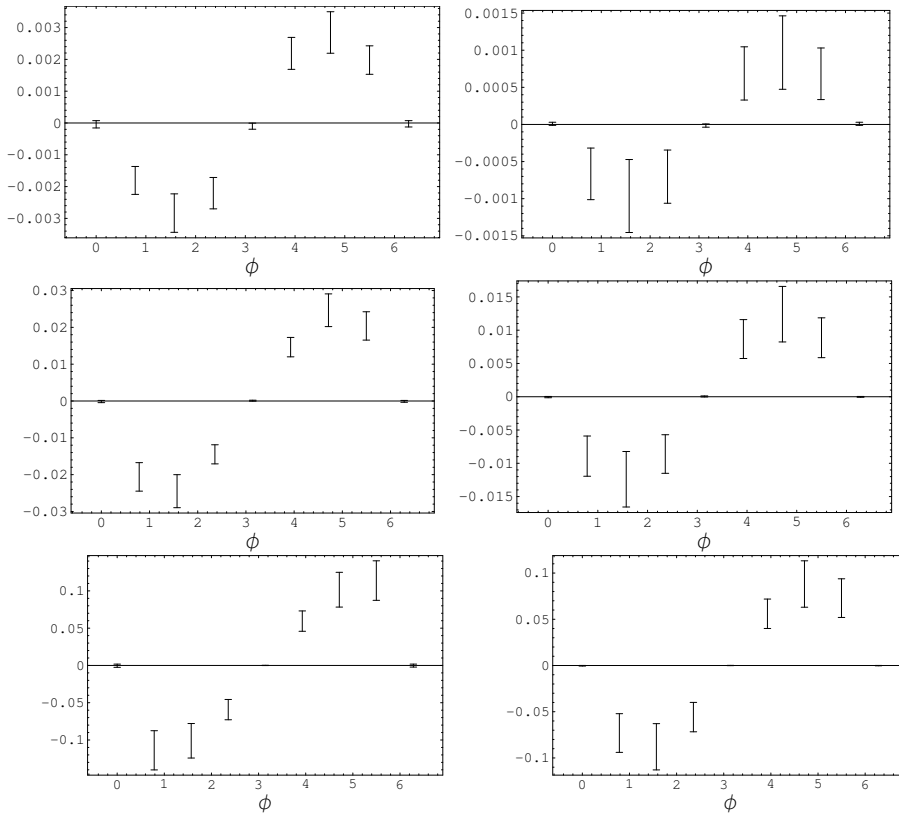


Figure 5.14: The imaginary part of general quark density $n(\phi)$ as a function of the boundary angle ϕ . Bounds are estimated with eqn. (5.37). The temperature is $T = 129\text{MeV}$ (upper row), 172MeV (middle) and 250MeV (lower), while the mass is $m = 1\text{MeV}$ and 100MeV in the left and right column respectively.

dominated than the general quark condensate, Fig. 5.14 gives the upper and lower bounds only, in which the higher spectrum contributions are estimated using eqn. (5.37).

Fig. 5.15 shows the resulting dual quark density divided by T^3 , $-\tilde{n}_1/T^3$ for two different masses, and Fig. 5.16 shows dual quark densities of higher windings $-\tilde{n}_2/T^3$ and $-\tilde{n}_3/T^3$ (related to the deviation of $n(\phi)$ from a pure $-\sin(\phi)$). Similar to Fig. 5.14, we give the bounds only. The high temperature limits agree with the Stefan-Boltzmann limit computed in eqn. (5.28) taking into account the staggered fermion redundancy of 4 and an extra 1.28844 factor from the lattice/continuous $\ln Z$ difference at $N_t = 8$ by dividing them. This result is similar to the Stefan-Boltzmann limit of pressure in [95]. As the dual quark densities are less IR dominated, we will use the stochastic vector method to calculate the dual quark density in the future as the spectral method we are using is not really suitable for less IR dominated observables like this one.

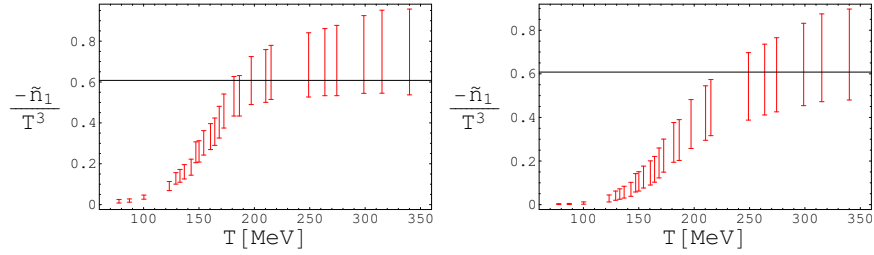


Figure 5.15: Dual quark density divided by the third power of temperature $-\tilde{n}_1(T)/T^3$ as a function of temperature, the probe mass is $m = 1\text{MeV}$ and 100MeV for the left and right panels respectively. Bounds are estimated with eqn. (5.37). The horizontal line is the theoretical Stefan-Boltzmann limit of $-\tilde{n}_1(T)/T^3|_{T \rightarrow \infty} \rightarrow 6/\pi^2$.

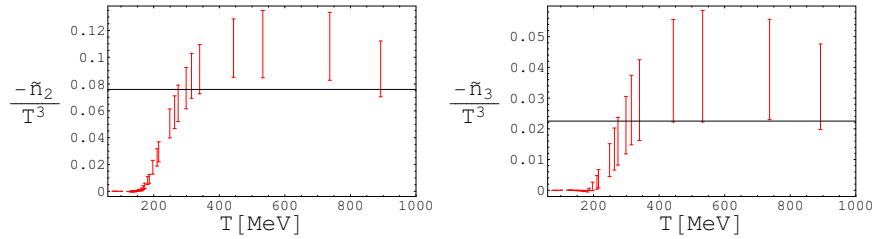


Figure 5.16: Dual quark density with higher windings, divided by the third power of temperature, $-\tilde{n}_2(T)/T^3$ (left) and $-\tilde{n}_3(T)/T^3$ (right), the probe mass is $m = 100\text{MeV}$. The horizontal lines are the theoretical Stefan-Boltzmann limits given in eqn. (5.28).

Chapter 6

Summary

In this thesis, we have explored the relations between chiral symmetry breaking and confinement in the QCD phase transition/crossover in two aspects.

The first one is the relation between different topological objects, which are candidates for the non-perturbative degrees of freedom in the QCD vacuum. The most important topological objects are vortices, monopoles and instantons, calorons are finite temperature instantons. Among them, vortices and monopoles are closely related to confinement, whereas instantons have closer relations to chiral symmetry breaking (calorons are related to confinement through their holonomy). The connections between calorons and monopoles (dyons as their constituents) and between vortices and monopoles (in Abelian and center projections) are well established. So in this thesis we investigated the remaining connection between calorons and vortices.

We have determined the vortex content of $SU(2)$ calorons and ensembles made of them mainly by the virtue of Laplacian Center Gauge in Chapter 3. The vortex surface from a single caloron has two parts. The first part are two magnetic fluxes induced by the magnetic charges, generically they extend in space and time. The purely spatial part of the vortex surface in a single caloron is a “bubble” around one of the dyons, depending on the holonomy. We have shown that it is induced by the relative twist between constituent dyons. The two intersection points of these two parts of vortex surface reproduce the unit topological charge of the caloron. The bubble degenerates into the mid plane of the two constituent dyons in the case of maximal nontrivial holonomy where the asymptotic Polyakov loop vanishes. In dilute caloron ensembles, the vortices are approximately a recombination of vortices from individual calorons. The spatial vortices in ensembles with close to trivial holonomies are small bubbles, while with the holonomy approaching the maximal nontrivial case the bubbles grow, merge with each other and form percolating vortex surfaces. Taking trivial and maximal nontrivial holonomy as equivalent to the deconfined and confined phase, respectively, this is exactly the feature of vortices expected in these phases. It shows that calorons are suitable to facilitate the vortex (de)confinement mechanism.

In Chapter 4 we have extended our findings to vortices in $SU(3)$ calorons. In this case, Laplacian center gauge was found to suffer from an ambiguity as one needs to choose particular operators in the gauge fixing, here 2 of the 3 non-diagonal entries of the first excited mode. We have demonstrated, that

spatial vortices again follow the relative twist, but also that different choices give different vortex contents indeed. This and the relation of $SU(3)$ caloron vortices to percolation and to different phases still needs to be clarified. The concept of thick vortices or other methods like IMCG and DMCG might be helpful here.

The second part of this thesis is devoted to order parameters near the QCD transition. The chiral condensate and the Polyakov loop are among the most important ones as they probe chiral symmetry breaking and confinement, respectively. The dual condensate is an order parameter that connects the Polyakov loop and the chiral condensate. It is the first Fourier component of the general quark condensate with respect to the boundary conditions. Its use as an order parameter had been demonstrated so far only in the quenched case. We have investigated the dual condensate and another dual operator – the dual quark density – in Chapter 5. The presented numerical results have been obtained on dynamical lattice configurations with physical pion masses using staggered fermions. We see that the dual condensate behaves as an order parameter. The crossover from the dual condensate temperature shows a trend to increase with the probe mass m , in which process the dual condensate moves from the chiral limit, where it has a close relation to the chiral condensate to the heavy quark limit, in which it can be shown to approach the Polyakov loop. The same trend of crossover temperature has been observed in the conventional chiral, strange condensates and Polyakov loop observables.

The dual quark density, although less IR dominated, displays a different dependence on the boundary condition (which can be understood), but also has a clear order parameter behavior. Interestingly, it is related to the quark number susceptibility and approaches a Stefan-Boltzmann limit as we have expected theoretically for different winding numbers.

More numerical efforts are needed to determine these quantities more precisely and to perform the continuum limit. Dual quantities are certainly useful observables in the QCD phase crossover not only in lattice simulations but also by other approaches like those mentioned in section 5.1.2. They might also be useful to find the influence of e.g. an external magnetic field on the QCD phase transition.

Bibliography

- [1] D. J. Gross, F. Wilczek, Phys. Rev. Lett. **30** (1973) 1343-1346.
- [2] M. G. Alford, A. Schmitt, K. Rajagopal and T. Schafer, Rev. Mod. Phys. **80** (2008) 1455 [arXiv:0709.4635 [hep-ph]].
- [3] L. D. McLerran and B. Svetitsky, Phys. Rev. D **24** (1981) 450.
- [4] H. J. Rothe, “Lattice gauge theories – an introduction” *World Scientific (2005)*.
- [5] L. S. Brown and W. I. Weisberger, Phys. Rev. D **20** (1979) 3239.
- [6] J. Greensite, Eur. Phys. J. ST **140** (2007) 1-52.
- [7] Y. Aoki, Z. Fodor, S. D. Katz and K. K. Szabo, Phys. Lett. B **643** (2006) 46 [arXiv:hep-lat/0609068].
- [8] Y. Aoki, S. Borsanyi, S. Durr, Z. Fodor, S. D. Katz, S. Krieg, K. K. Szabo, JHEP **0906** (2009) 088 [arXiv:0903.4155 [hep-lat]].
- [9] S. Borsanyi *et al.* [Wuppertal-Budapest Collaboration], JHEP **1009** (2010) 073 [arXiv:1005.3508 [hep-lat]].
- [10] M. Cheng *et al.*, Phys. Rev. D **81** (2010) 054504 [arXiv:0911.2215 [hep-lat]].
- [11] C. Gattringer, Phys. Rev. Lett **97** (2006) 032003 [arXiv:hep-lat/0605018].
- [12] E. Bilgici, F. Bruckmann, C. Gattringer and C. Hagen, Phys. Rev. D **77** (2008) 094007 [arXiv:0801.4051 [hep-lat]].
- [13] B. Zhang, F. Bruckmann and E. M. Ilgenfritz, PoS **LAT2009** (2009) 235 [arXiv:0911.0320 [hep-lat]].
- [14] F. Bruckmann, E. M. Ilgenfritz, B. Martemyanov and B. Zhang, Phys. Rev. D **81** (2010) 074501 [arXiv:0912.4186 [hep-th]].
- [15] F. Bruckmann, E. M. Ilgenfritz, B. Martemyanov and B. Zhang, arXiv:1011.6178 [hep-th].
- [16] Bo-Yuan.Hou and Bo-Yu.Hou, “Differential Geometry for Physicist” (in Chinese), *Science Press (2004)*.
- [17] L. H. Ryder, “Quantum Field Theory,” *Cambridge UK: University Press (2005)* .

- [18] P. A. M. Dirac, Proc. Roy. Soc. Lond. **A133** (1931) 60-72.
- [19] T. T. Wu, C. N. Yang, Nucl. Phys. **B107** (1976) 365.
- [20] A. M. Polyakov, JETP Lett. **20** (1974) 194 [Pisma Zh. Eksp. Teor. Fiz. **20** (1974) 430].
- [21] G. 't Hooft, Nucl. Phys. B **79** (1974) 276.
- [22] E. B. Bogomol'nyi, Sov. J. Nucl. Phys. **24**, (1976) 499.
- [23] M. K. Prasad and C. M. Sommerfield, Phys. Rev. Lett. **35** (1975) 760.
- [24] A.A. Belavin, A.M. Polyakov, A.S. Schwartz, Yu.S. Tyupkin, Phys. Lett. **B 59**, (1975) 5.
- [25] B. J. Harrington and H. K. Shepard, Phys. Rev. D **17** (1978) 2122.
- [26] T. C. Kraan and P. van Baal, Nucl. Phys. B **533** (1998) 627 [arXiv:hep-th/9805168].
- [27] K. M. Lee and C. h. Lu, Phys. Rev. D **58** (1998) 025011 [arXiv:hep-th/9802108].
- [28] T. C. Kraan and P. van Baal, Phys. Lett. B **428** (1998) 268 [arXiv:hep-th/9802049];
- [29] M. Garcia Perez, A. Gonzalez-Arroyo, A. Montero and P. van Baal, JHEP **9906** (1999) 001 [arXiv:hep-lat/9903022].
- [30] H. Reinhardt, Nucl. Phys. B **503** (1997) 505 [arXiv:hep-th/9702049].
- [31] C. Ford, U. G. Mitreuter, T. Tok, A. Wipf and J. M. Pawlowski, Annals Phys. **269** (1998) 26, [arXiv:hep-th/9802191];
- [32] O. Jahn and F. Lenz, Phys. Rev. D **58** (1998) 085006, [arXiv:hep-th/9803177].
- [33] E.-M. Ilgenfritz, B. V. Martemyanov, M. Müller-Preussker, S. Shcheredin and A. I. Veselov, Phys. Rev. D **66** (2002) 074503 [arXiv:hep-lat/0206004].
- [34] D. Diakonov, N. Gromov, V. Petrov and S. Slizovskiy, Phys. Rev. D **70** (2004) 036003 [arXiv:hep-th/0404042].
- [35] O. Jahn, J. Phys. A **33** (2000) 2997 [arXiv:hep-th/9909004].
- [36] F. Bruckmann, T. Heinzl, T. Vekua and A. Wipf, Nucl. Phys. B **593** (2001) 545 [arXiv:hep-th/0007119].
- [37] F. Bruckmann, JHEP **0108** (2001) 030 [arXiv:hep-th/0011249].
- [38] R. C. Brower, K. N. Orginos and C. I. Tan, Phys. Rev. D **55** (1997) 6313 [arXiv:hep-th/9610101].
- [39] A. Hart and M. Teper, Phys. Lett. B **371** (1996) 261 [arXiv:hep-lat/9511016].

- [40] P. de Forcrand and M. Pepe, Nucl. Phys. Proc. Suppl. **94** (2001) 498 [arXiv:hep-lat/0010093].
- [41] P. de Forcrand and M. Pepe, Nucl. Phys. B **598** (2001) 557 [arXiv:hep-lat/0008016].
- [42] J. Ambjorn, J. Giedt and J. Greensite, JHEP **0002** (2000) 033 [arXiv:hep-lat/9907021].
- [43] F. Bruckmann, F. Gruber and A. Schafer, Phys. Lett. B **687** (2010) 92 [arXiv:0910.4335 [hep-lat]].
- [44] L. Del Debbio, M. Faber, J. Giedt, J. Greensite and S. Olejnik, Phys. Rev. D **58** (1998) 094501 [arXiv:hep-lat/9801027].
- [45] T. G. Kovacs and E. T. Tomboulis, Phys. Lett. B **463** (1999) 104 [arXiv:hep-lat/9905029].
- [46] L. Del Debbio, M. Faber, J. Greensite and S. Olejnik, Phys. Rev. D **55** (1997) 2298 [arXiv:hep-lat/9610005].
- [47] G. 't Hooft, Nucl. Phys. B **190** (1981) 455.
- [48] A. J. van der Sijs, Prog. Theor. Phys. Suppl. **131** (1998) 149 [arXiv:hep-lat/9803001].
- [49] G. 't Hooft, Nucl. Phys. **B138** (1978) 1.
- [50] M. Engelhardt, K. Langfeld, H. Reinhardt and O. Tennert, Phys. Rev. D **61** (2000) 054504 [arXiv:hep-lat/9904004].
- [51] K. Langfeld, H. Reinhardt and O. Tennert, Phys. Lett. B **419** (1998) 317 [arXiv:hep-lat/9710068].
- [52] K. Langfeld, H. Reinhardt and A. Schafke, Phys. Lett. B **504** (2001) 338 [arXiv:hep-lat/0101010].
- [53] M. Engelhardt, K. Langfeld, H. Reinhardt and O. Tennert, Phys. Lett. B **431** (1998) 141 [arXiv:hep-lat/9801030].
- [54] K. Langfeld, Phys. Rev. D **69** (2004) 014503 [arXiv:hep-lat/0307030].
- [55] A. S. Kronfeld, M. L. Laursen, G. Schierholz and U. J. Wiese, Phys. Lett. B **198**, (1987) 516.
- [56] M. F. Atiyah and I. M. Singer, Annals Math. **93** (1971) 119.
- [57] T. Banks, A. Casher, Nucl. Phys. **B169** (1980) 103.
- [58] E. V. Shuryak, Nucl. Phys. B **203** (1982) 93.
- [59] D. Diakonov and V. Petrov, Phys. Rev. D **76** (2007) 056001 [arXiv:0704.3181 [hep-th]].
- [60] F. Bruckmann, S. Dinter, E.-M. Ilgenfritz, M. Müller-Preussker and M. Wagner, Phys. Rev. D **79** (2009) 116007 [arXiv:0903.3075 [hep-ph]].

- [61] C. Alexandrou, M. D’Elia and P. de Forcrand, Nucl. Phys. Proc. Suppl. **83** (2000) 437 [arXiv:hep-lat/9907028].
- [62] C. Alexandrou, P. de Forcrand and M. D’Elia, Nucl. Phys. A **663** (2000) 1031 [arXiv:hep-lat/9909005].
- [63] P. Gerhold, E.-M. Ilgenfritz and M. Müller-Preussker, Nucl. Phys. B **774** (2007) 268 [arXiv:hep-ph/0610426].
- [64] P. Gerhold, E. M. Ilgenfritz and M. Müller-Preussker, Nucl. Phys. B **760** (2007) 1 [arXiv:hep-ph/0607315].
- [65] ”<http://www.caam.rice.edu/software/ARPACK/>”.
- [66] A. J. van der Sijs, Nucl. Phys. Proc. Suppl. **53** (1997) 535 [arXiv:hep-lat/9608041];
- [67] F. Bruckmann and E.-M. Ilgenfritz, Phys. Rev. D **72** (2005) 114502 [arXiv:hep-lat/0509020].
- [68] R. C. Brower, D. Chen, J. W. Negele, K. Orginos and C. I. Tan, Nucl. Phys. Proc. Suppl. **73** (1999) 557 [arXiv:hep-lat/9810009].
- [69] E. M. Ilgenfritz, B. V. Martemyanov, M. Müller-Preussker and A. I. Veselov, Phys. Rev. D **71** (2005) 034505 [arXiv:hep-lat/0412028].
- [70] M. Garcia Perez, A. Gonzalez-Arroyo and A. Sastre, JHEP **0906** (2009) 065 [arXiv:0905.0645 [hep-th]].
- [71] M. Engelhardt, Nucl. Phys. B **585** (2000) 614 [arXiv:hep-lat/0004013].
- [72] M. Engelhardt and H. Reinhardt, Nucl. Phys. B **567** (2000) 249 [arXiv:hep-th/9907139].
- [73] F. Bruckmann and M. Engelhardt, Phys. Rev. D **68** (2003) 105011 [arXiv:hep-th/0307219].
- [74] H. Reinhardt, Nucl. Phys. B **628** (2002) 133 [arXiv:hep-th/0112215].
- [75] K. Langfeld, O. Tennert, M. Engelhardt and H. Reinhardt, Phys. Lett. B **452** (1999) 301 [arXiv:hep-lat/9805002].
- [76] T. C. Kraan, P. van Baal, Phys. Lett. **B435** (1998) 389-395. [hep-th/9806034].
- [77] P. van Baal, [hep-th/9912035].
- [78] I. Montvay and G. Munster, “Quantum fields on a lattice,” *Cambridge, UK: Univ. Pr. (2003)*.
- [79] F. Bruckmann, C. Gattringer, C. Hagen, Phys. Lett. B **647** (2007) 56 [arXiv:hep-lat/0612020].
- [80] F. Bruckmann, C. Hagen, E. Bilgici and C. Gattringer, PoS **LATTICE2008** (2008) 262 [arXiv:0810.0899 [hep-lat]].

- [81] E. Bilgici, F. Bruckmann, J. Danzer, C. Gattringer, C. Hagen, E. M. Ilgenfritz and A. Maas, *Few Body Syst.* **47** (2010) 125 [arXiv:0906.3957 [hep-lat]].
- [82] B. Zhang, F. Bruckmann, C. Gattringer, Z. Fodor and K. K. Szabo, arXiv:1012.2314 [hep-lat].
- [83] T. DeGrand and C. DeTar, “Lattice Methods For Quantum Chromodynamics” *World Scientific (2006)*.
- [84] C. Hagen, “Improved hadronic measurements and spectral sums on the lattice” (PhD thesis).
- [85] R. Gupta, [arXiv:hep-lat/9807028].
- [86] H. Kluberg-Stern, A. Morel and O. Napoly, *Nucl. Phys. B* **220** (1983) 447;
- [87] F. Gliozzi *Nucl. Phys. B* **204** (1982) 419.
- [88] L. Susskind, *Phys. Rev. D* **16** (1977) 3031.
- [89] J. B. Kogut, *Rev. Mod. Phys.* **55** (1983) 775.
- [90] R. Lohmayer, “Globale Symmetrien der $SU(2)_{color}$ QCD Wirkung im Kontinuum und für staggered Fermionen” (Projekt im Rahmen des beschleunigten Studienganges zum Modul Quantenchromodynamik, Univeristy of Regensburg, Notes in German).
- [91] A. Bazavov *et al.* [HotQCD Collaboration], *J. Phys. Conf. Ser.* **230** (2010) 012014. [arXiv:1005.1131 [hep-lat]].
- [92] F. Synatschke, A. Wipf and C. Wozar, *Phys. Rev. D* **75** (2007) 114003 [arXiv:hep-lat/0703018].
- [93] F. Synatschke, A. Wipf and K. Langfeld, *Phys. Rev. D* **77** (2008) 114018 [arXiv:0803.0271 [hep-lat]].
- [94] S. Borsanyi, F. Bruckmann, Z. Fodor, C. Gattringer, K. Szabo, B. Zhang, In preparation
- [95] F. Karsch, E. Laermann, A. Peikert, *Phys. Lett.* **B478** (2000) 447-455. [hep-lat/0002003].
- [96] J. Braun, L. M. Haas, F. Marhauser and J. M. Pawłowski, *Phys. Rev. Lett.* **106** (2011) 022002 [arXiv:0908.0008 [hep-ph]].
- [97] C. S. Fischer and J. A. Mueller, *Phys. Rev. D* **80** (2009) 074029 [arXiv:0908.0007 [hep-ph]].
- [98] K. Kashiwa, H. Kouno and M. Yahiro, *Phys. Rev. D* **80** (2009) 117901 [arXiv:0908.1213 [hep-ph]].
- [99] T. K. Mukherjee, H. Chen and M. Huang, *Phys. Rev. D* **82** (2010) 034015 [arXiv:1005.2482 [hep-ph]].
- [100] R. Gatto and M. Ruggieri, *Phys. Rev. D* **82** (2010) 054027 [arXiv:1007.0790 [hep-ph]].

- [101] J. Danzer, C. Gattringer and A. Maas, *JHEP* **0901** (2009) 024 [arXiv:0810.3973 [hep-lat]].
- [102] E. Bilgici, C. Gattringer, E. M. Ilgenfritz and A. Maas, *JHEP* **0911** (2009) 035 [arXiv:0904.3450 [hep-lat]].
- [103] F. Bruckmann and G. Endrodi, [arXiv:1104.5664 [hep-lat]].
- [104] C. Gattringer, private communication.
- [105] K. F. Riley, M. P. Hobson and S. J. Bence, “Mathematical methods for physics and engineering” *Cambridge University Press*, (2009).

Chapter 7

Appendix

7.1 Magnetic charge and winding number

This appendix will prove that the magnetic charge of a 't Hooft–Polyakov monopole is proportional to the winding number of $\vec{n}_\phi(\vec{n}_x)$ from the S_∞^2 of $|\vec{x}| = R \rightarrow \infty$ in coordinate space to the S^2 of $|\vec{\phi}| = 1$ in color space. All the definitions can be found in section 2.5.

We can define the gauge field in the remaining $U(1)$ direction as

$$A'_\mu = n_\phi \cdot A_\mu^a \quad (7.1)$$

and consider 't Hooft's field strength tensor

$$F'_{\mu\nu} = n_\phi \cdot F_{\mu\nu} - \frac{1}{e|\phi|^3} \epsilon_{abc} \phi^a (D_\mu \phi)^b (D_\nu \phi)^c. \quad (7.2)$$

We rewrite it in terms of A'_μ and ϕ :

$$F'_{\mu\nu} = \partial_\mu A'_\nu - \partial_\nu A'_\mu - \frac{1}{e|\phi|^3} \epsilon_{abc} \phi^a (\partial_\mu \phi^b) (\partial_\nu \phi^c). \quad (7.3)$$

Plugging in the asymptotic form of the Higgs field ϕ

$$F'_{ij} = -\frac{1}{e|x|^3} \epsilon_{ijk} x^k. \quad (7.4)$$

The magnetic charge of the monopole is

$$q_{mag} = \int_{S_\infty^2} \frac{\epsilon^{ijk}}{2} F'_{jk} d^2 S^i = -\frac{1}{2e} \oint_{S_\infty^2} \epsilon_{ijk} \epsilon_{abc} n_\phi^a \partial_j n_\phi^b \partial_k n_\phi^c d^2 S_i, \quad (7.5)$$

it is proportional to the S^2 winding number of the $n_\phi(n_x)$ as a mapping from the S_∞^2 in coordinate space to the S^2 in color space. So the topological feature of the 't Hooft – Polyakov monopole is an S^2 winding number of the Higgs field ϕ .

7.2 Comparison of numerical integration methods for the Fourier transformation

One crucial task in the evaluation of dual observables is the numerical calculation of the Fourier transformation, for which several methods exist. The question is which one of the methods is the most efficient and gives the smallest error. In this section, we compare Filon integration, Gauss-Legendre quadrature with the default method with equal distances and weights for all the sampling points.

In our first attempt [82], we calculated the Fourier transform to dual observables (cf. (5.8))

$$\tilde{O}_k = \frac{1}{2\pi} \int_0^{2\pi} d\phi e^{-ik\phi} O(\phi). \quad (7.6)$$

by taking 16 or 8 sampling points between $\phi = 0$ and $\phi = 2\pi$ with equal distances and equal weights, the integration becomes a Riemann sum:

$$\tilde{O} = \sum_{j=0}^{n-1} \frac{e^{-2\pi i j/n}}{n} O\left(\frac{2\pi j}{n}\right). \quad (7.7)$$

This is the “default” method for numerical integration, but it might be of low efficiency and give large errors.

Adaptive methods could give a satisfactory result with high accuracy for the numerical integration. However, we want to calculate the dual observables with different masses from the same data. They result in very different ϕ dependence, see Fig. 5.14 and 5.9. Adaptive sampling points might be good for some integrations but bad for the others. Therefore we study some non-adaptive numerical integration methods in this section, the Filon integration formula and the Gauss-Legendre quadrature methods.

The Filon integration formula [105] is designed for high frequency Fourier transformation

$$\begin{aligned} \int_{x_0}^{x_{2n}} O(x) \cos(tx) dx &= h \{ \alpha(th) [O_{x_{2n}} \sin(tx_{2n}) - O_{x_0} \sin(tx_0)] + \beta(th) C_{2n} \\ &+ \gamma(th) C_{2n-1} + \frac{2}{45} th^4 S'_{2n-1} \} - R_n \end{aligned} \quad (7.8)$$

7.2. COMPARISON OF NUMERICAL INTEGRATION METHODS FOR THE FOURIER TRANSFORMATION

Method a	0.1	0.2	0.3	0.4	0.5	0.6	4.0
Default	3.554	1.790	1.233	1.049	1.007	1.0007	1.023
Filon	4.460	2.247	1.535	1.252	1.136	1.078	0.9931

Table 7.1: Comparison of the default method and the Filon integration (both have 10 sampling points) normalized by the exact value of the integration.

where

$$C_{2n} = \sum_{i=0}^n O_{x_{2i}} \cos(tx_{2i}) - \frac{1}{2}[O_{x_{2n}} \cos(tx_{2n}) + O_{x_0} \cos(tx_0)] \quad (7.9)$$

$$C_{2n-1} = \sum_{i=0}^n O_{x_{2i-1}} \cos(tx_{2i-1}) \quad (7.10)$$

$$S'_{2n-1} = \sum_{i=0}^n O_{x_{2i-1}}^{(3)} \sin(tx_{2i-1}) \quad (7.11)$$

$$\alpha(\theta) = \frac{1}{\theta} + \frac{\sin(2\theta)}{2\theta^2} - \frac{2\sin^2(\theta)}{2\theta^2} \quad (7.12)$$

$$\beta(\theta) = 2\left[\frac{1 + \cos^2(\theta)}{\theta^2} - \frac{\sin(2\theta)}{\theta^3}\right] \quad (7.13)$$

$$\gamma(\theta) = 4\left[\frac{\sin(\theta)}{\theta^3} - \frac{\cos(\theta)}{\theta^2}\right] \quad (7.14)$$

$$R_n = \frac{1}{90}nh^5O^{(4)}(\xi) + O(th^7). \quad (7.15)$$

Here $x_0 \dots x_{2n}$ are equal distance sampling points, h is the step length and R_n is the remainder.

We adopt a Gaussian test function $f(\phi) = e^{-\frac{\phi^2}{a^2}}$, $\phi \in [-\pi, \pi)$ to mimic the general condensate $\Sigma_m(\phi)$, a is the width parameter of the test function. A small a mimics the general quark condensate with small mass at high temperature, which is the case that we might have large errors in the dual condensate if we adopt the “default” method. A large width a gives to an approximately constant function in the given interval which is similar to the general quark condensates at low temperature. The result of The Filon integration is not satisfactory, see Table 7.1.

The Gauss-Legendre quadrature [105] is designed for the integration of polynomials, with n sampling points it gives the exact result for the integrations of polynomials of highest order $2n - 1$.

The standard Gauss-Legendre quadrature is for an integration from -1 to 1 , $\int_{-1}^1 f(x)dx$. Gauss-Legendre quadrature has some extended methods for $\int_a^b f(x)W(x)dx$ where $W(x)$ is the weighting function [105]. In our case (dual condensate), we use the standard Gauss-Legendre quadrature with $W(x) = 1$ and $f(\phi) = \Sigma(\phi)e^{-i\phi}$.

The rank n Gauss-Legendre quadrature formula is very simple:

$$\int_{-\pi}^{\pi} f(x)dx \approx \sum_{i=1}^n f(x_i)w(x_i) \quad (7.16)$$

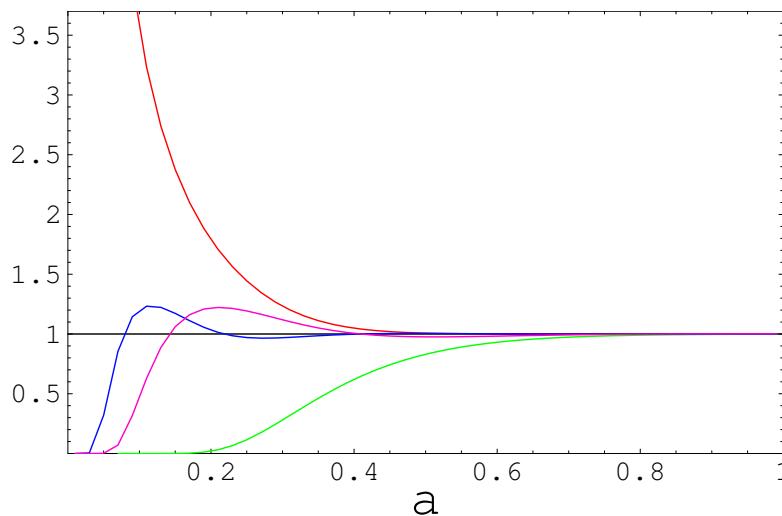


Figure 7.1: Comparison of different Gauss-Legendre methods (10 sampling points). Numerical integration as a function of the width of the test function normalized by the exact result. Green, blue and pink lines for standard, shifted and double shifted Gauss-Legendre method respectively, the red line is for the default method.

Method	a	0.1	0.2	0.3	0.4	0.5	0.6	4.0
Standard		2.9×10^{-9}	0.01991	0.2805	0.6200	0.8301	0.9309	1
Shifted		1.206	1.033	0.9688	0.9982	1.004	1.001	0.9724
Double		0.4746	1.219	1.119	1.006	0.9759	0.9821	1
Default		3.554	1.790	1.233	1.049	1.007	1.0007	1.023

Table 7.2: Comparison of the standard, shifted, double shifted Gauss-Legendre method and the default method.

where $f(x_i)$ is the value of the function at the sampling points x_i . x_i are π times the roots of the Legendre polynomial $P_n(x)$, and $w(x_i)$ are their weights,

$$w(x_i) = \frac{2}{nP_{n-1}(x_i)P'_n(x_i)}. \quad (7.17)$$

The sampling points distribute densely around $-\pi$ and π , while dilutely around 0. We can change this by shifting the sampling points by $x \rightarrow x + \pi$ to move the dense part to around 0, called shifted Gauss-Legendre method, or by $x \rightarrow (x + \pi)/2$ and $x \rightarrow (x - \pi)/2$ to have two dense regions around $\pm\pi$ and 0 respectively, called double Gauss-Legendre method.

Again, we adopt $e^{-\phi^2/a^2}$ as the test function and consequently $f(\phi) = \cos(\phi)e^{-\phi^2/(2\pi a)^2}$. Table 7.2 and Fig. 7.1 shows the results of different Gauss-Legendre methods normalized by the exact result.

Let us summarize the performance of the different numerical integration methods. If the dual condensate $\Sigma_m(\varphi)$ has an exact cosine behavior, $\Sigma \sim a + b \cos(\phi)$, the default method will always give the exact result if the number of sampling points is larger than 2.

7.2. COMPARISON OF NUMERICAL INTEGRATION METHODS FOR THE FOURIER TRANSFORMATION

The Filon integration formula might be good for high frequency Fourier transformations, but it seems to be always worse than the default method with the test function is $\exp(\phi^2/a^2)$.

The standard Gauss-Legendre method has a terrible performance in the small a cases, but is perfect in the flat cases where a is large. The shifted Gauss-Legendre method has good performance in the small a cases, but has a non-vanishing error in the flat cases. The double shifted Gauss-Legendre method have a “balanced” performance between the standard and the shifted Gaussian-Legendre method.

The secret of different performance of the Gauss-Legendre methods might reside in the dense region(s) of the sampling points and the region(s) of the large integrand derivative(s). In cases they coincide with each other, the Gauss-Legendre methods have a nice performance, otherwise they seem to give no improvement.

Is it really necessary for us to adopt the Gauss-Legendre quadrature? From the last plot ($m = 10\text{MeV}$, $T = 892\text{MeV}$) of Fig. 5.9, we can estimate that the width of the lump is around $a \simeq 0.3 \sim 0.4$, and the error should be less than 25%.

If we choose the Gauss-Legendre methods, which would have better performances at high temperature, will have worse performances at low temperature compared to the default method. Another advantage of the default method is that it can be easily improved by measurements on additional sampling points in the middle between the old ones. We stick to the default method in our numerical calculations in Chapter 5.

Acknowledgments

First of all, I want to thank my adviser Dr. Falk Bruckmann, for these very interesting research projects, answering innumerable questions in the past three years and the strict attitude of a physicist I feeld many times on him. His comments are very important parts of this thesis.

I would like to thank my collaborators, Dr. Szabolcs Borsanyi for the programs for smearing, suggesting the connection between the quark number susceptibility and the dual quark density, Prof. Dr. Christof Gattringer for many discussions on dual observables and insights on dual quark density and other dual observables, Dr. Ernst-Michael Ilgenfritz for many discussions on calorons and vortices. I also want to thank Dr. Craig McNeile and Dr. Christian Hölbling for helpful discussions on constructing operators with the staggered fermions, and Dr. Jacques Bloch for answering many questions on numerical integrations and ARPACK.

I would like to say thanks to my adviser of master thesis Prof. Dr. Shi-lin Zhu and my collaborator at that time Dr. Xiang Liu for the discussions on hadron spectrum problems.

Many thanks to my officemate, Florian Gruber for all the short discussions and comments on physics in the last two years and two of my best friends Xiao Liu and Peng-zhi Huang for answering and discussing a lot of basic questions when I was a graduate student in Peking University.

I also want to thank my colleagues, Johannes Najjar, Martin Hetzenegger and Sarah Collins for many helps on computer problems and programming.

I was financially supported by Deutsche Forschungsgemeinschaft grant BR 2872/4-1 and BR 2872/4-2 and in the last four months by Bergische Universität Wuppertal, for which I am grateful to Prof. Dr. Zoltan Fodor.

The computations in this thesis were performed on the Athene supercomputer at the University of Regensburg, HLRB2 at Leibniz-Rechenzentrum and clusters at the University of Regensburg.

Many thanks also go to the secretaries of our group, Heidi Decock and Monika Maschek.

Finally, I want to thank my parents, for supporting me all these years.